Charge Carrier Diffusion and Transfer Mechanism in Hybrid Lead Halide Perovskite Materials

Ladungsträgerdiffusion und Ladungsträgerübertragungsmechanismus in hybriden bleihalogenidbasierten Perowskit-Materialien

Der Naturwissenschaftlichen Fakultät
der Friedrich-Alexander-Universität Erlangen-Nürnberg

zur Erlangung des Doktorgrades Dr. rer. nat.
vorgelegt von

M. Bianka D. Puscher

Als Dissertation genehmigt
Von der Naturwissenschaftlichen Fakultät
der Friedrich-Alexander-Universität Erlangen-Nürnberg

Tag der mündlichen Prüfung: 15. Oktober 2019

Vorsitzender des Promotionsorgans: Prof. Dr. Georg Kreimer

Gutachter: Prof. Dr. Dirk M. Guldi
Gutachter: Prof. Dr. Tim Clark

Die vorliegende Arbeit entstand im Zeitraum von Oktober 2013 bis Juli 2019 im Department Chemie und Pharmazie (Lehrstuhl für Physikalische Chemie I) der Friedrich-Alexander Universität Erlangen-Nürnberg im Arbeitskreis von Prof. Dr. Dirk M. Guldi, sowie während eines viermonatigen wissenschaftlichen Auslandaufenthaltes (Oktober 2013 bis Januar 2014) im Arbeitskreis von Dr. Gerrit Boschloo und Dr. Erik M. J. Johansson im Department of Chemistry, Uppsala University, Schweden.

Abstract

Lead-based halide perovskite solar cells are a young but highly promising research field for future photovoltaic technologies. They have rapidly become the center of attention due to their outstanding power conversion efficiencies, yet the devices' stability under working conditions is challenging. Furthermore, as a young and unique solar cell concept, their working principle is still under heavy debate. In light of this, the aim of the work at hand is the investigation of lead-based halide perovskite's ionic conductivity with respect to device stability, as well as charge carrier injection and recombination processes across the interfaces of perovskite-materials with either a hole or an electron transporting layer. To this end, we have investigated model systems of perovskite solar cells using electrochemical methods, i.e. voltammetry, amperometry, and impedance spectroscopy, as well as femto-second transient absorption spectroscopy. We compared these results to figures-of-merit derived from current density voltage characteristics of full devices. We found that the ionic conductivity of hybrid perovskite was dependent on two diffusing species, namely halides and organic cations. This is in contrast to inorganic perovskite, where only halides diffuse, and forceful displacement of its second, non-lead inorganic cation causes decomposition. In ternary blends composed of perovskite nanoparticles, a polymer-based photon absorber, and a fullerene derivative, the charge carrier transport is facilitated by a cascading energy level alignment. We found that the presence of perovskite nanoparticles enables fast and longer-lasting charge carrier separation. In the next step, the electron injection from perovskite into electron transporting materials of different crystallinity was studied. Here, a layer of a polycrystalline fullerene derivative was compared to its amorphous standard analog. The augmented surface area and discrete energy levels of the polycrystalline film was found to offer ultrafast electron injection from perovskite. Finally, we turned towards charge carrier transfer processes occurring across the interface of perovskite with a small molecule type and polymer-based hole transporting materials. In both cases we found comparable injection time frames that corroborate ultrafast injection from perovskite. Furthermore, our study revealed an electron loss-pathway that elucidates how current loss in polymer-based hole transporting materials is correlated to the energetically deep lowest occupied molecular orbital. The findings of the work at hand help to open pathways for a better device stability as well as improved charge carrier injection for higher power conversion efficiencies of future perovskite solar cells.

Kurzbeschreibung

Ein vielversprechender Forschungsbereich für zukunftsorientierte Photovoltaik-technologien sind Bleihalogenid-Perowskit-Solarzellen, die durch ihre herausragenden Wirkungsgrade rasch in den Fokus der Forschung rückten. Unter Arbeitsbedingungen stellt die kurze Lebensdauer dieser Solarzellen jedoch nach wie vor eine Herausforderung dar und das Arbeitsprinzip ist noch nicht abschließend geklärt. Deshalb ist das Ziel dieser Arbeit die ionische Leitfähigkeit innerhalb der Perowskit-Materialien, sowie die Ladungsträgerinjektion und –rekombination an den Grenzflächen von Perowskit-Materialien mit entweder einem Lochleiter oder einem Elektronenleiter zu untersuchen. Hierfür haben wir Modellsysteme der Solarzellen mittels elektrochemischen Messmethoden wie Voltammetrie, Amperometrie, und Impedanzspektroskopie, sowie zeitaufgelöste Transiente-Absorptionspektroskopie im Femtosekundenbereich untersucht. Die so gewonnenen Erkenntnisse wurden mit den Leistungskennzahlen und Wirkungsgraden der Solarzellen, welche anhand von Stromdichtespannungskennlinien bestimmt wurden, verglichen. Wir fanden heraus, dass die ionische Leitfähigkeit der hybriden Perowskite von zwei diffundierenden Komponenten abhängig ist, den Halogeniden und den organischen Kationen. Im Gegensatz dazu diffundieren in anorganischen Perowskiten nur Halogenide, da eine erzwungene Migration des zweiten, nicht-bleiartigen anorganischen Kations zur Zersetzung des Materials führt. In einer ternären Mischung bestehend aus Perowskit-Nanopartikeln, einem polymerbasierten Lichtabsorber und einem Fullerenderivat wird die Ladungsträgerübertragung mittels einer kaskadenartigen Anordnung der Energielevel erleichtert. Wir beobachteten dabei, dass die Nanopartikel eine schnellere und langlebigere Ladungsträgertrennung begünstigen. Im nächsten Schritt untersuchten wir die Elektroneninjektion von Perowskit-Materialien in elektronleitenden Materialen mit unterschiedlicher Kristallinität. Hierfür wurde ein neuer Ansatz zur Herstellung kristalliner Nanopartikel, die aus einem Fullerenderivat bestehen, verwendet. Aus genannten Nanopartikeln stellten wir anschließend Dünnschichten her, welche mit ihren amorphen Standardanalogen verglichen wurden. Der polykristalline Film, der eine vergrößerte Oberfläche aufweist und diskrete Energielevel hat, ermöglicht eine ultraschnelle Elektroneninjektion vom Perowskit. Schlussendlich untersuchten wir Ladungsträgertransferprozesse an der Grenzfläche von Perowskit-Materialien mit kleinmolekularen und verschiedenen polymerbasierten Lochleitern. Für beide Arten fanden wir vergleichbare Injektionszeiten, welche die

ultraschnelle Lochinjektion vom Perowskit-Material untermauern. Diese Studie deckte außerdem einen zusätzlichen Verlustkanal für Elektronen auf, der den niedrigen Wirkungsgrad polymerbasierter Lochleiter mit tiefliegendem LUMO (engl. lowest unoccupied molecule orbital) erklärt. Die in dieser Arbeit dargelegten Erkenntnisse werden helfen, Perowskit-Solarzellen mit verbesserter Stabilität zu entwickeln und den Wirkungsgrad zu erhöhen, indem die Ladungsträgerseparierung sowohl beschleunigt als auch verlängert wird.

Table of Contents

1. Introduction

The growth and cultural evolution of the human species was from its turning point in evolution – the governing of fire[1] – directly related to the use of extra-somatical energy. Traditionally, this energy was obtained from biomasses or from solar heating through skillful architecture. Yet, with the universal application of the steam engine during the industrial evolution (1760-1840) and, especially, since the beginning of the digital revolution, the global primary energy consumption has increased exponentially. Just within the last 67 years, it skyrocketed from 27.972 to 153.595 terawatt hours (TWh)[2,3]. To cover this rising energy demand, technologies were developed that exploit fossil fuels, such as coal, petroleum, and natural gasses, as innovative and highly efficient energy sources. Certainly, this development will continue in our digital age due to two major reasons. Firstly, developed countries want to retain their high living standards that are exemplified by easy-to-access worldwide commodities due to globalized transport, a world travelling mindset, conditioned housing climate, artificial illumination, and consumerism towards state-or-the-art technology. In the year 2017, these energy exploitation factors added up to 3,808 TWh in the Federal Republic of Germany alone and can be subdivided into four sectors: transportation (29.5%), residential (26%), commercial (15.5%), and industrial (28.9%) (*Figure 1A*)[4,5]. Secondly, developing countries urge to achieve the same high living standards developed countries have attained.

This has, however, left a mark on our environment. About 80% of our primary energy consumption is covered by fossil fuels (*Figure 1B*), which exploits energy that was accumulated and stored over hundreds of millions of years but is now released over a few hundred years[6,7]. Hence, humans became the species that has the highest impact on the Earth's geology and ecosystems[8] since cyanobacteria caused the Great Oxygenation Event that enabled life for aerobes[9]. Consequences are, for example, an anthropogenic climate change, air and water pollution, as well as loss of biodiversity. The awareness to address these impacts has risen from an individual to a global scale as demonstrated by an increased worldwide focus on bio-products[10], increasing participation and a growing interest in environmental policy, protest movements like "Fridays for future", and global agreements such as the "Paris Climate Change Agreement"[11]. A highly efficient alternative to fossil fuels are nuclear power plants that provide a constant energy source. Yet it bears severe drawbacks; firstly, the

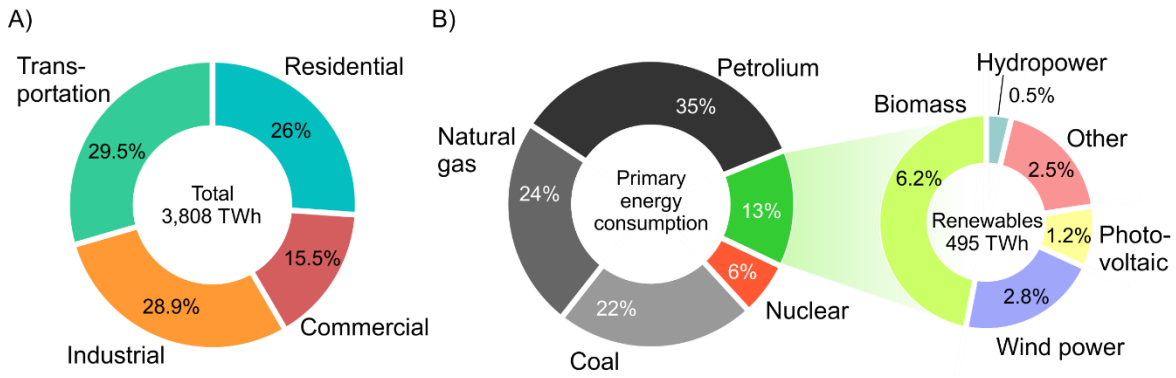

Figure 1. Total energy consumption of the Federal Republic of Germany in 2017 by sectors (A) and by sources (B). Numbers given are taken from the energy data provided by the Umweltbundesamt as well as the Bundesministerium für Wirtschaft und Energie[4,5].

byproducts of nuclear power generation are long-lived radioactive waste[12] and, secondly, the risk of nuclear disasters is present with not yet fully assessable consequences[13,14]. Consequently, nuclear energy covers only 6% (*Figure 1B*) of the primary energy consumption in the Federal Republic of Germany with falling tendency towards the nuclear phaseout.

Hence, the challenge of our time is to develop clean, environmentally friendly, renewable, and save technologies for energy production that can still maintain the acquired modern lifestyle of developed countries while allowing the same to developing countries without compromising the needs of future generations[15]. The major contribution to the energy generation by renewables comes from traditional combustion of biomass (6.2%). Although originally well-intended, biofuels have fallen into disrepute as their resources are taken from forests, causing deforestation and soil erosion especially in rain forests, or is grown on farmland that could otherwise be used for food production[16,17]. Technologies that have the potential to fulfil the named requirements are hydro-, tidal-, and wind power, geothermal energy, as well as solar heat and photovoltaic energy production. Most of these technologies are, though, linked to naturally occurring conditions and, hence, not universally available. Furthermore, the energy generation is limited by the occurrence and strength of its resources, i.e. wind, current, and sunlight. Technology that harvests solar energy offers the most potential[18]. Firstly, the technology and, in turn, the generation of electricity is readily utilizable in all four energy consumption sectors (*Figure 1A*). Secondly, it accesses an abundant energy source that is, in principle, universally accessible. The annual total amount of energy that the Earth receives from the Sun, approximately

3.85×10^{24} Joule ($\sim1.07\times10^{9}$ TWh)[2], could cover the global primary energy consumption manifold. There are locations on Earth, i.e. deserts and plateaus, that recieve constant and high irradiation intensities. For example, the Longyangxia Dam Solar Park on the Tibetan Plateau consists of more than four million solar panels that cover about 26 square kilometers and generates up to 850 megawatts of electricity[19]. Furthermore, projects like the International Space Station with its 35 meter (m) long solar array wings demonstrate that it possible to power a living environment exclusively by solar energy[20].

Compared to other renewable technologies, turning sunlight into electricity by illuminating a semiconductor is a relatively novel concept. The foundation was laid by Alexandre Edmond Becquerel in 1839[21]. He was the first to discover the photovoltaic effect by measuring an electric current when illuminating metal electrodes immersed in diluted acid. In the 1870s, Willoughby Smith as well as William Grylls Adams and Richard Evans Day observed the photovoltaic effect by illuminating selenium and, respectively, a junction between selenium and platinum[22,23]. Based on their findings, the first selenium solar cells with about 1% power conversion efficiency (PCE) were created and described by Charles Fritts in 1883[24]. Yet, the breakthrough for a practical use of solar cells was achieved by Russell Shoemaker Ohl, who developed the silicon p-n junction solar device in 1941[25]. The theoretical background of this phenomenon was provided by Albert Einstein's pioneering work on the photoelectric effect published in 1905[26] for which he received the Nobel Prize in 1921.

To improve the conversion of solar energy and to enable a diverse scope of application, various types of solar technologies were developed and are still hot topics in ongoing research. The devices are classified into different generations (*Figure 2*)[22]. The first generation are thick crystalline silicon wafer solar cells that lead to high efficiencies and longevity but are also energy intensive to manufacture, costly, and heavy[27,28]. In order to reduce the production costs by saving material, thin film technology was introduced. Here, the active layer is only a few micrometers thick, which, in turn, allows for solar cells that are lower in weight, flexible, and can be applied on, for example, a window as semi-transparent, photovoltaic glazing material[29]. Semiconductors used for this technology are amorphous silicon, cadmium telluride (CdTe), gallium arsenide (GaAs), and copper indium gallium selenide (CIGS)[30–33]. The efficiencies obtained in the laboratory are comparable to traditional silicon solar cells. However, an upscaling

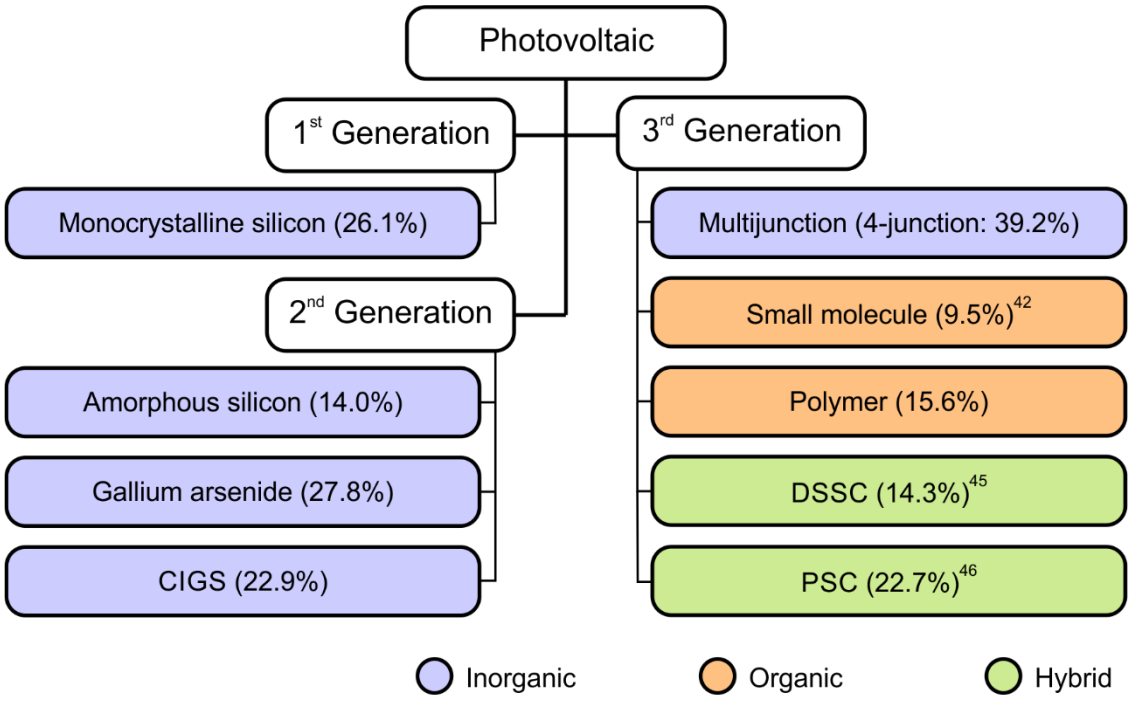

Figure 2. Solar cell generations with their representing important technologies and their record power conversion efficiencies according to NREL if not highlighted differently[28,42,45,47].

towards mass production at competitive prices without a severe loss in efficiency proved challenging. Furthermore, some thin film devices consist of rare earth elements and toxic materials, rendering them less sustainable.

The aim for third generation photovoltaic cells is a cost-effective production while providing high efficiencies and a vast range of application. This includes shifting from inorganic constituents to organic compounds and hybrids that can be processed from solution. An additional objective is to overcome the limitation caused by using a single-junction. Here, the theoretical maximum efficiency of 33% cannot be exceeded according to William Shockley and Hans-Joachim Queisser because the majority of photons have a lack or an excess of energy compared to the materials band-gap[34]. Third generation solar cells have the potential to surpass this limit owing to their architecture and unique properties of their materials. For example, two absorbers harvest complementarily the Sun's light in a co-sensitization approach, or alternatively multiple layers can be used in a tandem device (*Chapter 4.2.1*)[35–37]. Another example are compounds that perform singlet fission, such as pentacene[38,39], or semiconductors that have "long-lived" hot carriers (*Chapter 4.2.2*). Representatives of this generation are multijunction solar cells[40], small molecule solar cells[41,42], polymer solar cells also known as organic photovoltaics[35,43], dye-sensitized solar cells (DSSC)[44,45], and

perovskite solar cells (PSC)[46,47]. In order to render one technology commercially applicable it has to fulfill three conditions of i) having power conversion efficiencies that equal or surpass traditional silicon solar cells, ii) being inexpensive in production, and iii) having a long lifespan. To date, every type of third generation solar cells falls short on at least one of the three conditions. There is one technology that is considered to surpass silicon solar cells, namely lead-based halide perovskite solar cells. As the fastest growing photovoltaic technology, it has surpassed power conversion efficiencies of any type of dye-sensitized, organic, and conventional thin-film technology in the laboratory (*Figure 2*)[28,47,48]. The perovskite material consists of abundant elements (*Chapter 2.1.1*) and its manufacture is rather energy efficient. The production of highly crystalline layers can be performed under low-temperature, solution-based conditions, which allows for large scale manufacturing *via* ink-jet printing[49]. The major challenges for commercial application of perovskite solar cells are its toxicity and long-term stability. Here, environmental factors, such as oxygen and a humid atmosphere, are readily resolved by encapsulation[50,51] – which also enables a controlled and safe handling of the lead-based material. The stability of perovskite is also governed by intrinsic factors. It decomposes at temperature as low as 40 °C to 80 °C[52,53] or as a result of ion migration. The latter is mediated by illumination[53–55] and an applied bias[54] (*Chapter 4.1*), causing the material to degrade under working conditions. This was met by tuning of the material's composition, alkali doping, and passivation of grain boundary, which increased both the decomposition and ionic diffusion energy barrier[48,56–59]. The resulting perovskite solar cells are by now stable for more than 1000 hours[47,57] and, thus, also meet the third condition for commercialization.

2. Background

2.1. Perovskite as semiconductor

The material known as perovskite derives its name from the eponymous crystal structure of calcium titanate, which was first discovered by Gustav Rose[60] and named after the Russian mineralogist Lev Perovski. It has a general chemical formula of **ABX_3**, where for lead trihalide based perovskites **B** is a metal cation (here twofold charged lead, Pb^{2+}) and **X** is a halide (iodide, I^-, or bromide, Br^-). In the case of inorganic perovskite material, **A** is a monovalent cation (e.g. cesium, Cs^+; *Figure 3A*) or, for hybrid organic-inorganic perovskites (HOIP), an isoelectronic organic moiety (e.g. methylammonium, MA^+, or formadinium, FA^+; *Figure 3B*).

Although there were several studies on its properties already in the 1980-90s[61–70], lead trihalide based materials for perovskite solar cells (PSC) and perovskite light-emitting diodes (LED) entered the spot-light of world-wide research only 10 years ago. Originating from the well-versed field of dye-sensitized solar cells (DSSC)[71] and benefiting from the extensive research on organic and thin-film technologies, the power conversion efficiency of perovskite devices showed the fastest progress of all technologies[28,72]. Within six years, the power conversion efficiency increased from 3.8% for a perovskite-based DSSC (Miyasaka and colleagues, 2009)[71], *via* 10.9% for the first solid DSSC (sDSSC; Miyasaka, Snaith and colleagues, 2012)[73], to a PSC of 19.7% (Park and colleagues, 2015)[74]. With improving film formation techniques, fine-

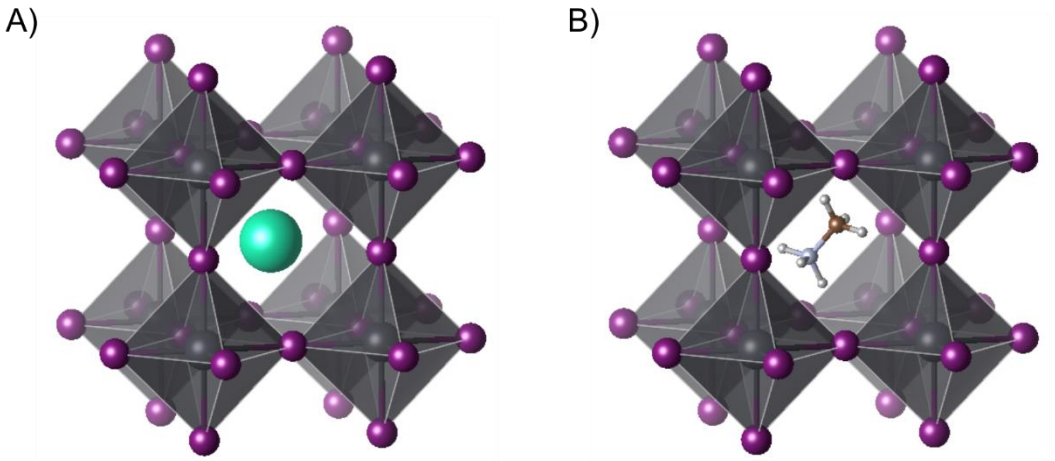

Figure 3. Cubic crystal structure of $CsPbI_3$ (A) and $MAPbI_3$ (B) (Pb^{2+}: black sphere; I^-: purple sphere; methylammonium molecule with cesium: turquoise sphere, carbon: brown, nitrogen: light blue, and hydrogen: white) derived from single crystal X-ray diffraction by Stoumpos *et al.*[69] and neutron powder diffraction by Whitfield *et al.*[70], respectively.

tuned composition of the perovskite, as well as attuned hole transporting materials (HTM) and electron transporting materials (ETM) power conversion efficiencies exceeding 20% are by now published[46–48,75,76].

Perovskite materials owe their leading role in optoelectronics to their various exceptional properties:

(i) Perovskite materials in general, but methylammonium lead triiodide (MAPI) in particular, combines a high absorption coefficient (e.g. $1.3 \cdot 10^5$ cm^{-1} at 550 nm)[77] with a broad absorption spectrum in the visible range[77–79]. By exchanging and/or mixing of the constituents, the band-gap (Chapter *2.1.3*), and, hence, the absorption onset, can be shifted[80]. This also allows for the fine-tuning of perovskites' photoluminescence (PL)[81–84], enabling emission across the whole visible range. Hybrid as well as all-inorganic perovskite materials exhibit PL peaks with a line width of 12-42 nanometer (nm) and quantum yields of 26% for $MAPbI_3$[85] or 50-90% for $CsPbI_3$[83]. This has rapidly attracted the interest of lighting technologies[85–88] with LEDs now reaching external quantum efficiencies of over 20%[89,90].

(ii) At room temperature and above, the primary species generated after photoexcitation was found to be free charges[91–94] while excitons offer a minor contribution due to exciton screening[95]. Consequently, the nature of charge carriers within perovskite materials are closer to inorganic semiconductors, such as gallium arsenide, than to organic solar cells with Wannier excitons that have binding energies below 10 meV[95–97].

(iii) Due to perovskite's soft crystal structure, hybrid perovskite materials are both electronic and ionic conductors. They exhibit charge carrier mobilities of 8-35 cm^2 V^{-1} s^{-1} [91,94,98–100], and diffusion lengths of up to several micrometers[91,92,99] even in solution-processed films. Ions – i.e. halides and even the MA^+ cation – migrate within the crystal structure under an applied bias voltage[64,101–106] and illumination[107,108]. As a result, doped regions are formed within the perovskite layer[106,108–110]. This has a tuning effect on the efficiency of PSCs but also induces a strong photocurrent density voltage (J-V) hysteresis[109] and reduces long-time stability[105]. More information on the ion migration will be presented in *Chapters 2.1.5 and 4.1*.

(iv) In general, perovskite materials used for PSCs consist of abundant materials and highly crystalline layers can be produced under low-temperature, solution-based conditions – *i.e.* spin-coating[73–75], dip coating[111], chemical vapor deposition[112], and ink-jet printing[49]. Furthermore, due to its soft structure it can be implemented into flexible devices[113,114].

In the following, the properties that are central to this work are elaborated.

2.1.1. Crystal structure and composition

In order to understand the exceptional properties of perovskite materials, a detailed depiction of its crystal structure is given in the following (*Figure 4*). The high-temperature (T > 327 K) $Pm\bar{3}m$ cubic structure of MAPI consists of charge counterbalancing **A** cations occupying the 12-fold cavity between octahedra of eight corner-sharing iodide atoms, and central interstitial lead atoms. For hybrid perovskites such as MAPI and formadinium lead triiodide (FAPI), the organic cation is highly disordered. It has *wobbling-in-a-cone* rotations and randomly changes between favored directions, induced by the formation of hydrogen bonds between, preferably, the protonated amine and the iodide atoms of the octahedra[115–120]. In this way, FAPI, which has two amino groups, has a higher phase transition temperature and improved photostability compared to MAPI[121]. Inorganic perovskites with their rigid Cs^+ cations do not feature this plastic crystal character[120].

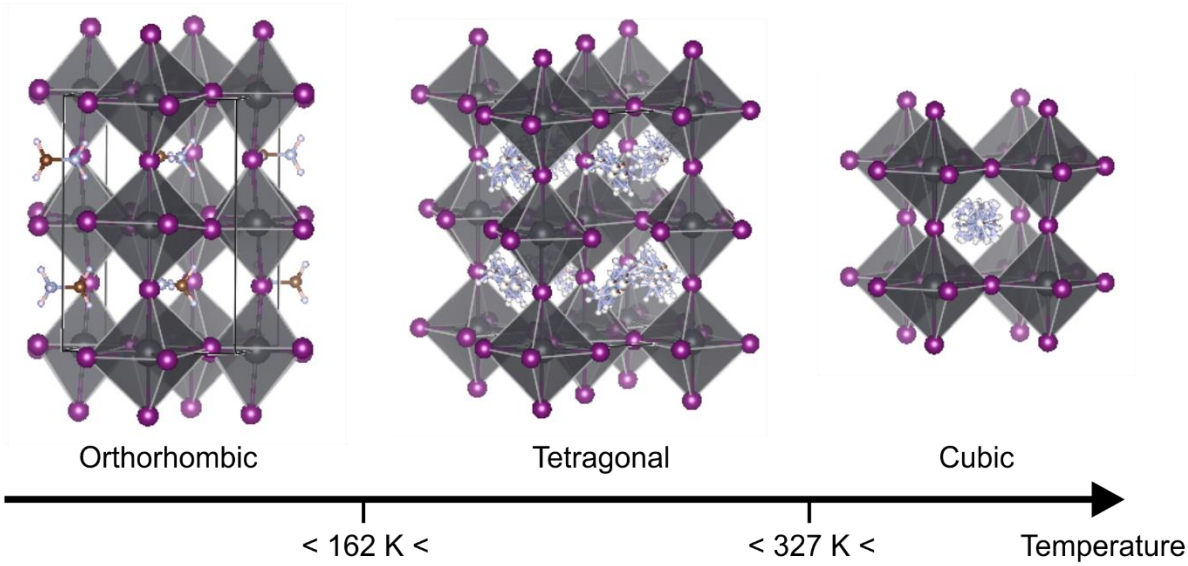

Figure 4. Orthorhombic, tetragonal, and cubic structure models of MAPI with increasing temperature derived from neutron powder diffraction by Whitfield *et al.*[70].

Since Weber *et al.* reported the cubic structure in 1978[62] for the first time, further investigations revealed two phase transitions of MAPI upon cooling, with each lowering the structure's symmetry[63,115,118,120,122,123]. At room temperature, perovskite transforms into the tetragonal phase (*I4/mcm*) with reduced rotational motion of the organic cation[115,120]. Two-dimensional infrared vibrational anisotropy spectroscopy displayed that these reorientations occur on the timescale of 1-10 ps[117,124], having a fast *wobbling-in-a-cone* (~ 0.3 ps) motion and with respect to the crystal structure slower jump-like reorientation of the molecular dipole (~ 2 ps)[119]. Because the organic cation has a strong rotational degree of freedom in both cubic and tetragonal structures, the phase transition from one to the other shows a continuous alternation of its physical properties. This becomes apparent as a red-shift of both absorption onset and photoluminescence with decreasing temperature[98,122,125,126]. The second phase transition (T < 162 K) to the orthorhombic structure (*Pnma*) implies a more drastic change of properties with MA^+ being restricted to rotate around its C-N axis[61].

The rotational dynamic of MA^+ is, furthermore, dependent on the $[PbX_3]^-$ cage. With decreasing size of the halide atom, the halide's reduced polarizability accelerates the rotation of the cation despite rising steric hindrance caused by a smaller framework[127]. As for the phase transitions with decreasing temperature, perovskites with mixed halide composition show decelerated disordered motion and almost immobilization. Selig *et al.* relate this to the breaking of the symmetry within the perovskite unit cell[127], which was found to increase the long-time stability of perovskite and, in turn, PSCs[48,128].

2.1.2. Nanocrystal

Perovskite nanocrystals (NC), which are with an edge length of 15-50 nm not yet affected by quantum confinement, were found to have several improved properties compared to their bulk polycrystalline film counterparts. Surfactants used as capping agent, such as octylammonium[106] or oleylammonium[129], enable NCs to have solubility in a broader range of solvents[83], passivate surface vacancies[87], and insulate against humidity[87,130]. As a result, they can form blends with, for example, HTMs[129,130] in which they act as second photon absorber and/or mediate charge carrier separation

(*Chapter 4.2.1*). The resulting improvement in photoluminescence quantum yield[131] renders perovskite NCs attractive for implementation in lighting technologies[87,88].

2.1.3. Electronic structure

The interaction of the **A** cation with the $[PbX_3]^-$ cage is rather electrostatic and structural and has only slight influence on the band structure[132,133]. Exchanging, for example, MA^+ with the larger FA^+ or the smaller and more rigid Cs^+ causes an approximately 0.04 eV decrease or 0.15 eV increase of the band-gap, respectively[69]. The $[PbX_3]^-$ cage itself, which has a formal electronic configuration of $5d^{10}6s^26p^0$ for lead and $5p^6$ for iodine, determines the valence (VB) and conduction band (CB) energy levels. In this way, the VB maximum consists mainly of the I 5*p* and partly of the Pb 6*s* orbitals, while the CB minimum is mostly dominated by Pb 6*p*[132]. As a result, when going from iodide to bromide, the band-gap energy (E_g) increases from 1.59 to 2.64 eV due to a rise of the CB.

One of the many outstanding properties of perovskite is the broad linear absorption feature that, for iodide containing materials, spans across the whole visible light range (*Figure 5A*). A strong debate arose on the origin of the shoulder (or secondary onset)

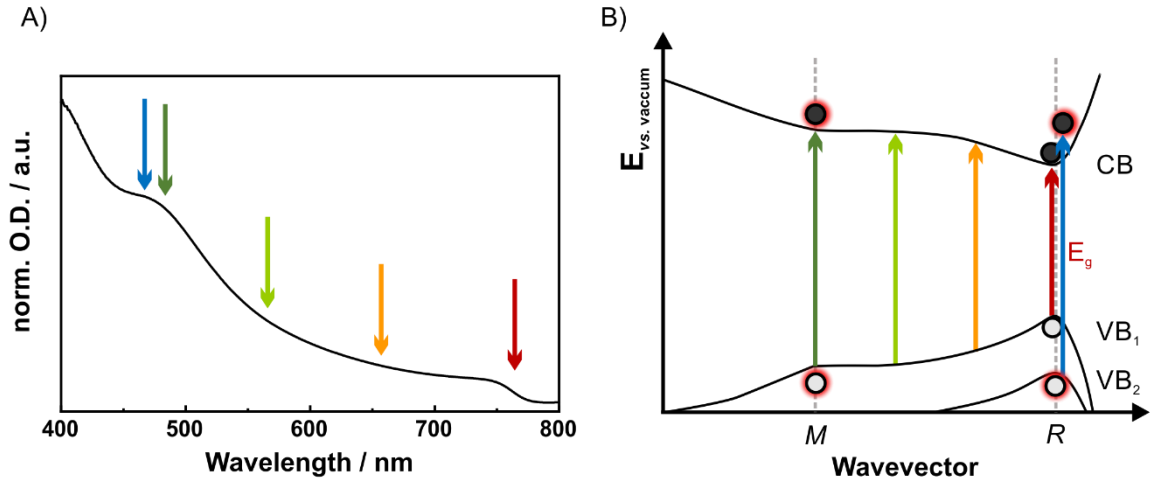

Figure 5. A) Normalized absorption spectrum of MAPI, with colored arrows illustrating the continuous electronic transitions of the VB_1 to CB_1 going from the *R* to the *M* point as well as the transition from VB_2 to CB_1. B) Simplified schematic electronic band structure of MAPI with arrows ranging from red (*R* point), which represents the optical band-gap E_g, to green (*M* point) for allowed photoinduced electronic transitions from VB_1 to CB_1. The partly dipole-allowed electronic transition from VB_2 to CB_1 is depicted with a blue arrow (adapted from density-functional theory calculations presented by Even *et al.*[95]).

at 480 nm (2.58 eV, dark green arrow), assigning it to a high-energy charge-transfer band[134,135], high-energy transitions between higher/lower electronic bands such as $VB_2 \rightarrow CB_1$ or $VB_1 \rightarrow CB_2$[136,137]. Furthermore, it could include contribution of residual lead(II) iodide (PbI_2) with a band-gap onset at 510 nm[135,138]. Another cause for the absorption feature at 480 nm was elucidated by density functional theory that also takes the spin-orbit coupling into consideration[95,139]. Spin-orbit coupling, caused by the heavy nature of perovskite's lead and iodine ions, induces a splitting of the CB with a lowered CB minimum. Even *et al.* reported on MAPI's high symmetry points in the reciprocal space of the Brillouin Zone (*Figure 5B*) and showed the connections between *R* and *M* points and their correlation to the primary (red arrow) and secondary (dark green arrow) absorption onset[95]. Hereby, the photogeneration of charge carriers across the broad range of visible light can be explained, which causes the favorable absorption continuum (colored arrows) for photon energies above E_g. Subsequently, photogenerated "hot" electrons and holes at the *M* point relax towards the *R* point *via* phonon vibration (*Chapter 2.1.4*). In addition, high-energy optical transitions exist between higher/lower electronic bands at the *R* point for the correct symmetry. Yet, the features of $VB_1 \rightarrow CB_1$ at the *M* point (480 nm) and $VB_2 \rightarrow CB_1$ at the *R* point (460 nm) are not well defined due to their close energetic proximity. *Figure 5* shows the schematic electronic band structure (based on calculations of Even *et al.*[95]) correlated to the linear absorption feature of MAPI; red (blue) and green arrows represent the transitions between VB_1 (VB_2) and CB at *R* and *M* points in the Brillouin Zone, respectively.

The debate on the excitonic contribution to the primary onset was, meanwhile, solved unanimously. At temperatures above 160-200 K, and, hence, also upon working conditions, the primary photogenerated species present in perovskite are free charge carriers[91–94]. Only upon cooling, an exciton feature appears at the primary onset of the absorption around 730 nm[68,95,98] and sharpens after phase transition[98]. The excitonic nature of the characteristic is corroborated by a change of the dielectric screening ($\varepsilon_{eff<159\ K} = 11$, $\varepsilon_{eff>212\ K} = 20$)[95] and a rise of the binding energy from 10 meV at room temperature[95–97] to 37-50 meV[68,140,141] at temperatures below 162 K.

2.1.4. Polarons and phonons

Although the excitonic contribution can be neglected for PSCs working under ambient conditions, perovskite's photogenerated free charge carriers easily form large polarons that even dominate at higher temperatures (≥ 290 K). In ionic solids, electrons and holes have a strong interaction with their adjacent charged atoms, causing a polarization and, thus, displacement of the lattice which affects more than one surrounding plane for large polarons (*Figure 6A*)[142]. This screens the charge of the electron/hole. The charge carriers self-trap into localized states, *i.e.* polarons, which increases their effective mass and reduces their mobility. In this way, perovskite has, compared to other semiconductors[143,144], rather moderate charge carrier mobilities. The out-of-equilibrium motion of the framework is known as phonons. As temperature-dependent propagations of the atoms within the crystal structure, they are differentiated by acoustic (A) and optical (O) phonons with the modi transversal (T) and longitudinal (L) (*Figure 6B*). Acoustic phonons follow a coherent movement and are low temperature vibrations, which is a topic beyond the scope of this work. Optical phonons are out-of-phase movements, where the electric field of the light induces a dynamic dipole moment within the crystal structure by accelerating the ions with opposite charge in different directions.

Right after photoexcitation of perovskite, which is a highly anharmonic system, hot charge carriers thermalize *via* sub-picosecond (ps) elastic carrier-carrier scattering and inelastic carrier-longitudinal optical (LO) phonon coupling, otherwise known as Fröhlich interactions. Usually, hot carriers decay within 1 ps *via* subsequent LO phonon emission towards lower lying LO phonon states until the band edge is reached. The full cooling mechanism is not entirely understood yet, but so far reduced phonon-phonon interaction[145] and screening of the Coulomb potential (polaron-protection) were found to slow down the cooling process to 10 ps[96,146]. Simulations of these hot electronic states found an asymmetric behavior for the thermalization of holes and electrons, which was furthermore corroborated by the following observations; the longer living species with 1-5 ps are the hot electrons, while hot holes thermalize within 0.1-0.5 ps[147,148]. This stronger coupling in the VB is correlated to its high density of states, as it is mainly influenced by iodide 5p orbitals. In comparison, the CB is primarily composed of lead 6p orbitals, which is less available due to the 1:3 stoichiometry of the perovskite composition. By increasing the carrier density through high illumination

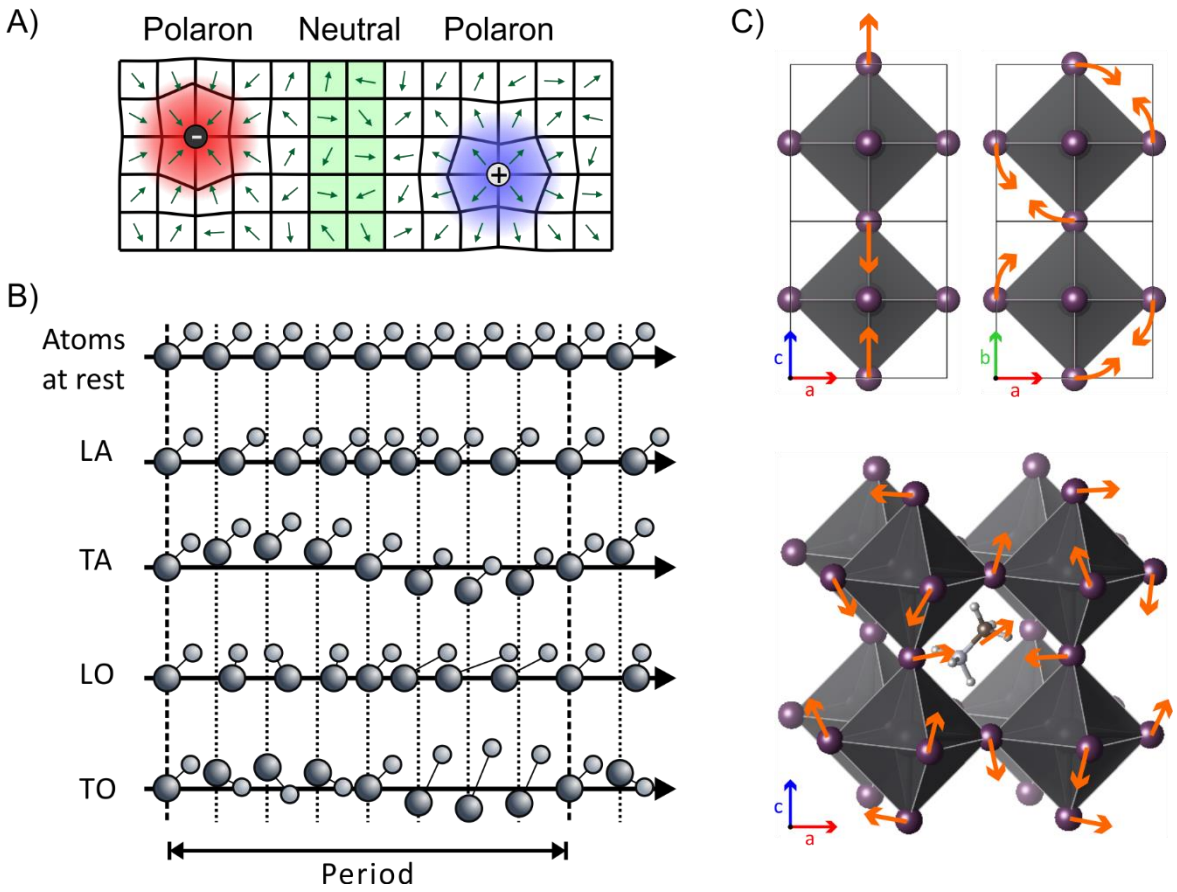

Figure 6. A) Schematic cross section of the MAPI structure (black lines representing lead-iodide bonds, green arrows the MA^+ cation with head as amine) without charge carriers (green), as well as with a negative (red) and a positive (blue) polaron, which deform their surrounding $[PbI_3]^-$ cage. B) Simplified representation of phonon vibrations with combinations of longitudinal (L), transversal (T), acoustic (A), and optical (O) modi. C) Possible phonon vibrations of the crystal structure with orange displacement arrows as calculated by Druzbicki *et al.* and Park *et al*.[116,142].

intensities, hot electrons reach lifetimes of 30 ps due to the hot-phonon bottleneck effect and Auger heating[96]. Possible LO phonon modi were calculated by Druzbicki *et al.* and Park *et al.* of which three are shown in *Figure 6C*[116,142].

The exceptional slow phonon cooling property is mediated by the electron-phonon coupling, which is caused by the displacement of the lead and iodide ions. Although the scientific community agrees on the importance of the dynamic interconnection between the inorganic I-Pb-I framework and the organic cation (*Chapter 2.1.1*) [142,146,148–150], the opinions differ on whether it reinforces or dampens the cooling. Zhu *et al.* described, that in, for example, MAPI, the adjacent MA^+ cations reorientate, which, in turn, deforms and bends the $[PbI_3]^-$ framework[146,149,150]. *Figure 6A* depicts MA^+ cations' dipole moments pointing with the amine (arrowhead) towards the Pb^{2+} center[142]. In inorganic perovskite no polaron-protection was observed as the dynamic

interaction between the Cs^+ cation and the $[PbI_3]^-$ framework is non-existant[146]. Medjet *et al.*, however, found evidence that the motion of the dipole enhances electron-phonon coupling and, thus, shortens the hot carriers' lifetime compared to inorganic perovskite at low-temperature[148].

In conventional semiconductor solar cells, the excess energy of hot charge carriers is lost to heat. Due to reduced thermalization, perovskite is a potential candidate for hot carrier solar cells (*Chapter 4.2.2*). Unfortunately, this also introduces new recombination pathways, when hot electrons are transferred into HTMs with an lowest unoccupied molecular orbital (LUMO) level that is close to the perovskite CB (*Chapter 4.2.3*).

2.1.5. Ion diffusion

The soft crystal structure enables perovskites to be both an electric semiconductor and an ionic conductor. Interestingly, the migration can not only be observed in thin films and crystals of perovskite material by applying an external bias voltage[64,101–106], but already under illumination[107,108]. With perovskite's ionic bonds being rather weak[151], it is prone to high defect densities, meaning ions easily leave their lattice site, creating vacancies and become interstitial (*Figure 7*, blue arrow). At first, it was considered that the ionic diffusion originates entirely from halide anions (V_I) and organic cation vacancies (V_{MA}) (Schottky defects), whose diffusion activation energies were computationally determined to be 0.26-0.50 and 0.55-0.89 eV[103,105,151,152] for V_I and V_{MA}, respectively. The scheme in *Figure 7* shows the preferred diffusion pathways through the bulk according to these calculations: halide vacancies move along the edges of the $[PbX_6]^{4-}$ octahedrons (red), while V_{MA} progresses along the MA-I plane (orange). Further calculations have shown that interstitial I^- and MA^+ (Frenkel defects) have very similar, even marginally lower diffusion activation energies compared to their corresponding vacancies[152] and propagate too[153]. At grain boundaries of polycrystalline films, where ionic bonds are weakened, ion diffusion is enhanced and, additionally, opens a direct path towards the HTM and ETM layers[154]. This transport process was effectively reduced by thermal- and solvent-annealing processes that cause larger grains[110,154–156] and inhibited by passivation using, for example,

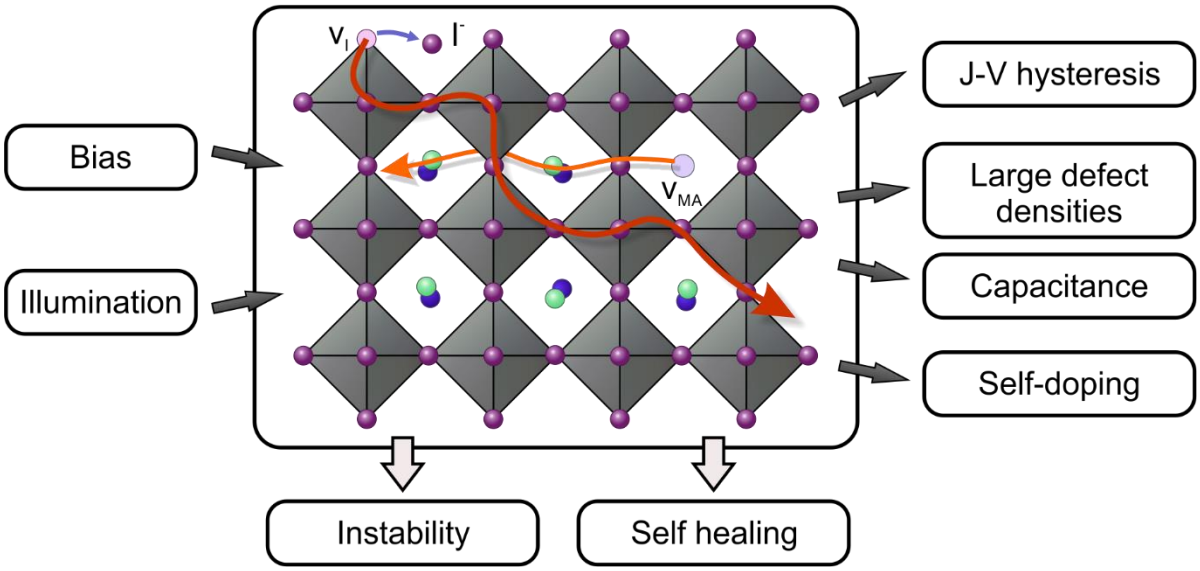

Figure 7. Scheme of the migration of halide vacancies along the edges of the $[PbX_6]^{4-}$ octahedra (red) and organic vacancies in the plane (orange), as well as reasons for defect formation (blue arrow) and migration (left) as well as consequent phenomena (right) and their impact (bottom).

[6,6]-phenyl-C_{61}-butyric acid methyl ester (PCBM)[154,157] or PbI_2[138]. Based on an activation energy of 2.3 eV for the translation of the lead cation[103,151], a rather immobile Pb^{2+} sublattice is assumed.

It is important to understanding the ion movement, because several phenomena result from it as summarized in *Figure 7*. Most prominent and most researched is the scan-rate and scan-direction dependent J-V hysteresis[109,157–160], where a tuning effect of the ion diffusion can be observed. As a result, compared to PSC measurements with reduced hysteresis, improved light-harvesting efficiencies can be achieved in reversed scan direction (from V_{OC} to 0 V), however, forward scan direction shows lower efficiencies. The hysteresis was greatly hampered by the aforementioned passivation procedures, as well as, by redistributing and accumulating ions at the contacts before solar cell characterization using light-soaking[161,162] and pre-poling[163,164]. As a side note, other sources of the hysteresis were speculated to be charge trapping processes or ferroelectricity; both of which were found to be, in fact, consequences of the ion diffusion[157,165,166]. Furthermore, electrochemical impedance spectroscopy measurements show a large capacitance in PSCs under illumination[167], which can also be related to ionic transport within the perovskite film.

If an electric field is applied, the ions accumulate in electrical double layers (EDL) at the ETM and HTM layers. This was directly observed using optical and photothermal

induced resonance microscopy[102,104]. The perovskite film self-dopes, causing a n-type region containing positive charged ions (MA^+) and vacancies (V_I) as well as a p-type region with negative ions (I^-) and vacancies (V_{MA}). As a result, a p-i-n junction is formed and was found to be switchable by reversed poling[106,108–110]. This mechanism is comparable to the *modus operandi* of a light emitting electrochemical cell (LEC). Here, HTM and ETM layers used in LEDs for better and more balanced charge injection are replaced by a ionic-based and, thus, self-doping active layer[168–170]. Using this well-known and studied concept[171–173], the p-i-n formation within pristine perovskite materials can be directly observed (*Chapter 4.1*). In general, ion diffusion causes natural instability of the perovskite lattice, which constrains long-time application of PSCs[105]. Surprisingly, to some extent the perovskite lattice was observed to regenerate when stored in the dark[54,55,106,174].

2.2. Perovskite solar cell

2.2.1. Device architecture

Generally, PSCs have two device architectures: the sDSSC (also mesoscopic PSC) and the thin-film architectures (also planar PSC). Both designs can be applied to a n-type setup, where holes and electrons are collected through the metal anode and conductive glass cathode, respectively. In a p-type setup the charge carrier movement flows *vice versa*.

The standard structure of a sDSSC is composed of five constituents *Figure 8A*:

(i) The incident light is passing through a glass slide (blue) coated with a highly transparent conducting oxide (TCO, grey), for which usually fluorine-doped tin oxide (FTO) or indium-doped tin oxide (ITO) is used. In the case of flexible solar cells, the rigid glass substrate is replaced by polyesters such as polyethylene naphthalate (PEN)[114].

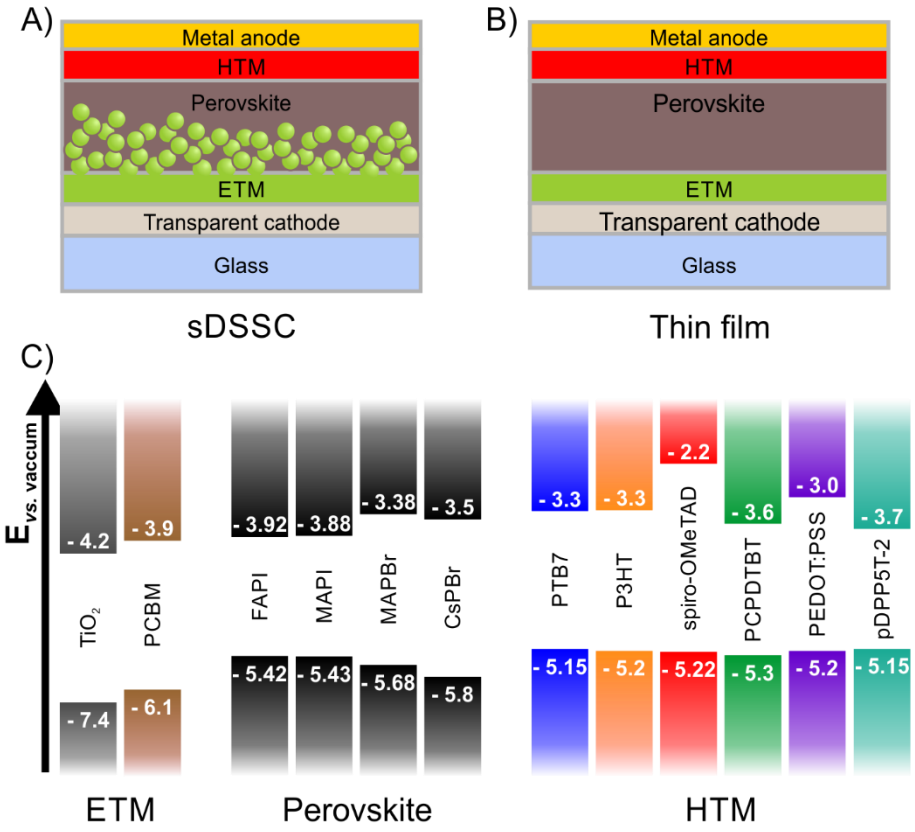

Figure 8. Schematic depiction of the two most common n-type device architectures for PSCs: sDSSC (A) and thin-film (B) setup. C) Energy level diagram of compounds used in this work divided by ETMs, perovskite materials, and HTMs.

(ii) The TCO substrate is coated with a 30-50 nm compact film and a, subsequent, 150-400 nm mesoporous layer of a wide band-gap semiconductor (green). Here, the materials used for n-type PSCs are typically titanium dioxide (TiO_2)[48,73,156,158,175], tin dioxide[176], zinc oxide[177,178], or fullerene dervatives[179–181] and for p-type PSCs nickel(II) oxide[182].

(iii) On top, the perovskite (brown) is deposited. It acts as a dye, meaning it injects the photogenerated electrons into the n-type semiconductor and is "regenerated" by transferring its holes into the HTM. A thick (> 300 nm) perovskite capping layer is beneficial to the solar cell efficiency, as it prevents recombination between the electrons in the ETM and the holes in the HTM[46,183].

(iv) The break-through for PSCs occurred, when the liquid iodine-based redox mediator was replaced by the solid HTM (red) 2,2′,7,7′-tetrakis-(diphenylamino)-9,9′-spirobifluorene (spiro-OMeTAD, *Figure 9*)[73]. Although it requires doping to enable good hole transporting mobilities[184–187], it is one of the best-performing and most employed HTM[48]. Several other materials were tested including polymers such as poly(3-hexylthiophene-2,5-diyl) (*P3HT*), poly[[4,8-bis[(2-ethylhexyl)oxy]benzo[1,2-b:4,5-b']dithiophene-2,6-diyl][3-fluoro-2-[(2-ethylhexyl)carbonyl]thieno[3,4-b]thiophenediyl]] (PTB7), diketopyrrolopyrrole–quinquethiophene (pDPP5T-2), and poly[2,6-(4,4-bis-(2-ethylhexyl)-4H-cyclopenta[2,1-b;3,4-b′]dithiophene)-alt-4,7(2,1,3-benzothiadiazole)] (PCPDTBT)[47,188–190] (*Figure 9*), small molecules like fluorene-dithiophene[175], and, for example, copper(I) iodide[191] and copper(I) thiocyanate[192] as inorganic materials.

(v) The cell is finalized by applying a 70 nm film of gold (Au) or aluminum (Al) as back electrode (yellow).

From the sDSSC architecture derives the meso-superstructured architecture that uses a mesoporous layer of insulating aluminum oxide as a substitute for TiO_2[73]. Instead of injecting the electrons into the scaffold layer, they are carried through perovskite, which is a better transporting material (~ 35 $cm^2\ V^{-1}\ s^{-1}$)[98] compared to mesoporous TiO_2 (0.1-1 $cm^2\ V^{-1}\ s^{-1}$)[193], before they are collected at the compact layer. Despite the benefit of hampering charge carrier recombination by TiO_2[194,195], having the charge carriers move though perovskite itself reduces not only the collection time, but also improves the V_{OC}[73,183]. The latter is a result of the mesoporous TiO_2 film being a macroscopic

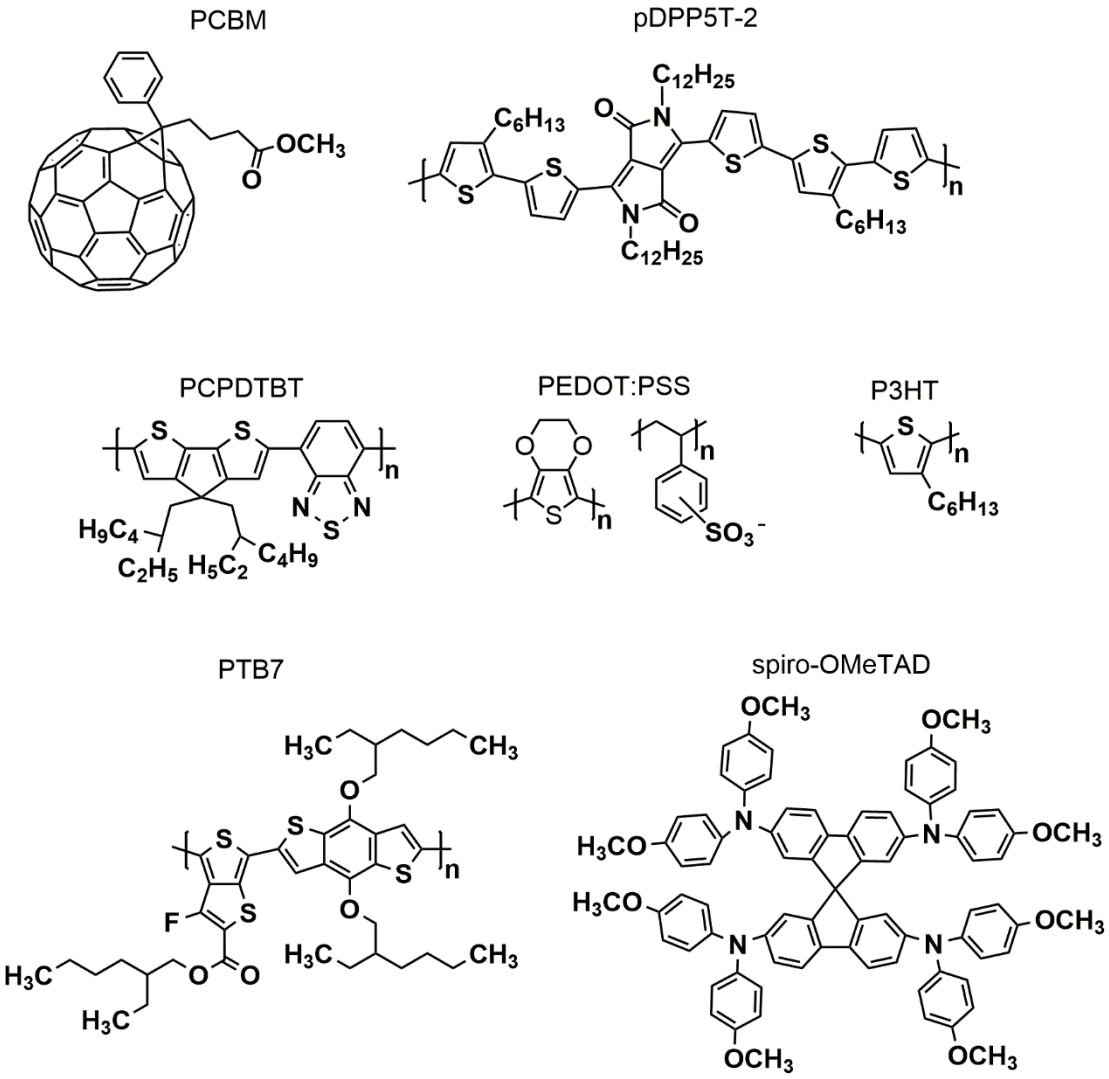

Figure 9. Structural formulae of ETM PCBM as well as HTMs pDPP5T-2, PCPDTBT, PEDOT:PSS, P3HT, PTB7, and spiro-OMeTAD, which were used in this work.

chemical capacitor, where a trail of the density of states extends into the band-gap and, under illumination, can be filled with electrons[196]. The consequential quasi-Fermi level for electrons (E_{Fn}) is lower than the CB for any given charge density, which, with a rising E_{Fp}, also applies to HTMs, and can be inhibited by using highly crystalline semiconductors[197] (*Chapter 4.2.2*).

Alternatively, trapped electrons within TiO_2 can be avoided by a light harvesting material that also acts as formidable semiconductor, such as perovskite. This approach resulted in the implementation of the thin-film architecture (*Figure 8B*) that has only a thin compact film but neither a mesoporous nor a scaffold layer [180,198,199]. This planar structure enables low-temperature fabrication or flexible devices[200–202] and can, additionally, be used for lighting technologies[87,88]. The p-type configuration of the

planar PSC is also known as inverted-planar PSC and is the third most common architecture. Here, poly(3,4-ethylenedioxythiophene) polystyrene sulfonate (PEDOT:PSS)[201] or poly(triaryl)amine (PTAA)[179] are implemented as HTMs and PCBM is used as ETM.

2.2.2. Working principle

The working principle of a n-type mesoscopic PSC is summarized in the schematic representation given in *Figure 10*. After excitation (1) with either long- (blue arrow) or short-wavelength (purple arrow) light, several processes take place at the HTM/perovskite and ETM/perovskite interfaces (*Figure 10A* and *B*) as well as within perovskite's bulk (*Figure 10C*). Green arrows indicate the favorable flow of charge carriers that leads to the generation of electricity (*Figure 10A*). However, several undesired recombination pathways lower the overall efficiency, which are indicated by in red arrows (*Figure 10B*).

After ultrafast free charge carrier generation, electrons and holes with excess energy thermalize (2) within 1-10 and 0.1-0.5 ps[147,148], respectively (*Chapter 2.1.4*). By using a crystalline material with a large interface, as it is presented in *Chapter 4.2.2*, hot electrons are partly harvested (3) before thermalization[179]. In general, the timescale for the charge carrier injection process of electrons into the ETM (3) or holes into the HTM (4) is under heavy debate. The temporal range for electron transfer into TiO_2 stretches from between 0.2[203] to 400 ps[136,194]. The injection of holes into HTMs were reported to be 0.7[203,204] or 660 ps[136] for spiro-OMeTAD, to even several ns for P3HT[205]. *Chapters 4.2.2* and 4.2.3 of the work at hand address the kinetics and mechanism of charge carrier transport within PSC and corroborate sub-picosecond injection. Subsequently, it takes several milliseconds (ms)[194] for electrons and holes to diffuse though the respective layers, before they are collected at the electrodes (5).

The efficient collection of photogenerated charge carriers at the electrodes is hindered by loss processes. For instance, the electrons in the ETM's CB can recombine with the holes in the perovskite's VB (6) – either from the bulk (~ 100 microsecond, µs)[183,195] or *via* charge traps within the mesoporous layer (~ 1 µs)[206]. The analogous recombination process occurs at the perovskite/HTM interface, where electrons of the perovskite's CB recombine with injected holes within the HTM's VB (7, ns-µs)[189]. Recombination between electrons in the ETM and holes in the HTM is avoided by using a perovskite

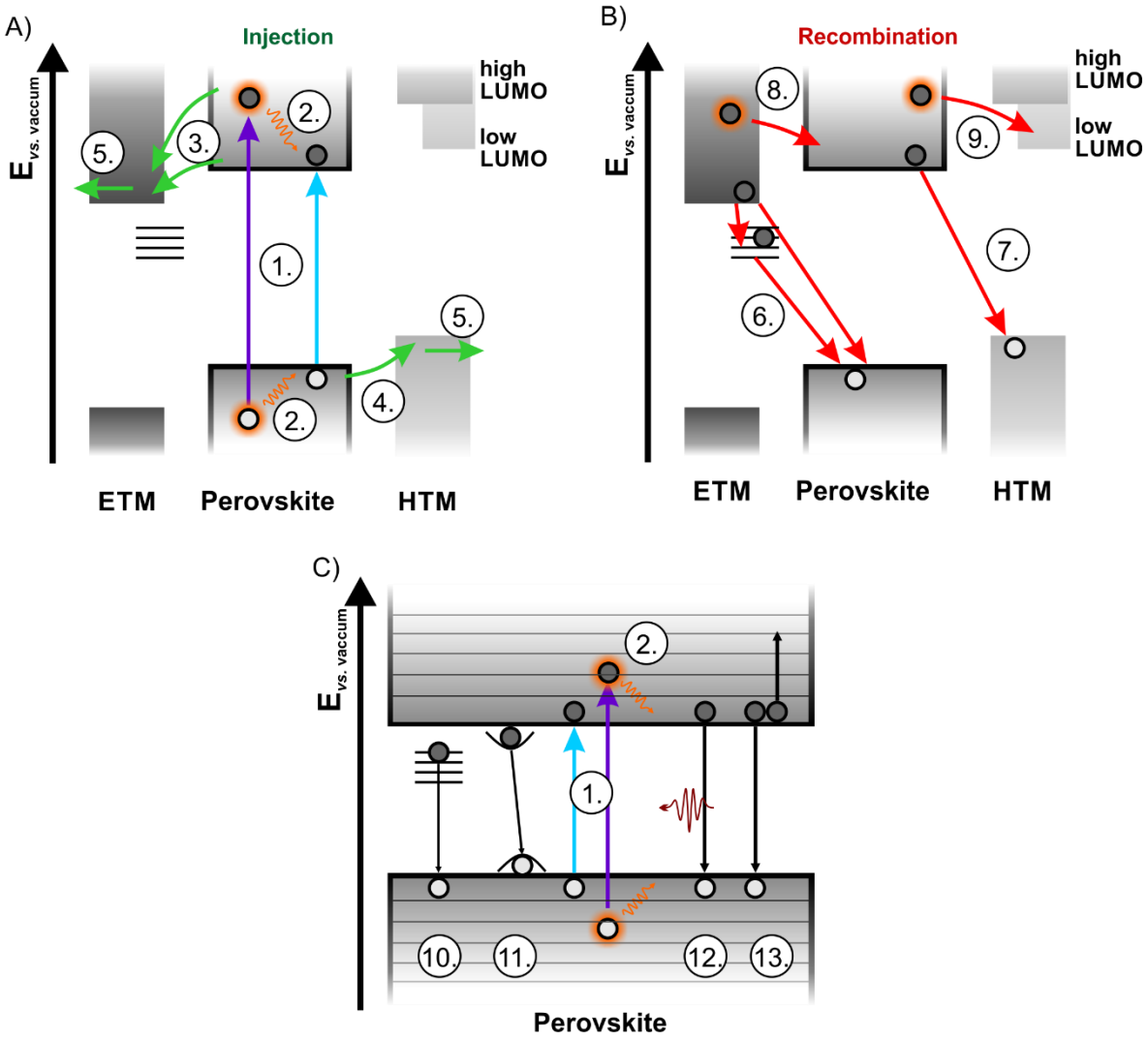

Figure 10. Schematic representation of charge carrier pathways at the ETM/perovskite and perovskite/HTM interface with favorable processes that lead to power conversion (A) and undesired recombination processes that lower the overall efficiency (B). C) Schematic representation of processes taking place within perovskite's bulk.

capping film with a sufficient thickness[183]. In the work at hand, we report on further loss pathways related to hot electrons (*Chapters 4.2.2* and 4.2.3). Here, already injected hot electrons back-transfer within the ETM into the perovskite's CB within the first 10 ps (8). Furthermore, by using an HTM with a low LUMO such as PCPDTBT, the power conversion efficiency is reduced by a loss transfer that originates from hot electron injection into the HTM (9).

Not all of perovskite's electrons (holes) are injected into TiO_2 (HTM)[189,207], and the remaining electrons either diffuse though the perovskite film towards the electrode, like in a meso-superstructured architecture, or recombine. In polycrystalline perovskite films with many grain boundaries, trapped charge carriers exhibit a lifetime of up to

milliseconds (10)[208]. During the first picoseconds after excitation, moving charge carriers self-trap within the deformation of the crystal structure resulting in the formation of large polarons[149] (*Chapter 2.1.4*). These polarons are the reason for perovskite's nearly microsecond long-lived charge carriers (11) and are favored at higher temperatures (≥ 290 K)[150]. Upon cooling, the ratio between large polarons and free charge carriers shifts towards the latter and, in turn, radiant bi-exponential recombination as seen in increasing PL intensities becomes the dominant recombination process (12, 100-500 nanoseconds)[150,189]. Using high illumination intensities, e.g. high laser fluences in fs-TAS measurements, the large carrier density induces Auger heating, which decelerates energy loss by phonon-emission (13, 30 ps)[96].

3. Instruments and methods

Two major measurement techniques were used to elucidate the fundamental processes within perovskite devices. Firstly, ion diffusion was investigated using static and dynamic electrochemical impedance spectroscopy (EIS). Secondly, femto-second transient absorption spectroscopy (fs-TAS) was employed to observe short-lived species. This provided information on carrier generation and recombination processes. The results of the model system used for fs-TAS were then related to the figure-of-merits obtained by J-V characteristics performed by collaborators.

3.1. Electrochemical impedance spectroscopy

The overall efficiency of a solar cell is dependent on charge carrier transfer and transport processes between and within its components. These are examined by EIS through investigating the resistance (R) and capability to store electrons within a component or across an interface as well as dynamics of chemical reactions at a surface[209–211]. The frequency-based approach of EIS, furthermore, allows a differentiation between electronic charge carrier transport processes, intrinsic ionic motion within a mixed electronic-ionic conductor, and diffusion controlled reactions.

In potentiostatic EIS, a sinusoidal alternating voltage (V_{ac}) is applied to an electrochemical cell and the response of the investigated system is measured in an alternating current (AC) signal (I_{ac}). In order to allow a linear response that only impacts the phase and not the magnitude of the applied signal, a small amplitude perturbation of a few millivolt is used. By varying the frequency (f), different processes resonantly react to the oscillating voltage according to the species' diffusion rate. In this way, the impedance (Z), the resistance and reactance by means of magnitude and phase angle (φ) shift, is recorded according to

$$Z = \frac{V_{AC}\sin(\omega t)}{I_{AC}\sin(\omega t + \varphi)} \qquad (1)$$

where ω = 2πf is the angular frequency.

This can be expressed in a Cartesian form (*Equation 1*) by applying Euler's relationship, where Z is composed of a "real" in-phase (Z') and an "imaginary" out-of-phase part (Z'').

$$Z = |Z|e^{i\varphi} = Z' - iZ'' \quad (2)$$

with i being the imaginary unit.

The current response is a mixed contribution of three electric circuit elements. For an ideal resistor that follows Ohm's law the electrical current is directly proportional to the applied voltage (*Equation 3*) with its resistance being independent of the current intensity, direction, and whether a direct (DC) or alternating current is used. The response is always in phase and, thus, it represents the real impedance Z'.

$$V = R \times I \quad (3)$$

The second element is the ideal capacitor that stores electrical energy within an electric field. The current response is out-of-phase by 90° compared to the applied AC voltage and it, hence, represents the imaginary impedance Z''. A capacitance (C) is recorded when two highly conductive layers, e.g. electrodes, at a distance d and the geometric area A_g sandwich a non-conducting (dielectric) medium. C is then described by

$$C = \frac{\varepsilon_0 \varepsilon_R A_g}{d} \quad (4)$$

where ε_0 and ε_R are the permittivity in vacuum (8.85 x 10^{-12} Faraday m^{-1}) and in the dielectric medium.

While the corresponding current in a capacitor is leading compared to an in-phase response, the current influenced by the third element, the inductor, is lagging. Hence, a capacitor and an inductor have phase angles with opposite sign.

In *Chapter 4.1*, the formation of electrical double layers is investigated by EIS assays. Double layers are imperfect capacitors due to a non-uniform current distribution caused by surface and/or bulk heterogeneities[173,212]. In this case, the capacitance is replaced by the constant phase element (CPE) with an impedance described by *Equation 5*.

$$Z_{CPE} = \frac{1}{Q(i\omega)^n} \quad (5)$$

Although Q cannot be directly associated to any physical value, it depends on n; Q is a pure capacitor for n = 1 or a pure resistor for n = 0. For any value in between, the effective capacitance (C_{eff}) is derived by *Equation 6*[212].

$$C_{eff} = Q^{1/n} R^{(1-n)/n} \quad (6)$$

The EIS data is usually presented in a Nyquist plot, where the imaginary Z'' is given as function of the real Z' (*Figure 11A*) and the impedance is described as a vector with the length |Z| and the angle φ. The Nyquist plot of a device features typically the same number of semicircles as frequency-resonant interfaces are present in the device. In the fitting model, each semicircle is correlated to a pair of parallelly connected resistance and capacitance elements. To depict the frequency-dependence of |Z| and φ, Bode modulus and Bode phase plots (*Figure 11B*) are used, respectively.

For mixed electronic-ionic conductive systems such as the active layer of a light-emitting electrochemical cell or a hybrid perovskite material, EIS is used to investigate the changes of the conductance and capacitance upon applying a bias[171,172,213]. This behavior is related to the ionic diffusion induced by the external electric field, which causes the formation of electrical double layers (EDLs) and doped regions. Consequently, the medium becomes more conductive or, as it is the case for LECs, the ion accumulation leads to balanced charge injection[171–173]. EIS on hybrid and inorganic perovskites were measured in two types of experiments. In static EIS, the impedance is obtained at different applied voltage values. Here, two different behaviors are expected when measuring below – where only EDL formation is present – and above the band-gap, where, additionally, p- and n-type doping occurs. In dynamic EIS, a constant voltage is applied and, subsequently, the impedance is measured at given time intervals. In this way, the changes caused by the ionic diffusion within the observed material are recorded over time. The models used for data fitting in this work are given in *Figure 11D* with the part in black being used for static and the full model used in dynamic EIS assays. The circuit elements incorporated in the model are i) a series resistor (R_s) that includes the resistance values of the ITO, the cables, and clamps used for contacting the device, ii) the electrical (R_e) and ionic resistance (R_i), iii) the CPE of the active layer (CPE_{geo}) and the sum of both EDLs (CPE_{EDL}), as well as iv) the inductance caused by the cables (L_{cab}). The conductance (G) and capacitance at a given frequency can be determined by

$$\frac{1}{Z} = G(\omega) + i\omega C(\omega) \tag{7}$$

By plotting G and C as a function of the frequency (*Figure 11C*) the effects of the ionic diffusion over an increased voltage or over time are monitored in detail. At an oscillating

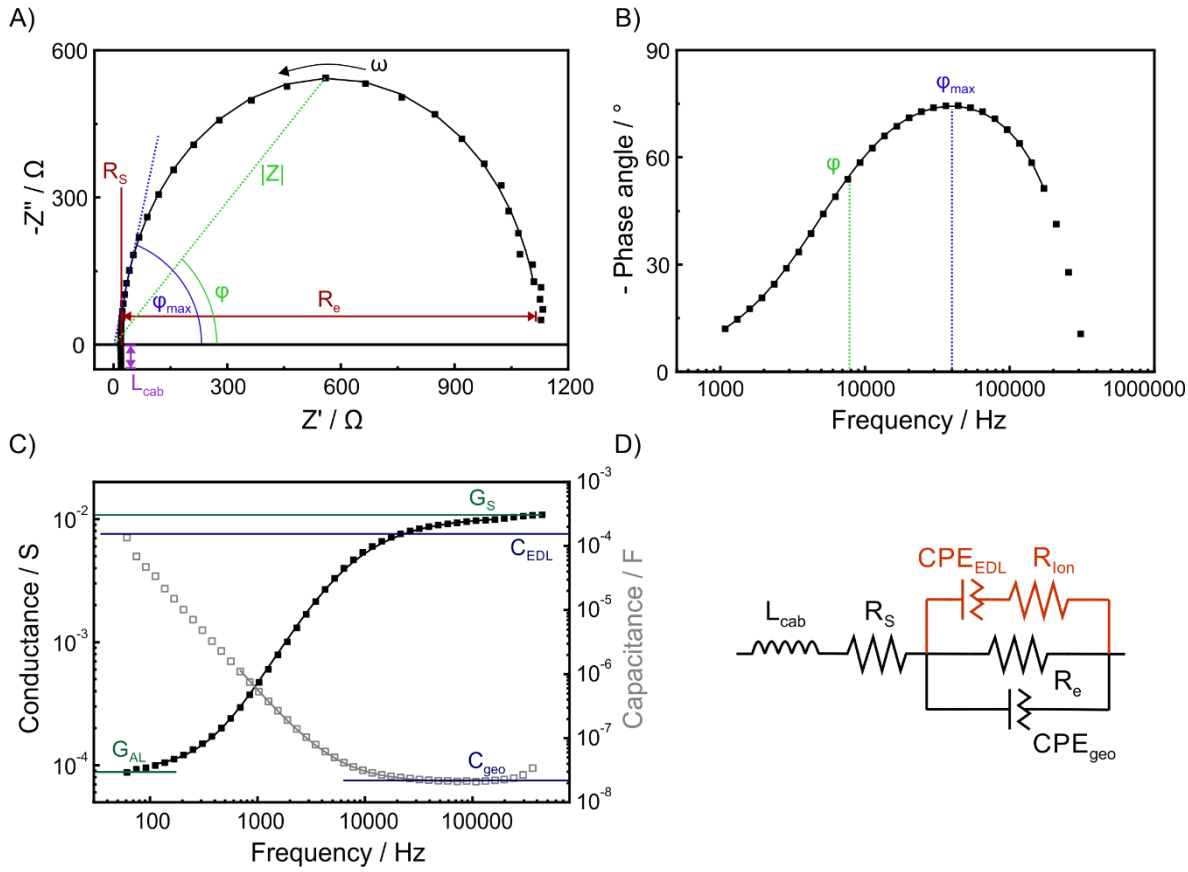

Figure 11. Exemplary Nyquist plot (A) and Bode phase (B) of a hybrid perovskite at an applied voltage of 1.5 V with highlighted series (R_S) and electrical resistance (R_e), phase angle φ as well as inductive contribution of the cables, L_{cab}. C) The conductance and capacitance of $MAPbBr_3$ at an applied voltage of 0 V is given as a function of frequency with assigned contributions. D) Circuit model used for fitting of the static (black) and dynamic (black and dark orange) EIS assays.

voltage around 0 V, the conductance according to R_S is seen as a plateau in the high frequency region, while the plateau at lower frequencies represents the conductance of the pristine active layer (G_{AL}). Upon applying a voltage, G_{AL} increases due to the formation of EDLs and/or doped regions. C_{geo} relates to the geometric capacitance of the active layer, while the capacitance of the EDLs (C_{EDL}) is derived at very low frequencies. Due to instability effects for frequencies below 100 Hz, a complete picture of the ionic diffusion is not given.

3.2. Femto-second transient absorption spectroscopy

Femto-second transient absorption spectroscopy (fs-TAS) is a technique to characterize photoinduced transient processes. Here, emissive as well as non-emissive states of photoexcited molecules in solution or in solid state are studied[214,215].

The obtained differential absorption spectra provide information on the mechanisms following photoexcitation with a sub-picosecond resolution. These include, in general, conformational changes, solvation effects, chemical reactions, as well as energy and charge carrier transfer/separation processes. For efficient harvesting of the absorbed energy in a solar cell, charge carrier transfer processes, in particular, have to be fast in order to compete with loss pathways such as internal conversion, intersystem crossing, and fluorescence.

The measuring principle of fs-TAS is based on two laser pulses with a pulse width of about 150 fs. The pump pulse with an excitation wavelength of λ_{exc} promotes a fraction (typically 0.1-10%) of the molecules to an electronically excited state according to the Frank-Condon principle. A weak white probe pulse measures the ground state absorption reference spectrum as well as the excited sample with a delay time in respect to the pump pulse in a range spanning from 400 – 780 (visible range) and 780 – 1400 nm (near infrared, NIR, range). For the reference spectrum, a chopper blocks every second excitation pulse. The attenuation in the transmission is given as the difference in the optical density (ΔO.D.), *Equation 8*, which is derived by subtracting the absorption spectrum (*Equation 9*) of the ground state (I_u) from the absorption spectrum of the excited sample (I_p). The absorption of the specimen is derived by measuring the initial light intensity (I_0) and the light intensity after passing through the sample (I).

$$\Delta O.D.(\tau) = -lg\left(\frac{I_p(\tau)}{I_u}\right) \tag{8}$$

$$O.D. = -\lg(T) = -lg\left(\frac{I}{I_0}\right) \tag{9}$$

By changing the delay time between excitation and probing from 200 fs to 7 ns, the differential absorption profile assays are arranged in a (m × n) matrix data set, where the rows (m) and columns (n) are given by the probed wavelengths and the delay time, respectively.

The features are generally visible in a differential absorption spectrum and represented in *Figure 12*:

(i) *Ground state bleaching* (GSB): Upon excitation, a fraction of the molecules is promoted to the excited state leaving fewer molecules in the ground state.

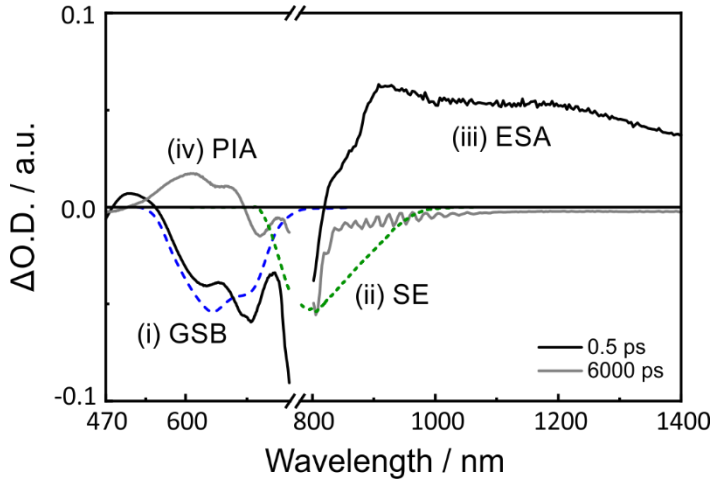

Figure 12. Exemplary differential absorption spectra after a delay time of 0.5 ps (black) with contributions of the GSB (blue), the SE (green), and in the NIR of the ESA, as well as after a delay time of 6000 ps (grey) with a formed feature between 500 and 700 nm related to the PIA, here triplet excited state.

Thus, the ground state absorption in the excited sample is lower compared to the reference spectrum. This leads to a negative signal in the differential absorption spectrum within the wavelength region of the ground state absorption, also known as ground state bleaching.

(ii) *Stimulated emission* (SE): Using a pump pulse with enough energy, its photon induces emission of a photon from the excited molecule, which consequently falls back into the ground state. As the emitted photon has the same direction as the photon of the excitation pulse, the light intensity perceived by the detector is increased and a negative signal is obtained in the differential absorption spectrum. This process cannot be initiated by the weak probe pulse and only occurs for optically allowed transitions. Hence, the spectral profile of the SE follows the fluorescence spectrum of the excited molecule and is Stokes shifted with respect to the GSB.

(iii) *Excited-state absorption* (ESA): When the excited molecule absorbs additional photons provided from I_p, it is promoted to a higher excited state. As the states are populated in excited molecules but not in molecules in their ground state the feature in the differential absorption spectrum is positive.

(iv) *Photoinduced absorption* (PIA): The charge carriers within the excited molecule can participate in transitions that result in transient or longer lived states, such as charge separated, triplet excited, and isomerized states, as well as products after a photochemical process. The PIA in the differential

absorption spectrum is positive, as the state is not populated in the molecule's ground state.

A typical differential absorption spectrum of perovskite after a delay time of 1 ps is shown in *Figure 13A*. Highlighted features represent the processes presented in *Figure* 13*B*. Two GSB signals are located at 760 and 460 nm, and reflect the two onsets seen in the steady state absorption spectra. Flender *et al.* performed ultrafast fs-TAS studies that recorded differential absorption spectra at shorter delay times than 20 fs[216]. Here, GSB dominates the whole visible range mirror-imaging the steady-state absorption. The feature at 760 nm (3, red) represents the band-gap transition $VB_1 \rightarrow CB_1$ and due to hot carrier distribution extends asymmetrically towards shorter wavelengths[96,217].

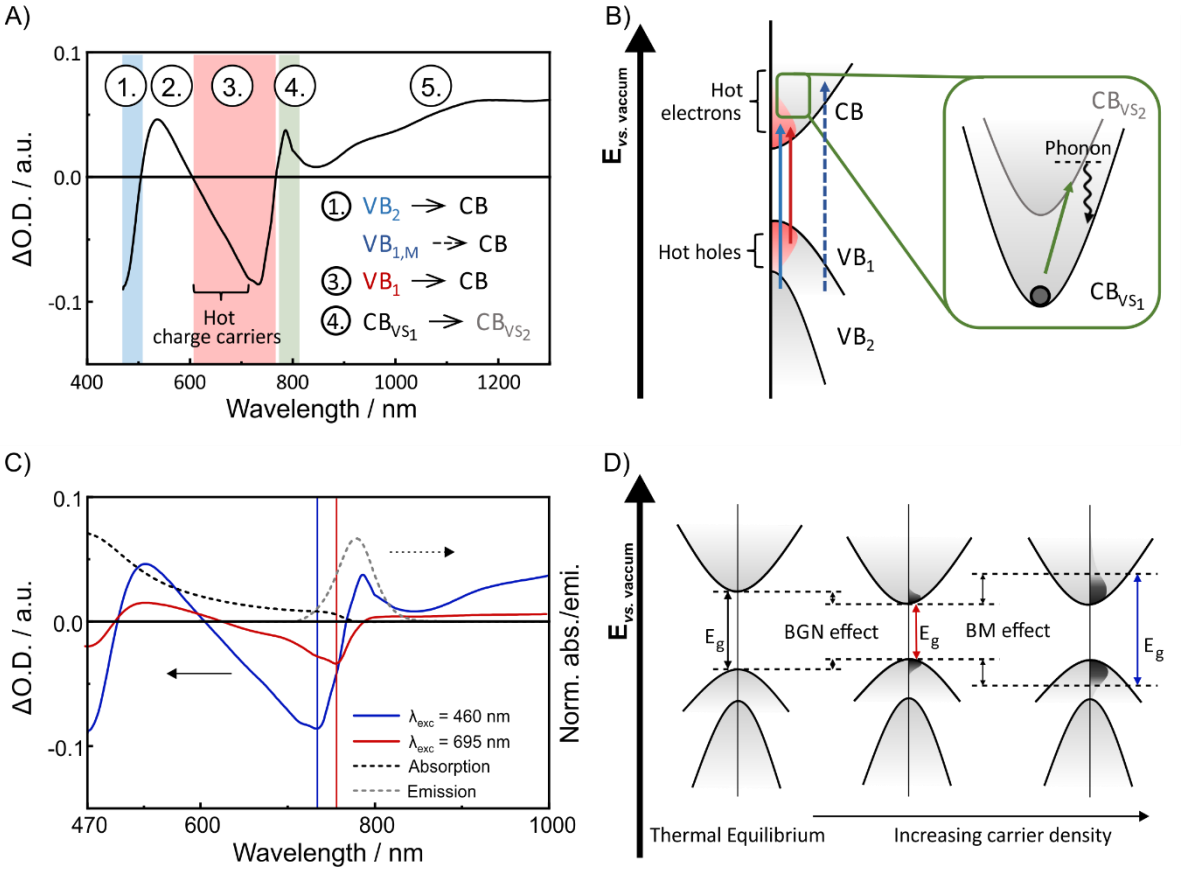

Figure 13. A) Differential absorption spectrum after a delay time of 1 ps with characteristic features of MAPI upon excitation with 460 nm. Highlighted features relate to the schematic depiction of processes (B) investigated in the work at hand. C) Differential absorption spectra after a delay time of 1 ps upon excitation with 460 (solid blue) and 695 nm (solid red) as well as normalized steady state absorption (dashed black) and emission (dashed grey) as reference. D) Schematic representation of the band-gap renormalization and Burstein-Moss effects on the band-gap upon increasing carrier density with their impact highlighted in (C).

The GSB at 460 nm (1, blue) is still heavily debated on and has most likely contributions of two transitions at 480 and 460 nm related to $VB_2 \rightarrow CB_1$ at the *R* point and $VB_1 \rightarrow CB_1$ at the *M* point in the Brillouin Zone, respectively (*Chapter 2.1.3*)[95].

According to Flender *et al.* and Price *et al.*, after 20 fs, a PIA signal emerges between 500 and 650 nm (2) as a result of carrier-induced changes of the refractive index[216,217]. Intraband ESA is visible as a short-lived (~ 6 ps) PIA signal (5) in the NIR with a maximum at 930 nm[218,219]. Upon using a pump pulse with a high laser fluence, LO phonon emission provokes a transition of an electron from an energetically lower to an energetically higher vibration state (VS). This intra subband ESA can be investigated as ultrashort-lived (~ 1.5 ps) PIA signal at 780 nm (4, green)[217,220]. For MAPI, the emission maximum peaks at 778 nm (*Figure 13C*, grey dashed line) and, hence, the SE is partly superimposed by the hot carrier PIA as well as by the output (775 nm) of the titanium-sapphire laser.

Exciting a semiconductor with excess energy generates a high charge carrier density, which dopes the semiconductor itself. Consequently, many-body and state-filling effects influence the dynamics of the charge carriers leading to a red- and blue-shift of the GSB minimum in differential absorption spectra, respectively (*Figure 13C* and *D*)[217,221]. For high charge carrier concentrations in solid states, the Pauli principle prohibits two electrons with identical spins to occupy the same unit cell, while Coulombic interactions maximize the spacial distance between carriers with identical charge. The repulsive electrons and holes create sub-band-gap states, which lower the CB and increases the VB, respectively. This so-called band-gap renormalization, in turn, decreases the band-gap energy and causes a red-shift in the GSB minimum (*Figure* 13*C* and *D*, red) compared to its absorption onset[96]. Upon increasing the excitation energy further, density of states available for occupation are filled and charge carriers are transitioned from/into energetically higher VSs. This band filling model, also known as Burstein-Moss effect, blue shifts the GSB minimum (*Figure 13C* and *D*, blue)[137]. Both band-gap normalization and Burstein-Moss effect usually cancel out each other.

3.2.1. Multi-wavelength target analysis

For more complex systems, such as solar cells, a multi-wavelength analysis that fits specific wavelengths multi-exponentially is insufficient to derive lifetimes and rates. Instead, the fs-TAS data set collected in a matrix correlated to the probed wavelengths and the delay time can be analyzed and fitted using statistical analysis packages and methodologies. For sequential deactivation processes, global analysis evaluates the data matrix by a set of exponential functions and provides a species associated spectrum as well as its corresponding lifetime τ_i for each transient state according to

$$\Delta O.D.(\lambda,\tau) = \sum_i A_i(\lambda) \times e^{\frac{-t}{\tau_i}} \quad (10)$$

where $A_i(\lambda)$ is the amplitude to describe the decay associated spectrum.

Yet, this requires states to be parallelly or sequentially accessible. At interfaces of solar cell components, charge carrier transfer processes are more complex and require a more sophisticated model. Here, multiple component excitation, branching injection, back-transfer, and different recombination pathways can be considered in a target analysis[222]. By applying the knowledge gained from preliminary characterization – i.e. steady-state absorption and emission, spectroelectrochemistry, triplet-sensitization as well as time-resolved spectroscopy, a deactivation model is established and further elaborated in the interpretation process.

3.3. Current density voltage characteristics

The power conversion efficiency (PCE) of a solar cell and its figure-of-merits is evaluated from J-V characteristics as follows[223]. For this, the voltage is steadily scanned while recording the current response (*Figure 14A*). Under open circuit conditions, when no current is flowing, the maximal photovoltage V_{OC} is reached. At short circuit, i.e. 0 V, the highest obtainable photocurrent density J_{SC} is obtained. The power (P) of the solar cell at any voltage value is calculated by

$$P = J * V \quad (11)$$

The fill factor (FF) provides information on the quality of the solar cell. When having a high shunt and a low series resistance, the fill factor is high and approaches optimum device conditions. It is obtained by

$$FF = \frac{J_{MPP} \times V_{MPP}}{J_{SC} \times V_{OC}} \quad (12)$$

where J_{MPP} and V_{MPP} are the current density and voltage at the maximum power point (MPP).

The power conversion efficiency (PCE, η) of a solar cell is defined as:

$$\eta = \frac{P_{MPP}}{P_{light}} \quad (13)$$

with P_{MPP} being the maximal obtained power by the solar cell and P_{light} the radiant power of the light source. For universal test conditions P_{light} was set as 1000 W m^{-2} and a standardized solar spectrum that considers sunlight absorption by the Earth's air mass at a solar zenith angle of 48.2°. Hence, the PCE can also be determined by

$$\eta = J_{SC} \times V_{OC} \times FF \quad (14)$$

For devices with polarizable material, such us perovskite-based solar cells, hysteresis can occur in the J-V characteristics (*Figure 14B*). The figure-of-merits are, hence, given for both forward (from 0 V to V_{OC}) and reversed scan direction (from V_{OC} to 0 V)[158].

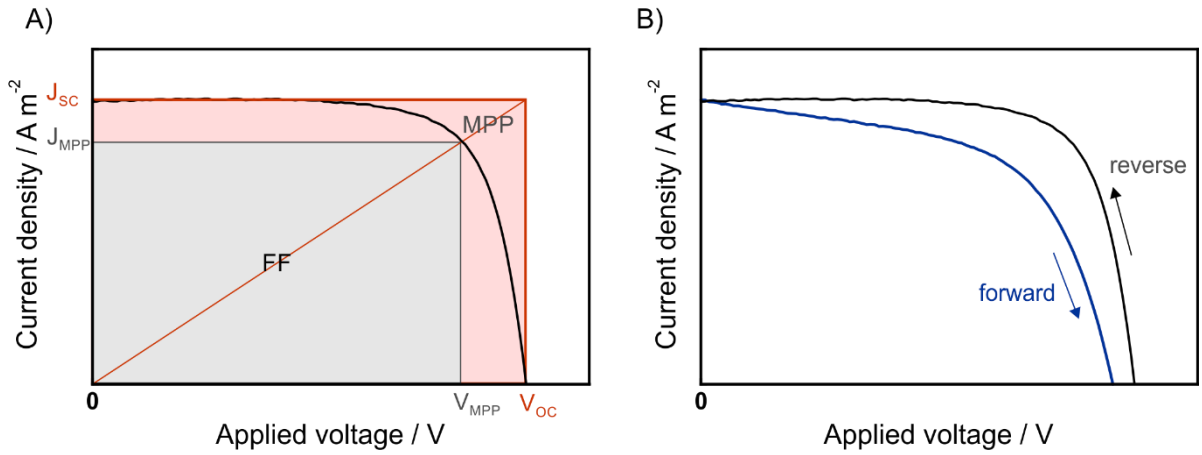

Figure 14. A) Exemplary J-V characteristics (black) including J_{SC} and V_{OC} (red) and J_{MPP} and V_{MPP} (grey) as well as the respective areas for calculating the FF. B) Exemplary J-V characteristics with hysteresis upon measuring in forward (blue, from 0 V to V_{OC}) and reversed scan direction (black, from V_{OC} to 0 V).

4. Results and discussion

In the first part of this chapter, we use EIS assays as described in *Chapter 3.1* to investigate ion diffusion within hybrid and inorganic perovskite materials. In the second part, we focus on the charge carrier transfer mechanism at ETM/perovskite and HTM/perovskite interfaces studied by fs-TAS as established in *Chapter 3.2* and elaborate novel injection processes.

4.1. Unveiling the dynamic processes in hybrid lead bromide perovskite nanoparticle thin film devices

B. M. D. Puscher, M. F. Aygüler, P. Docampo, R. D. Costa, *Advanced Energy Material*, 2017, **7**, 1602283.

The nature of perovskite being both an electric semiconductor and an ionic conductor was first reported by Mizusaki *et al.* in the 1980s[64], yet, the interest of the scientific community arose only after ion migration was shown to be associated to the scan-rate dependent J-V hysteresis in 2014[158,160]. Under an applied bias and upon illumination, interstitial ions and their related vacancies are produced from the soft crystal structure and diffuse out of and along the crystal lattice, respectively (*Chapter 2.1.5* and *Figure 7*)[151–153]. The charge carriers accumulate at the interfaces of perovskite with either a charge carrier transport layer or an electrode, which screens the electric field and, in turn, either facilitates or impedes charge carrier extraction. This, on the one hand, typically leads to immediate improved power conversion efficiencies when measuring in reverse (V_{OC} to 0 V) scan direction or when using device preconditioning by exposing the PSCs to poling or light soaking before characterization[101,164]. On the other hand, ion diffusion is considered to initiate the degradation of PSCs[101,104,224] and perovskite-based LEDs[225], as indicated by a fast drop of power conversion efficiency and luminous efficiency, respectively. The diffusion of halides in HIOPs such as MAPI was in the focus of attention from the beginning[103,158], while the organic cation was thought to realign as a response to the electric field but to abide within the cavity of the $[PbX_6]^{4-}$ octahedrons[104,124] as it is the case for ABO_3-type perovskites[226]. In order to overcome this intrinsic stability challenge, ion movement is studied to open ways to suppress the underlying processes without impacting perovskite's optoelectronic properties.

For investigating the ion diffusion processes, we turned towards light-emitting electrochemical cells (LECs), which are a well-understood thin-film ionic-based lighting technology and an ideal model system to study ionic drifts. In contrast to LEDs that need several HTM and ETM layers for better and more balanced charge carrier injection into the electroluminescence layer, the active layer of LECs consists of a solid ionic conductor containing electrolyte additives and an electroluminescence species[168–170]. Upon applying a voltage, the ionic additives redistribute by diffusion in the ionic conductor and, in turn, introduce an electrical double layer (EDL) of uncompensated ionic charges. These EDLs self-regulate the electric field close to the contact for facilitated charge injection. Furthermore, the active layer self-dopes forming a p-i-n junction with highly conductive p- and n-type doped regions and a depletion region where the charge carriers radiantly recombine. For an ionic-electronic material such as perovskite, the electrochemical doping model of LECs is transferable. We investigated octylammonium capped hybrid organic-inorganic $MAPbBr_3$ (MAPB) NCs as well as inorganic perovskite $CsPbBr_3$ (CPB) NCs samples prepared by Dr. Meltem F. Aygüler[87,106] in a ITO/PEDOT:PSS/perovskite/Al architecture (*Figure 15A*)[106].

Under an externally applied constant voltage of 4 V (*Figure 15B*), the time-dependent response of the current (black marks) rises until a run time of 6 hours (h) is reached. The tri-exponential increase represents the lowering of the resistance within the perovskite through the formation of EDLs and doped regions. Bromide anions and their

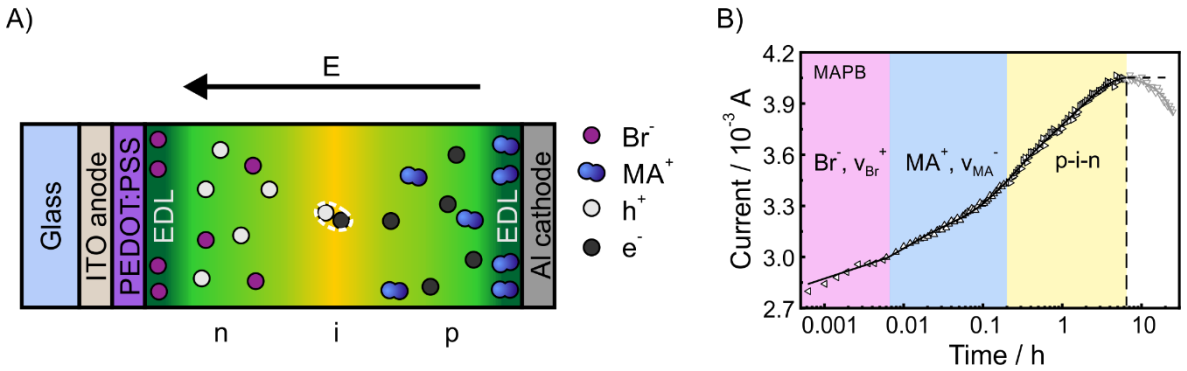

Figure 15. A) Schematic representation of the device including the electrochemical doping model with electronic (hole, h^+, as white and electron, e^-, as black circular area) and ionic (Br^- as purple circular area and MA^+ as blue structure) as well as EDLs (dark green), n- and p-type doped regions (light green), and depletion region (yellow). B) Current response of the MAPB device upon applying a constant voltage of 4 V over 24 hours. The halide (purple) and organic cation (blue) diffusion as well as p-i-n junction formation (yellow) are highlighted. The onset of degradation is marked with a dashed vertical line, while the dashed horizontal line represents the development of the current for an ideal, degradation-free device. Adapted from Puscher *et al.*[106].

vacancies V_{Br} (purple), which have the lowest activation energy of the three species within perovskite, are the fastest migrating species. The derived diffusion time of 30 ± 1.5 s is in agreement with a response time of a few seconds that was observed in photocurrent relaxation measurements[158] as well as time-dependent PL imaging of MAPI[110] and MAPB[104] bulk thin-film solar cells. MA^+ cations and their vacancies, V_{MA}, have higher diffusion activation energies compared to the halides. Their diffusion is, thus, expected to be slower and we attribute the second time constant of 12 ± 0.4 minutes (min) to their migration towards the interface. This represents the accumulation time found in another time-dependent PL imaging of MAPI[227], where, however, the authors do not consider cation but do consider halide diffusion. After the formation of the EDLs, a further increase of the conductance is related to the growth of n- and p-type doped regions[168,171–173,228], which gives the third time constant of 1.6 ± 0.1 h. In an optimum LEC, the current profile reaches a plateau at which it operates at stable and efficient conditions (dashed horizontal line, *Figure 15*). For the perovskite, however, the current (grey marks) decreases after 6 h (dashed vertical line). This is possibly caused by overoxidation and/or reduction processes, which degrade the material, or due to the generation of pinholes by an inhomogeneous distribution of the electric field strength within the morphology of the thin-film[229,230].

For long-term studies of the device behavior, we turned towards pulsed current driving schemes where the average voltage response upon applying a set current and 0 A in 500 µs intervals is measured. This drastically slows degradation and allows investigation of the ion redistribution within a time frame of one day. Here, the average voltage response over time follows a tri-exponential increase, which is, interestingly, independent of the applied current (*Table 1*). For τ_1 and τ_2 this is intuitive, since the activation energy for ion diffusion is exceeded. The time constant for the formation of the doped region is, however, also comparable with increasing electric field when going from 10 to 80 mA. Hence, the growth of the doped region appears to be solely ruled by the electronic conductivity of the perovskite as the electric field is efficiently screened at the perovskite/electrode interface[168,228,231,232].

The improved continuity in the measurement provided by the pulsed driving scheme allows the investigation of the ion diffusion within inorganic CPB NCs. Here, τ_1 is halved in relation to τ_1 of MAPB. A study by Zhou *et al.* published a few months after ours sheds light on this matter: they investigated the illumination-dependent ion motion of

hybrid and inorganic perovskite[57]. They found light intensity independent activation energies for $CsPbI_2Br_1$ (~ 0.45 eV) that are lower compared to MAPI in the dark (0.62 eV); only under illumination the activation energies of the ion diffusion are lower for the HIOP perovskite[57]. In contrast, τ_2 of CPB NCs is longer than for MAPB NCs owing to a less fluid **A** cation of the inorganic perovskite[146] and, in turn, slower diffusion of the Cs^+ (*Table 1*). Due to an earlier degradation of the inorganic film upon polarization (~ 40 min), a τ_3 was not obtained.

Table 1. Time constants obtained from applying different pulsed currents.

Perovskite type	Pulsed current [10^{-3} A]	τ_1 [s]	τ_2 [min]	τ_3 [h]
MAPB	10	16 ± 0.6	4.9 ± 0.4	1.6 ± 0.1
	20	18 ± 1.0	5.1 ± 0.3	1.5 ± 0.1
	50	21 ± 1.1	4.2 ± 0.5	1.1 ± 0.1
	80	15 ± 0.5	5.4 ± 0.2	1.6 ± 0.1
CPB	10	10 ± 0.8	12.0 ± 2.3	-
	20	6 ± 0.2	8.1 ± 0.2	-

To unambiguously determine whether the obtained time constants are caused by two different diffusion species or by the architecture of the device, we turned towards electrochemical impedance spectroscopy. Here, electronic and ionic charge carriers of a mixed conductor are differentiated by the probed frequency according to the concept of ionic diffusion processes within LECs[171–173]. For this, two different measuring modes were used and the data was fitted using the circuit models given in *Chapter 3.1*.

In a steady EIS assay, the impedance was obtained by increasing the voltage from 0 to 4.5 V in 0.5 V steps. In *Figure 16A* and *B*, the electrical resistance (R_e) obtained from fitting of the EIS assays of MAPB and CPB is given against the applied voltage. Both samples clearly show two different slopes below and above the materials' band-gap, E_g, related to the growth of EDLs and p- and n-type doped regions within the active layer, respectively.

In the range between 0 and 2.5 V, R_e decreases mono-exponentially for hybrid perovskite MAPI, while the redistribution of charges equilibrates at about 1.5 eV. The ionic conductance obtained at a frequency of 100 Hz mirrors the development of R_e

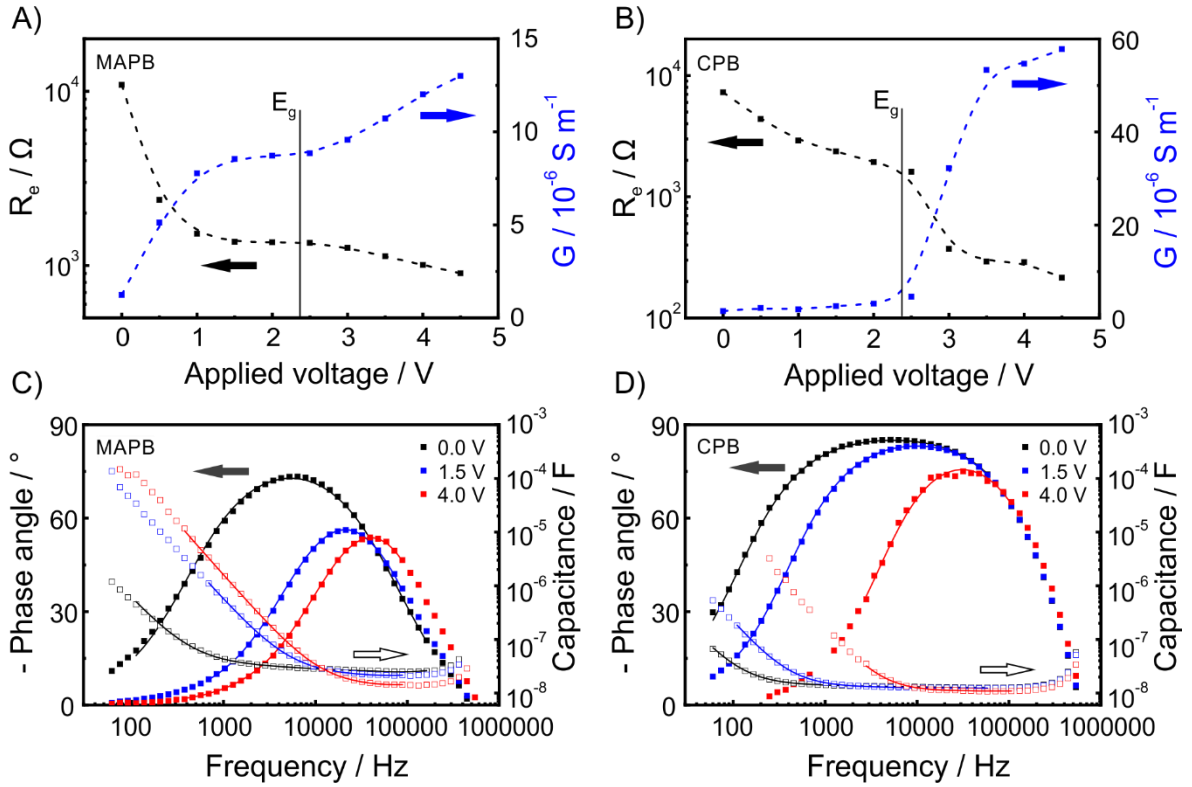

Figure 16. EIS assay driven at steady type mode. Resistance (black) and conductance (blue) as a function of applied voltage for MAPB NCs (A) and CPB NCs (B) with their respective band-gap marked by the vertical line. Phase angle (filled squared) and capacitance (empty squared) as a function of frequency for MAPB NCs (C) and CPB NCs (D) by applying a voltage of 0.0 (black), 1.5 (blue), and 4.0 V (red). Dashed lines in A) and B) are a guidance for the eye; solid lines in C) and D) represent the fittings according to the model of *Chapter 3.1*. Adapted from Puscher *et al.*[106].

and corroborates the correlation between ionic diffusion, formation of highly conductive regions, and, thus, a reduction of the resistance. A more detailed picture of the EDL formation is given by the capacitance and phase angle as a function of frequency in *Figure 16C*. As a result of the growing EDLs upon increasing the applied voltage, a rise of their capacitance is indicated at low frequencies. Also, the maximum of the phase angle lowers and shifts towards higher frequencies. This can be rationalized by the general behavior of double layers that have a high capacitance for low frequencies[172]. At high frequencies, though, these highly conductive layers near both electrodes contribute to the distance which the electronic charge carriers travel before reaching the sandwiched less conductive region of the film. Upon increasing the applied voltage beyond E_g, effective ohmic charge carrier injection initiates the

formation of p- and n-type doped regions as reflected in the linear reduction of the resistance.

In comparison, EIS assays of inorganic perovskite reveal a slower redistribution of charges upon increasing voltage (*Figure 16B*). R_e is lowered by some extent but does not equilibrate and the ionic conductance shows no crucial increase until E_g is reached. Furthermore, the capacitance and phase angle (*Figure 16D*) emphasize the finding that while EDLs are formed in CPB, their growth is much slower than for MAPB. In conclusion, this clearly highlights that Cs^+ rather abides within the crystal structure and does not contribute to the ionic motion. By exceeding the band-gap energy, the resistance drops drastically, which, in turn, increases the ionic conductivity. Firstly, this is a clear contrast to the hybrid perovskite, where the crossover between the slope of the resistance before and after E_g is continuous due to an efficient band-gap alignment. Secondly, here p- and n-type doped regions are forcefully formed, which most likely decomposes the material as was observed in the pulsed mode.

Finally, we observed the ion movement within MAPB in dynamic EIS assays. Here, a constant voltage of 3 V was applied for 12 h during which the impedance was periodically measured every 30 min (*Figure 17A*). The electrical characterization obtained from data fitting according to the full circuit is given as a function of time in *Figure 17B*. With decreasing ionic resistance (R_i) of the EDLs, R_e mono-exponentially drops within the first 4 h and converges to R_i. The time constant derived from the development of R_e is 1.3 ± 0.1 h, which is in perfect agreement with the results

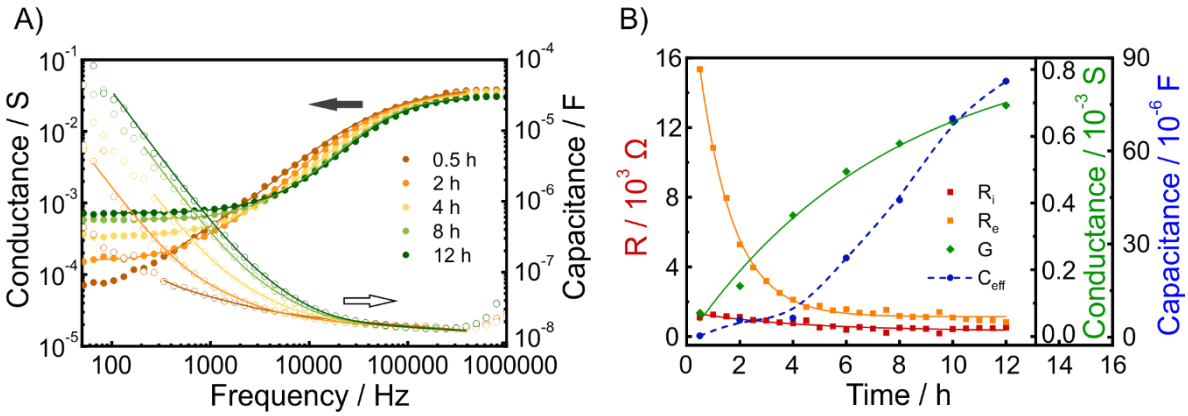

Figure 17. A) Conductance (filled circles) and capacitance (empty circles) as a function of frequency for MAPB NCs at 0.5, 2, 4, 8, and 12 h upon applying a constant voltage of 3.0 V. B) Electrical characterization as a function of time for MAPB. Dashed line in B) is a guidance for the eye; solid lines in A) and B) represent the fittings according to the model of *Chapter 3.1*. Adapted from Puscher *et al.*[106].

obtained from constant voltage and pulsed current measurements (*Table 1*). During the first 4 h, where R_e decreases, the effective capacitance (C_{eff}) rises slightly. After the convergence of the resistances, the doped regions grow towards each other narrowing the less conductive region and, in turn, C_{eff} increases drastically. Due to the diminishing of the undoped region, the ionic conductance approaches a limit at which the intrinsic zone cannot shrink any further. This is most likely the reason for the degradation of the perovskite presented in *Figure 15B*.

In summary, we have examined the ionic conductivity within perovskite by successfully applying the ionic drift concept of LECs as model system. We demonstrated the presence of two diffusing species within MAPB namely halides at short times and MA^+ at longer times. Upon applying a voltage, these form highly conductive EDLs at the electrodes and, when the voltage exceeds E_g, n- and p-type doped regions within the perovskite layer. Within inorganic perovskites such as CPB, it is only the halides that diffuse and upon forcefully displacing the Cs^+, the material rather decomposes.

4.2. Charge carrier transfer across interfaces within perovskite solar cells

In the following, the attention is focused on the charge carrier transfer mechanism studied by fs-TAS. Initially, we investigated charge carrier dynamics in polymer-based ternary solar cells containing perovskite NCs. Then, we turned towards electron injection from perovskite into PCBM layers of amorphous and polycrystalline morphologies. Finally, we address the controversial topic of hole injection from perovskite into varying hole transporting materials.

4.2.1. Improved charge carrier dynamics in polymer/perovskite nanocrystal-based hybrid ternary solar cells

R. Soltani‡, B. M. D. Puscher‡, A. A. Katbab, I. Levchuk, N. Kazerouni, N. Gasparini, N. Camaioni, A. Osvet, M. Batentschuk, R. H. Fink, D. M. Guldi, T. Ameri, *Physical Chemistry Chemical Physics*, 2018, **20**, 23674-23683. // ‡ contributed equally.

In many single-junction polymer solar cells the photoactive layer is a blend of a fullerene derivative acting as electron acceptor and a conjugated polymer as electron donor material[35,233]. The spectral range of these polymers is easily tunable but limited, thus incorporating a second photon absorber, such as narrow band-gap polymers[234,235], dyes[236], small molecules[237] or quantum dots[238], with a complementary absorption range to the first photon absorber improves photon harvesting. A center of attention are derivatives of diketo pyrrolo-pyrrole that are soluble, narrow band-gap polymer with an ambipolar nature and high charge carrier mobilities as demonstrated by Bronstein *et al.*[239]. Furthermore, when combined with fullerene derivatives, the components form a high-energy charge separated state[240]. Bujleveld *et al.* achieved a PCE of up to 4.6% for single-junction binary blends of diketo pyrrolo-pyrrole and PCBM[241], which is comparable to P3HT:PCBM blends with 5%[235]. A huge draw-back of polymer solar cells is, however, inefficient dissociation of bound Frenkel excitons within polymer grains and across the interface. This slows charge carrier separation drastically and promotes charge carrier recombination. Gasparini *et al.* demonstrated that a ternary blend containing a highly ordered sensitizer suppresses these recombination processes[234].

In this work, we presented the beneficial contribution of perovskite in the form of FAPI NCs as a second photon absorber in the bulk heterojunction active layer of a polymer solar cell. The active layer is composed of the electron donor pDPP5T-2 (DPP), a

derivative of diketo pyrrolo-pyrrole, and the electron acceptor PCBM (structural formulae are given in *Figure 9)*. Nanocrystals and specimens used for this study were prepared in the group of Prof. Brabec[242] and Dr. Ameri[129]. The FAPI NCs, that have an edge length of 14.4 ± 3.4 nm, are surrounded by the capping agents oleylamine and oleic acid. Most likely the NCs are located between the polymer and fullerene domains as it is known from other ternary blends[236] and should mediate charge carrier separation between the donor and acceptor. Firstly, FAPI NCs allow for fast generation of free charge carriers from Wannier excitons and, secondly, exhibit a cascading charge carrier transport (*Figure 18A*). In order to elucidate the charge carrier transfer mechanism in these DPP:FAPI NCs:PCBM ternary blends, we performed fs-TAS on binary blends of DPP:PCBM (1:2 percent by weight, wt%) and DPP:FAPI NCs (1:1 wt%) as well as DPP:PCBM ternary blends containing 5 and 10 wt% of FAPI NCs and a DPP reference.

The solar cell devices that have an inverted architecture of ITO/$Ba(OH)_2$/active layer/MoO_x/Ag (*Figure 18B*) were prepared and characterized by Dr. Rezvan Soltani[129]. In relation, our specimen were directly deposited on glass using the fabrication of their respective devices, yet without any hole or electron transporting layer. The samples were measured at room temperature in a home build nitrogen-

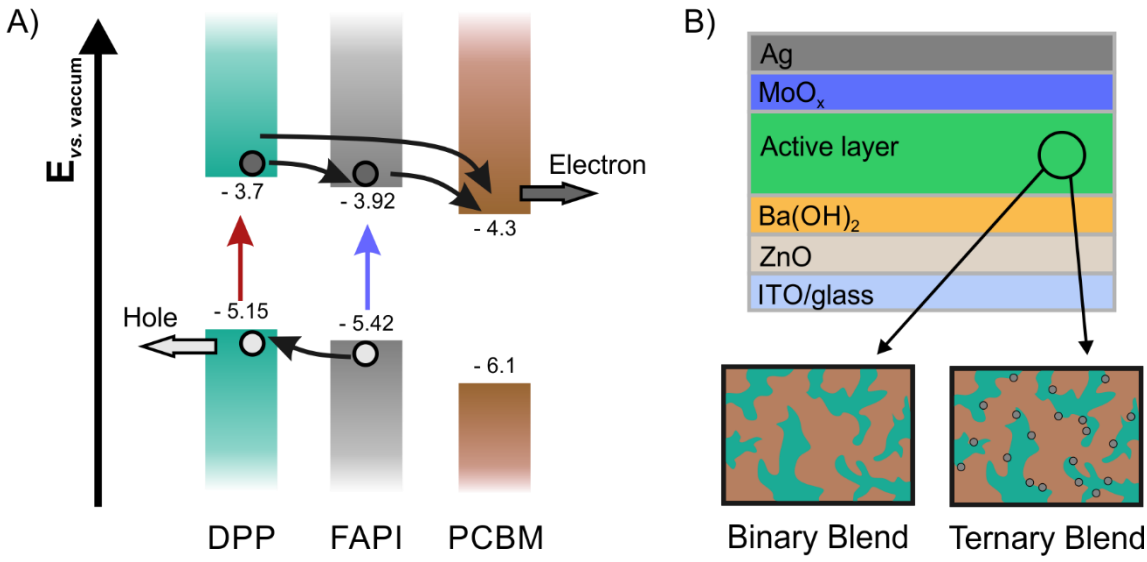

Figure 18. A) Energy level diagram of components within the active layer with DPP (turquoise), FAPI NCs (grey), and PCBM (brown). B) Corresponding schematic depictions of the architecture used for solar cells (top) studied as well as the blending within DPP:PCBM binary (left bottom) and ternary blend (right bottom) with FAPI NCs (grey) at the DPP-PCBM interface. Adapted with permission from Soltani, Puscher *et al.*[129].

purged atmosphere chamber. An λ_{exc} of 775 nm with a laser fluence of 104 µJ cm^{-2} was used to selectively excite DPP in order to observe the charge injection from the polymer into FAPI NCs and PCBM.

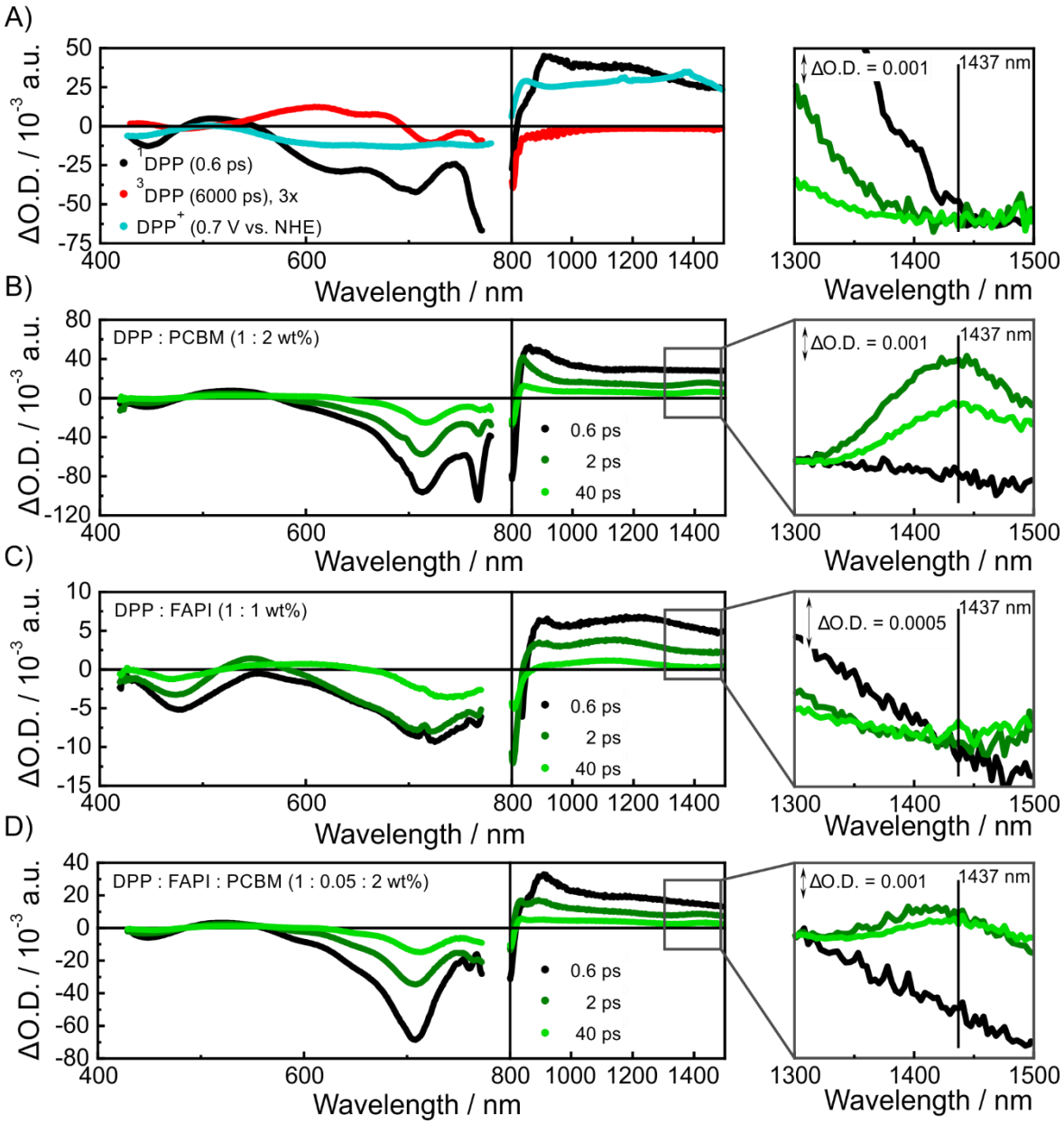

Figure 19. Differential absorption spectra (A, left) taken at time-delays of 0.6 and 6000 ps after excitation with 775 nm representing singlet (black) and triplet (3x enhanced, red) excited DPP, as well as differential absorption spectrum upon spectroelectrochemical oxidation of DPP at 0.7 eV *vs.* normal hydrogen electrode (turquoise). Detailed, stacked differential absorption spectra (A, right) of the DPP cation signal region. Differential absorption spectra (left) of DPP:PCBM (1:2 wt%, B) and DPP:FAPI (1:1 wt%, C) binary blend as well as DPP:FAPI:PCBM (1:0.05:2 wt%, D) ternary blend upon excitation with 775 nm; corresponding detailed, stacked differential absorption spectra of DPP's cation signal (right). Delay times of 0.6 (black), 2 (dark green), and 40 ps (light green) were used. Adapted with permission from Soltani, Puscher *et al.*[129].

First, we investigated the excited states and recombination processes within the DPP reference. The differential absorption spectrum of the DPP singlet excited state after 0.6 ps (*Figure 19A*, black) displays GSBs at 448, 634, and 703 nm as well as PIA at 520 nm and above 800 nm extending into the NIR range. The PIA in the NIR overlaps with the SE centered around 840 nm. An additional pathway that depopulates the singlet excited state is intersystem crossing towards the triplet excited state, discernable by its PIA signal located between 620 and 695 nm at 6000 ps (*Figure 19A*, red, 3x enhanced signal).

We then turned towards the binary blends to investigate the charge separation process between DPP and PCBM (*Figure 19B*) as well as DPP and FAPI NCs (*Figure 19C*). Derived from spectroelectrochemical results (*Figure 19A*, turquoise), the DPP's cation signal is located at 850 and 1437 nm, with the latter being emphasized in the detailed and stacked curves on the right in *Figure 19B* and *C*.

In the differential absorption spectra of the DPP:PCBM sample (*Figure 19B*), the signals related to the DPP cation at 1437 nm develop after 2 ps, confirming charge carrier separation at the DPP-PCBM interface. The intensity of the DPP cation signal at 1437 nm is, however, already strongly reduced after 40 ps, which suggests fast recombination of the holes in the DPP and electrons in the PCBM. Apart from non-geminate recombination towards the polymer's and fullerene's ground-state, electrons within the PCBM are, additionally, transferred from the charge separated state into the energetically lower triplet excited state of DPP.

In the differential absorption spectra of DPP:FAPI NCs (*Figure 19C*), the GSB features and the pronounced NIR PIA signal of the polymer have the same red-shift to 480, 650, and 720 nm as recorded in absorption measurements by Soltani, Puscher *et al.*[129]. Most probably, this is a direct result of the FAPI NCs on the polymer's ordering towards well-structured domains[243]. After a delay time of 40 ps, the GSB is further red-shifted compared to the signal obtained for a delay time of 2 ps. This stems from the contribution of excited perovskite, which is observable only after charge injection from the polymer due to the selective excitation of DPP. Charge separation at the DPP-FAPI NCs interface is corroborated by a weak DPP cation signal in the NIR. The additional transient species by the FAPI NCs is populated within the first 10 ps, as was studied in time absorption profiles of the GSB recorded at 681 and 756 nm by Soltani, Puscher *et al.*[129]. Interestingly, the features of DPP's triplet excited state are

weak in DPP:FAPI NCs binary blends, leading to the conclusion that recombination between DPP and FAPI NCs is preferred over re-injection from the perovskite into the triplet excited state of DPP.

Finally, we compared the insight gained from the binary blends to the fs-TAS results of the ternary blends (*Figure 19D*). While the DPP:FAPI NCs:PCBM sample has the same differential absorption features as the DPP:PCBM blend, it differs in its kinetics. For instance, we derive from the DPP cation signal that FAPI NCs facilitate the formation of and, furthermore, extend the lifetime of the charge separated state. To further evaluate the lifetimes of the species (*Table 2*) within both binary and ternary blends, we performed target analysis using Glotaran and the models presented in *Figure 20A*. The calculated species associated spectra and the states population over time are presented in *Figure 20B* and *C*. The lifetime of DPP's singlet excited state (τ_1) is with 0.6 ± 0.01 ps for the 5 wt% ternary blend much shorter than was observed in the binary blend with 1.4 ± 0.04 ps. This faster depopulation is caused by dual charge injection pathways towards the charge transfer state $DPP^{\delta+}$:$PCBM^{\delta-}$ and charge separated state DPP^{+}:$FAPI^{-}$.

Table 2. Lifetimes of the species determined from target analysis using the model given in *Figure 20*A.

FAPI NCs content [wt%]	τ_1 [ps] ^{1}DPP:PCBM	τ_2 [ps] $DPP^{\delta+}$:$PCBM^{\delta-}$	τ_3 [ps] DPP^{+}:$FAPI^{-}$	τ_4 [ps] DPP^{+}:$PCBM^{-}$
0	1.4 ± 0.04	31 ± 0.2	-	536 ± 4
5	0.6 ± 0.01	43 ± 0.3	4.1 ± 0.03	607 ± 5
10	0.5 ± 0.01	48 ± 0.3	4.6 ± 0.04	572 ± 5

The lifetime of the bound charge carriers increases by 39% and 55% for ternary blends with 5 and 10 wt% FAPI NCs, respectively, compared to the binary blend. The lifetime τ_3 of the intermediate charge separated state DPP^{+}:$FAPI^{-}$ reaches a mean value of 4.4 ± 0.04 ps for the ternary blends. Finally, the charge separated state DPP^{+}:$PCBM^{-}$ is populated by the diffusion of the bound charge carriers of $DPP^{\delta+}$:$PCBM^{\delta-}$ into the respective grains and the injection of electrons within FAPI NCs into the PCBM domain. The lifetime τ_4 of DPP^{+}:$PCBM^{-}$ is with 607 ± 5 ps the longest in 5 wt% ternary blends, which means that the FAPI NCs inhibit recombination and injection into DPP's triplet excited state. This can be rationalized by a smaller DPP-PCBM interface owing to FAPI

NCs being located between the polymer and fullerene domains. When increasing the FAPI NCs content to 10 wt%, τ_4 is reduced compared to 5 wt% but still longer than for the binary blend. These findings are corroborated by the power conversion efficiency of the respective solar cells that increase from 5.0 ± 0.4% for binary to 5.5 ± 0.3% for ternary blends with 5 wt% of NCs.

In summary, this study elucidated the effect of FAPI NCs on the charge carrier mechanism and the transients' lifetime in DPP:FAPI NCs:PCBM ternary blends. FAPI NCs provide an additional pathway to rapidly depopulate the singlet excited state of

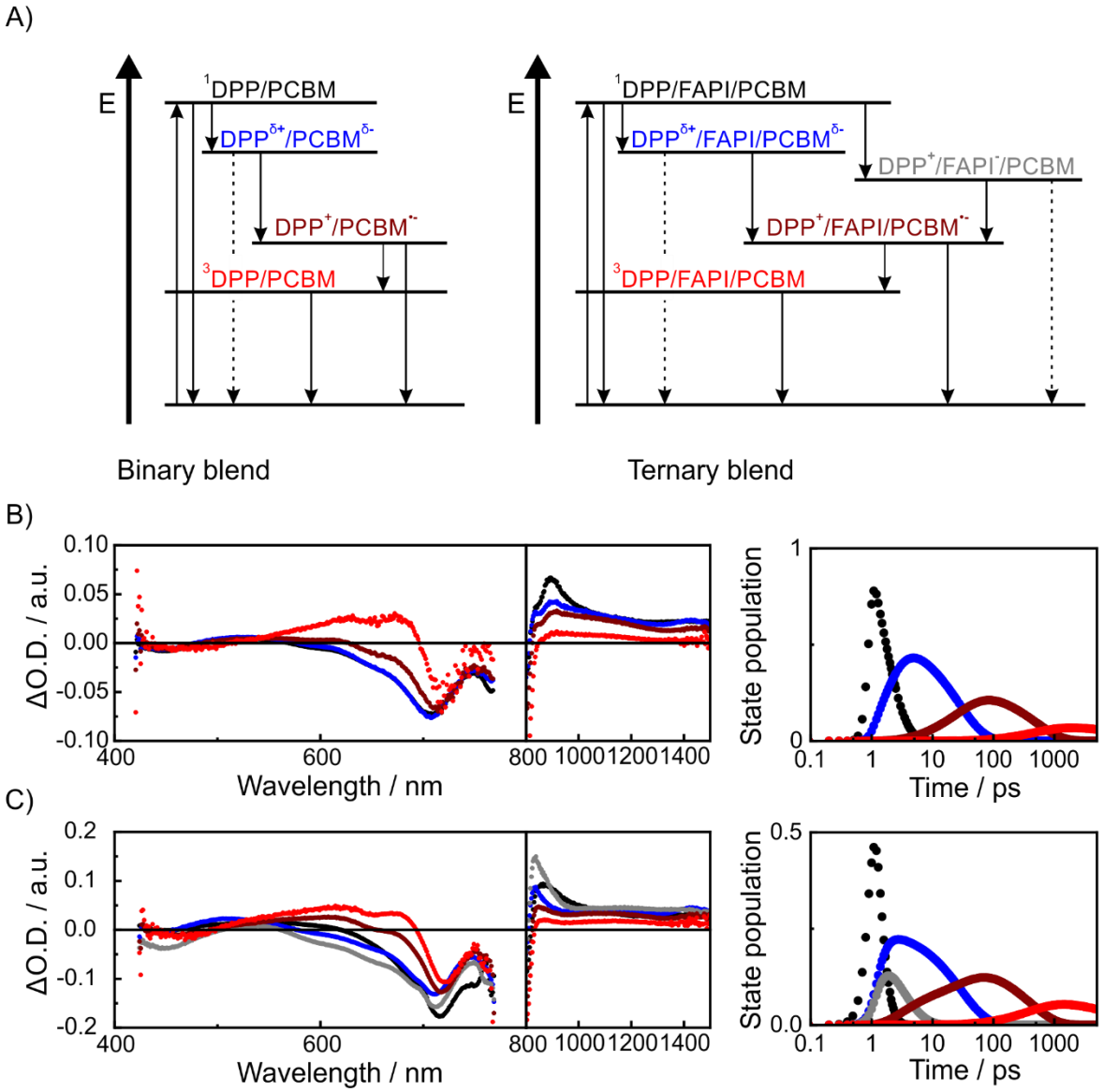

Figure 20. A) Models used for target analysis of binary (left) and ternary blends (right). Species associated spectra (left) and state population (right) of binary (B) and ternary (C) blends showing singlet excited DPP (black), bound charge carriers located at the interface of either DPP:PCBM (blue) or DPP:FAPI (grey), separated charge carriers in DPP and PCBM (dark red), as well as triplet excited DPP (red). Adapted with permission from Soltani, Puscher *et al.*[129].

DPP and accelerate free charge carrier generation. This leads to fast charge carrier separation across DPP and PCBM. Furthermore, the recombination of the separated charge carriers within the polymer and the fullerene is slowed and re-injection into DPP's triplet excited state is reduced by a smaller DPP-PCBM interface. The results were corroborated by the figure-of-merits and characterization of complete solar cells performed by Dr. Rezvan Soltani[129], resulting in champion devices with a PCE of 5.5% using 5 wt% of FAPI NCs.

4.2.2. Assembling mesoscale-structured organic interfaces in perovskite photovoltaics

Y. Hou, C. Xie, V. V. Radmilovic, B. M. D. Puscher, M. Wu, T. Heumüller, A. Karl, N. Li, X. Tang, W. Meng, S. Chen, A. Osvet, D. M. Guldi, E. Spiecker, V. R. Radmilović, C. J. Brabec, *Advanced Materials*, 2019, **31**, 1806516.

In the previous chapter, we have demonstrated the beneficial role of perovskite NCs within a polymer solar cell due to its improved charge carrier transfer properties. We now turn towards PSCs and study the extraction of electrons from the perovskite material.

In planar PSCs, one of the most prominent organic ETMs is the fullerene derivative PCBM (structural formula is given in *Figure 9* in *Chapter 2.2.1*). In contrast to fullerenes, PCBM films are solution-processable at low temperature, e.g. from chlorobenzene, while still showing good electron accepting and hole blocking properties. In 2013, Docampo *et al.* successfully implemented PCBM in low-temperature fabricated, flexible PSCs with inverted, thus p-type, architecture as alternative to mesoporous TiO_2 that needs to be annealed to 500 °C[201]. Additionally, Shao *et al.* and Hou *et al*. demonstrated that planar PSCs with PCBM and other fullerene derivatives covering compact TiO_2 feature reduced J-V hysteresis compared to bare TiO_2-based devices, due to its passivating effect on perovskite's grain boundaries and surface[157,180]. When introduced in a n-type structure with PCBM as bottom layer ($PCBM_{compact}$), the PCBM has, however, a low wettability towards the perovskite's precursor and suffers from molecule diffusion into the perovskite film[244]. Consequently, homogenous thin-film formation, which is important for reduced trap states and reproducible power conversion efficiencies with minimal deviations, is challenging. Furthermore, solution-processed disordered PCBM films feature a broad distribution of its density of states that, similar to mesoporous TiO_2, extends into the band-gap (*Chapter 2.2.1*). Shao *et al.* demonstrated that solvent annealing improves the crystallinity and, in turn, enhances the V_{OC} by 9% and the PCE by 13% of a planar PSC prepared by solvent annealing in comparison to PSCs prepared by temperature annealing[197]. For better stability and improved charge carrier extraction, fullerene derivatives that have good TiO_2-covering and self-assembling properties were tailored by Hou *et al.* and Tao *et al.*[180,245], but are less straight-forward in fabrication.

In this work, Dr. Yi Hou presented a straight-forward and environmentally friendly preparation of highly crystalline PCBM nanoparticles (NPs, $PCBM_{NPs}$) from water *via* nanoemulsion technique. From scanning electron microscopy and high-resolution transmission electron microscopy, it was seen that these $PCBM_{NPs}$ are spherical and have a diameter of 40 ± 11 nm. When deposited on a substrate like tin dioxide, PCBM NPs reorganize themselves to form an ordered mesoporous structure with a large pore volume, of which the latter is tuned to a desired size by temperature annealing. Accordingly, the surface geometry is altered in favor of an increased interface area. The precursor solution of perovskite fills these voids without leaching PCBM and has, furthermore, an improved wettability compared to compact PCBM films. The perovskite layer thus obtained has an improved homogeneity and crystallinity, resulting in PSCs with an overall reproducible efficiency and better thermal stability compared to perovskite on top of compact PCBM.

As the PCBM-perovskite interface plays an important role, we studied the electron injection from lead iodide rich perovskite ($FA_{0.83}MA_{0.17}Pb_{1.1}Br_{0.22}I_{2.98}$) into the ETMs by fs-TAS on perovskite/$PCBM_{compact}$ (orange), perovskite/$PCBM_{NPs}$ (turquoise), and perovskite reference (black) films on top of a glass substrate (see *Figure 21A*). An λ_{exc} of 695 nm was chosen to nearly resonantly excite the perovskite across the band-gap and solely populate perovskite's VB_1. The differential absorption spectra of all three samples with a 0.7 ps time-delay are presented in *Figure 21B*; the characteristic features of photoexcited perovskite are identifiable as described in detail in *Chapter 3.2*. In short, the GSB at 760 nm represents the transition $VB_1 \rightarrow CB_1$ with an asymmetric extension towards shorter wavelengths due to hot carrier distribution. PIA signals emerge between 500 and 650 nm as well as in the NIR with a maximum at 930 nm.

The onset of the asymmetric extension towards the PIA for perovskite/$PCBM_{NPs}$ compared to the perovskite reference is red-shifted from 656 to 686 nm, which is in strong contrast to the marginal shift for perovskite/$PCBM_{compact}$. Furthermore, derived from exponentially fitting time-absorption profiles of *Figure 21C*, the rate constants for the hot-carrier cooling process increased from $(18.1 \pm 0.3) \times 10^{10}$ s^{-1} for perovskite to $(18.8 \pm 0.3) \times 10^{10}$ s^{-1} for perovskite/$PCBM_{compact}$, and to $(20.4 \pm 0.4) \times 10^{10}$ s^{-1} for perovskite/$PCBM_{NPs}$. Consequently, it is evident that the hot carrier density within photoexcited perovskite is harvested due to ultrafast electron injection from perovskite

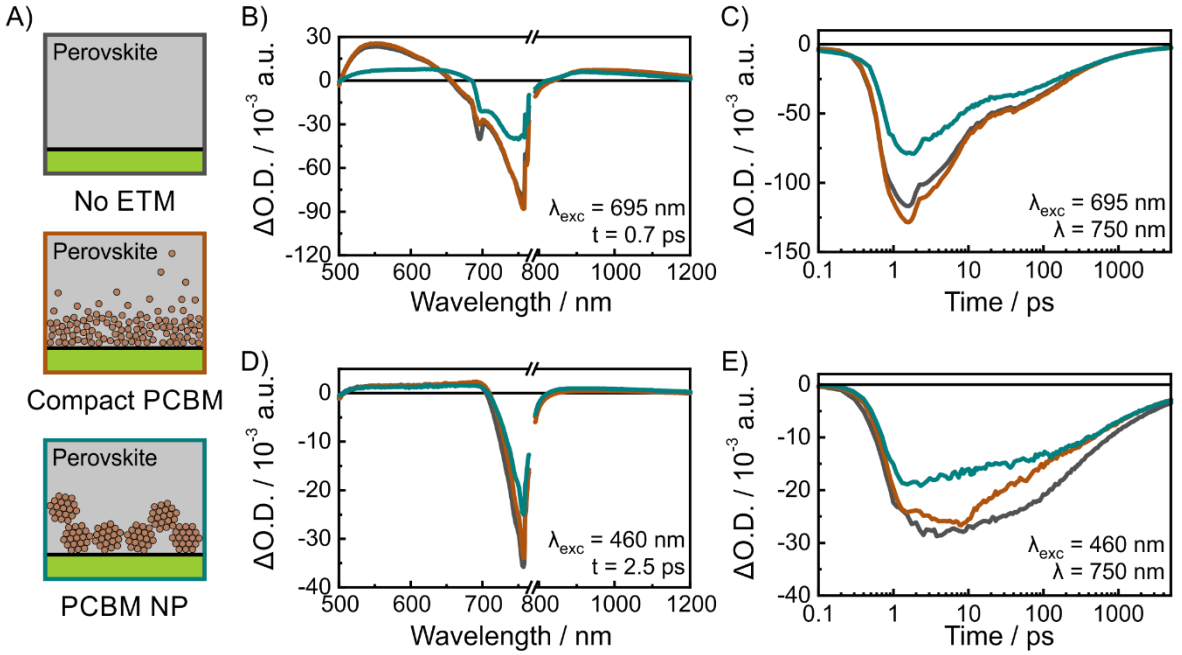

Figure 21. A) Schematic depiction of perovskite (top, black), perovskite/$PCBM_{compact}$ (middle, brown) with molecule diffusion, and perovskite/$PCBM_{NPs}$ (bottom, turquoise) films. Differential absorption spectra taken at a time-delay of 0.7 ps after excitation with 695 (B) and 460 nm (D) of perovskite (black), perovskite/$PCBM_{compact}$ (brown), and perovskite/$PCBM_{NPs}$ (turquoise) films. Time absorption profiles at 750 nm after excitation with 695 (C) and 460 nm (E) of the same samples. Adapted with permission from Hou *et al.*[179].

into the highly crystalline PCBM NP film. This can be rationalized by two enhanced properties of PCBM NPs, namely the augmented interface area and the improved crystallinity. Materials with many grain boundaries and lattice dislocations, such as compact PCBM, introduce disperse, perturbed, and localized energy states that, additionally, extend into the band-gap. Crystalline solids, however, have well-defined energy levels within their band structure, by which high-energy states of PCBM NPs activate a “hot” channel[246] to harvest perovskite’s hot electrons.

To further investigate the ultrafast charge separation process at the interface of perovskite and both PCBM films, the samples were excited at 460 nm (*Figure 21D* and *E*). Signifying the cooling process of hot carriers within the perovskite reference, the kinetic profile of its GSB at 750 nm growths within the initial 4 ps after photoexcitation. This is not observed for the perovskite/$PCBM_{NPs}$ sample, which accounts for the efficient harvest of hot carriers by crystalline PCBM NPs. Very intriguing is the 8 ps delayed GSB signal when using compact PCBM. The process, which underlies this finding, is a back-transfer of electrons within high-energy states of $PCBM_{compact}$ into perovskite’s VB.

In summary, our fs-TAS results reveal the improved interaction between perovskite and the PCBM NPs film referenced to the standard compact PCBM. The augmented interface of the self-assembled highly crystalline mesoscale-structured PCBM layer improves the permeation by the perovskite precursor and, in turn, scavenges electrons efficiently. Furthermore, the distinct density of states within polycrystalline PCBM NPs enables harvesting of hot electrons before thermal relaxation. In contrast to PCBM NPs, already collected electrons within compact PCBM are lost by fast back-injection into the perovskite's CB. Consequently, Dr. Yi Hou observed that the exceptional electron extraction provided by the mesoscale-structured PCBM combined with improved perovskite film formation conditions by the same, enables solar cells (0.1 cm^2) with reproducible PCE of 19.0 ± 1.8%; in comparison compact PCBM achieved 18.1 ± 2.9%. Furthermore, when increasing the active area to 1 cm^2, the PCE of compact PCBM decreased to 16.2%, while the PCE stayed nearly constant at 18.5% with PCBM NPs.

4.2.3. Hot electron injection into semiconducting polymers in polymer based-perovskite solar cells and their fate

J. Jiménez-López‡, B. M. D. Puscher‡, W. Cambarau, R. H. Fink, E. Palomares, D. M. Guldi, *Nanoscale*, 2019, **11**, 23357-23365. // ‡ contributed equally.

Finally, we investigated the charge carrier transfer across the perovskite/HTM interface for organic semiconductors used in an n-type sDSSC architecture. The injection rate for hole transfer from perovskite into HTMs of both small molecule and polymer-based type is heavily debated: time constants for spiro-OMeTAD range between 660[136] and 0.7 ps[203] according to Xing *et al.* and Piatkowski *et al.*, respectively. Later, Brauer *et al.* even reported on hot hole injection within a sub-80 fs time scale[204]. In the case of polymer-based semiconductors as HTMs, another study by Brauer *et al.* states that hole injection requires several ns for P3HT, PCPDTBT, and PTAA[205]. In contrast, Ishioka *et al.* observed hole injection to occur within 1 and 2 ps for PTAA and PEDOT:PSS, respectively[247]. Thereby, in the first part of this work we corroborated the fast hole injection of about 1-2 ps from perovskite into both spiro-OMeTAD as well as commercially available low band-gap semiconducting polymers such as P3HT, PTB7, and PCPDTBT. Interestingly, compared to PTB7 and P3HT, PCPDTBT shows a clear underperformance as HTM for PSCs, although both the injection rate[248] as well as the hole mobility[189] are comparable. Li *et al.* demonstrated that it is feasible to inject hot electrons into an energetically higher LUMO level compared to the CB of perovskite[249]. Thus, in the second part of this work, we investigated another loss pathway arising from hot electrons within non-thermalized perovskite that can be injected into an HTM with an energetically low LUMO level, such as PCPDTBT. As a reference for efficient electron and hole extraction from the perovskite, we used state-of-the-art mesoporous TiO_2 and spiro-OMeTAD, respectively. The energy levels and structural formulae of the organic semiconductors are given in *Figure 9*.

The samples, bilayers of MAPI/TiO_2 and MAPI/HTM as well as a MAPI reference, were prepared by Dr. Jesús Jiménez-López and Werther Cambarau. They were sealed with poly(methyl methacrylate) (PMMA) and measured at room temperature. An λ_{exc} of 460 nm with laser fluences ranging from 2.6 to 191 µJ cm^{-2} was used to selectively excite MAPI with enough excess energy for the creation of hot electrons. The differential absorption spectra obtained from the MAPI reference (*Figure 22*, black) display the characteristic features of perovskite as described in detailed in *Chapter 3.2*.

GSBs at 760 and 460 nm represent the transitions $VB_1 \rightarrow CB_1$ as well as $VB_2 \rightarrow CB_1$ or alternatively $VB_1 \rightarrow CB_1$ at another high symmetry point in the Brillouin Zone[95], respectively. PIA signals emerge between 500 and 650 nm as well as a short-lived one in the NIR starting from 790 nm. Hot carriers are distributed in the CB_1 causing an asymmetric extension of the 760 nm GSB towards shorter wavelengths. Increasing the excess energy of charge carriers, intra subband absorption of electrons assisted by LO phonon emission causes an ultrashort-lived PIA signal at 780 nm[217,220].

For MAPI/HTM samples, the spectral characteristics of the HTMs' polarons are visible after 1.2 ps in the NIR (*Figure 22A*) with main peaks being located at 905 and 965 nm for PCPDTBT and spiro-OMeTAD, respectively. To evaluate the injection kinetics, the time absorption profiles at these polaron features were correlated to the traces in MAPI in the absence of any HTM. The resulting charge injection rate for PCPDTBT with $(1.00 \pm 0.05) \times 10^{12}$ s^{-1} is similar to the one of spiro-OMeTAD with $(0.82 \pm 0.03) \times 10^{12}$ s^{-1}. This coincides with a resembling "apparent driving force" for the hole transfer process in both materials compared to other polymer HTMs[189] and renders the injection rate a non-determining factor for efficient solar cells.

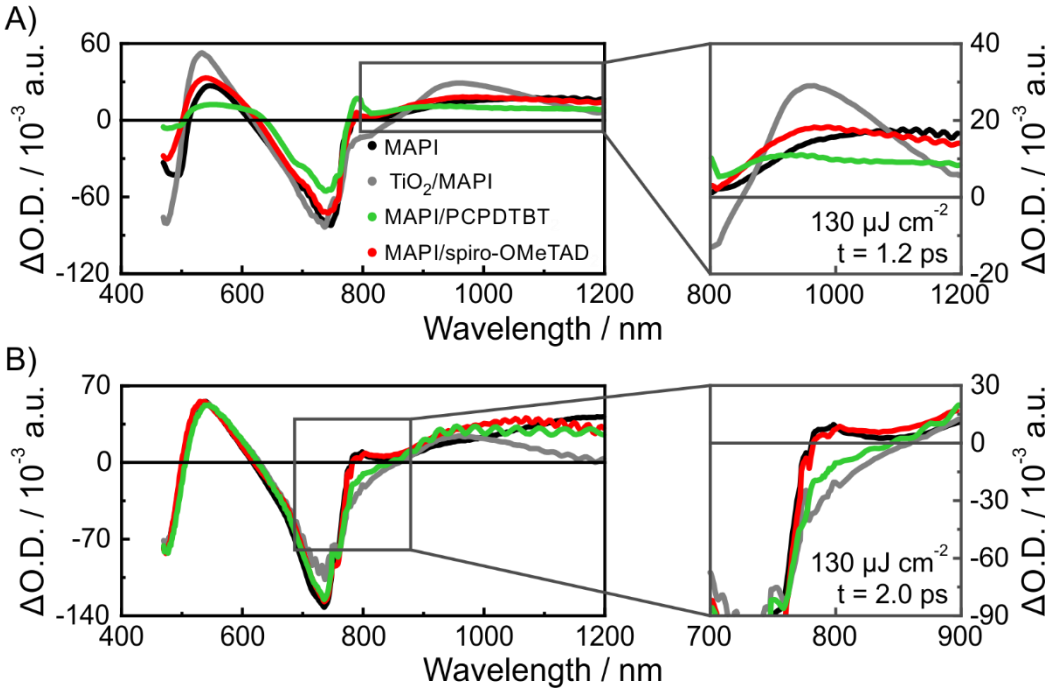

Figure 22. Differential absorption spectra of MAPI (black), TiO_2/MAPI (grey), MAPI/PCPDTBT (green), and MAPI/spiro-OMeTAD (red) with a delay time of 1.2 (A) and 2 ps (B) after excitation with 460 nm and a laser fluence of 130 μJ cm^{-2}. Adapted with permission from Jiménez-López, Puscher *et al.*[248].

The weakening of the 780 nm PIA in the presence of PCPDTBT is striking compared to spiro-OMeTAD (*Figure 22B* and *Figure 24A*). This behavior resembles the spectral progress in the TiO_2/MAPI sample, where it is attributed to hot electron injection from the perovskite into an ETL. To investigate whether PCPDTBT quenches hot electrons across the MAPI/HTM interface, we performed laser intensity dependent measurements (*Figure 23*). The intensity of the hot carrier PIA for MAPI indicates saturation towards high laser fluences related to Pauli blocking effects[250]. In the presence of ETM and HTMs, the intensity of the PIA increases linearly for laser fluences below 26 µJ cm^{-2}. The PIA of the MAPI/spiro-OMeTAD sample saturates upon increasing the laser fluence towards 191 µJ cm^{-2} similarly to the MAPI reference. This is in contrast to the linear dependence in MAPI/TiO_2, where electrons are injected into the ETM and a reduced charrier-phonon interaction shifts the saturation towards laser fluences exceeding 191 µJ cm^{-2}. Intriguingly, MAPI/PCPDTBT also follows a continuously linear increase similar to MAPI/TiO_2, which, furthermore, corroborates our hypothesis that not only holes but also hot electrons are extracted by PCPDTBT due to its energetically low LUMO level. In comparison, spiro-OMeTAD, which has a high LUMO level, acts not only as hole transporting but also electron blocking layer.

In the presence of dual charge carrier injection, two possible features should be observable. Firstly, injected holes and electrons within the PCPDTBT can radiatively recombine, which would be visible as fluorescence. On the basis of the absence of any noticeable emission by the polymer, we consider this not to be a plausible scenario. Secondly, as a result the electrons can be back-transferred from PCPDTBT's LUMO

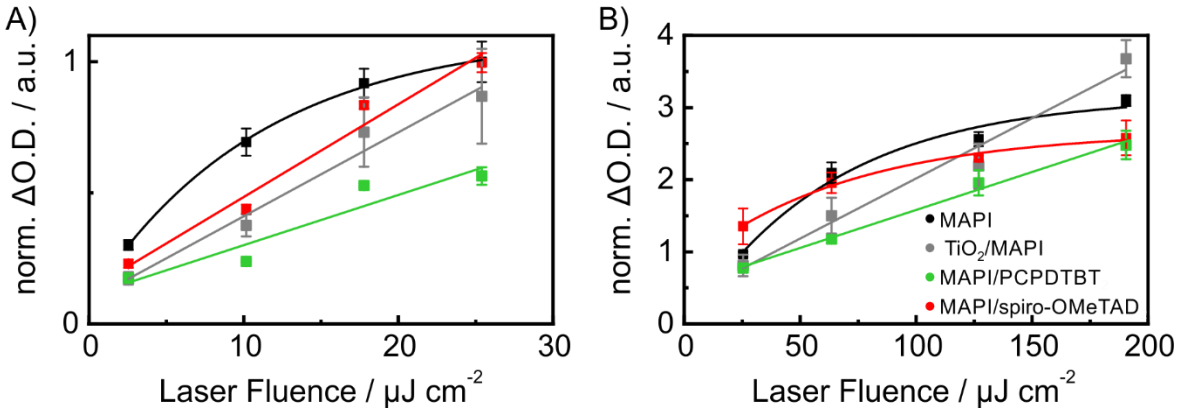

Figure 23. The dependence of the PIA at 785 nm on the laser fluence going from 2.6 to 26 µJ cm^{-2} (A) and 26 to 191 µJ cm^{-2} (B) for MAPI (black), MAPI/TiO_2 (grey), MAPI/spiro-OMeTAD (red), and MAPI/PCPDTBT (green). The intensity was normalized in reference to 26 µJ cm^{-2}. Adapted with permission from Jiménez-López, Puscher *et al.*[248].

into the lower CB minimum in MAPI, which would, in turn, delay the GSB maximum of MAPI as was seen for the compact PCBM (*Figure 21E*)[179]. The time absorption profiles at 750 nm for MAPI, MAPI/TiO_2, and MAPI/spiro-OMeTAD peak at approximately 4 ps as given in *Figure 24B*, yet for MAPI/PCPDTBT it is clearly delayed to 9 ps. This can also be observed upon reducing the laser fluence, where the GSB maximum peaks at 6 to 8 ps in the presence of spiro-OMeTAD or TiO_2 but is delayed to approximately 25 ps for MAPI/PCPDTBT (*Figure 24C*).

Finally, we turned towards the PIA in the NIR and analyzed the time absorption profiles at 1040 nm (*Figure 24D*). Here, the spectral features of the transferred charge carriers within the ETM and HTM are best discernable at intensities of 26 µJ cm^{-2}. The kinetics of the MAPI/TiO_2 and MAPI/spiro-OMeTAD show divergent recombinations compared to one another as well as to the short-lived MAPI reference. The time absorption profile of MAPI/PCPDTBT differ most from the others, though. On early delay times (< 3 ps), we observed a reduced intensity in the PIA to MAPI that we relate to electron extraction by the polymer. Subsequently, the intensity of the PIA signal increases simultaneously

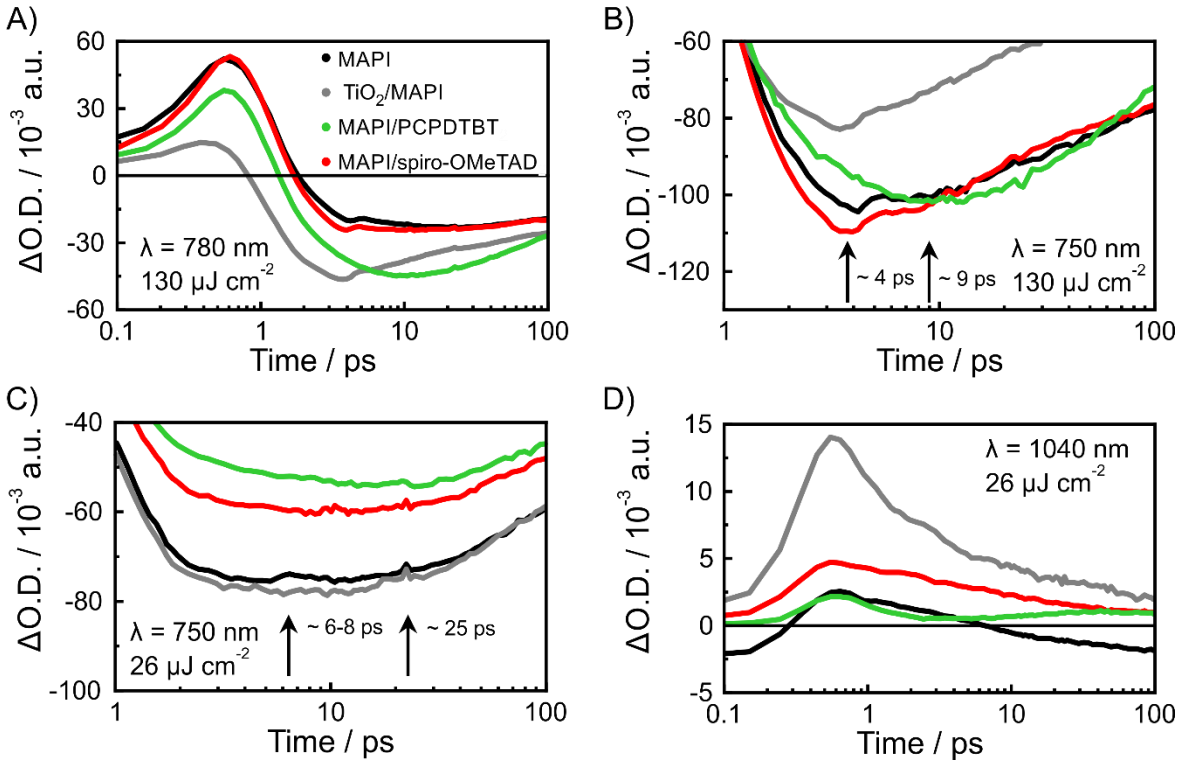

Figure 24. Time absorption profiles of MAPI (black), TiO_2/MAPI (grey), MAPI/PCPDTBT (green), and MAPI/spiro-OMeTAD (red) at a probing wavelength of 780 (A), 750 (B, C), and 1040 nm (D) after excitation with 460 nm and a laser fluence of 130 (A, B) and 26 µJ cm^{-2} (C, D). Adapted with permission from Jiménez-López, Puscher *et al.* [248].

with the back-injection of electrons into the MAPI CB. We attribute the PIA at longer time-delays to the spectral signature of the PCPDTBT polaron. The fluctuation of features in the NIR is not present in the time absorption profiles of any other sample. These findings are detrimental in a full device, as hot electrons are affected in their extraction by a sub-picosecond competition between the favorable TiO_2 and the polymer. As a consequence of their subsequent back-transfer, the luminescence of MAPI in the presence of PCPDTBT is the highest in relation to the other HTMs. Finally, this loss process lowers the photocurrent by 40% and 30% of solar cells featuring PCPDTBT in relation to spiro-OMeTAD and PTB7, respectively. We assign it tentatively to be the reason behind the weak performance of solar cells using PCPDTBT as HTM.

In summary, we have shown the HTM-type independent fast injection of holes from perovskite into small molecule type or polymer-based HTMs. Furthermore, we have elucidated a loss pathway for hot electrons that are generated close to the perovskite/HTM interface. Instead of being efficiently transported and injected into an ETM, the electrons are transferred into a deadlock within the energetically low LUMO state of the HTM and can only relax back into the perovskite CB. We have, thus, shown that hot carriers cannot only contribute to the solar cell efficiency, but also cause reduced performance if materials with a low LUMO are selected as HTMs.

5. Summary

In conclusion, the work at hand provides a deep understanding of ionic diffusion processes within lead-based halide perovskite materials as well as their interaction with electron and hole transporting materials by means of injection and recombination processes. Perovskite's exceptional properties, e.g. fast generation of free charge carriers and relatively long-lived hot electrons, enable additional pathways for charge carrier transfer. The studies were performed using electrochemical methods, i.e. voltammetry, amperometry, and impedance spectroscopy, as well as fs-TAS.

In the first part, we focused on the intrinsic properties of perovskite in respect to its ionic conductivity. We demonstrated that hybrid perovskites such as $MAPbBr_3$ (prepared in the workgroup of Dr. Docampo) feature two diffusing species under an applied voltage in contrast to inorganic perovskites such as $CsPbBr_3$. For both perovskite materials, the components with short diffusion times are halides and their vacancies which provide low diffusion activation energy. With a longer diffusion time, the organic **A** cations, MA^+, realign with the electric field and it as well as its vacancies contribute to the ionic motion within the material. In contrast, the **A** cation in $CsPbBr_3$ has a less fluid character than $MAPbBr_3$ and, in turn, Cs^+ remains within the crystal structure. $CsPbBr_3$ decomposes by forcefully displacing Cs^+ when a high voltage is applied. This reflects on the one hand the improved stability but on the other hand the reduced self-healing property of inorganic perovskite over hybrid perovskite under working conditions.

In the second part, we emphasized the charge carrier transfer and recombination mechanism between perovskite and the ETMs TiO_2 and PCBM as well as several polymer-based HTMs and spiro-OMeTAD. We demonstrated the beneficial incorporation of $FAPbI_3$ NCs into a DPP:PCBM-based polymer solar cell (fabricated in the group of Dr. Ameri). These $FAPbI_3$ NCs accumulate at the grain boundaries between the polymer and the fullerene derivative and, consequently, reduce the interface between donor and acceptor. Firstly, perovskite acts as second light absorber within the ternary blend that is complementary to DPP and, thus, improves the overall light absorption of the active layer. Secondly, $FAPbI_3$ NCs mediate the charge carrier separation across DPP and PCBM *via* an additional transfer pathway. In this way, perovskite improves the generation of free charge carriers as well as inhibits recombination between DPP^+ and $PCBM^-$ or the electron re-injection into the triplet

excited state of DPP. The optimum $FAPbI_3$ NCs concentration was found to be 5 wt%, where the lifetime of the charge separated state in ternary blends is up to 13% longer than in binary blends. Highest efficiencies in solar cells were obtained with a ratio of 1:0.05:2 for DPP:FAPI:PCBM, achieving a PCE of 5.5 ± 0.3% compared to 5.0 ± 0.4% for the binary blend (performed in the group of Dr. Ameri).

Thereafter, we investigated electron injection from the perovskite into PCBM while varying the ETM layer's crystallinity. Polycrystalline PCBM NPs obtained from nanoemulsion (prepared in the group of Prof. Brabec) were utilized within an n-type thin-film architecture solar cell and referenced to the standard compact PCBM. Here, the PCBM NPs self-assemble into a mesoscale-structured layer that has a larger interface and a less perturbed density of states, caused by its polycrystallinity, compared to a compact layer of amorphous PCBM. Consequently, electrons are more efficiently harvested by (i) an increased interface and (ii) ultrafast injection into a more discrete LUMO of PCBM NPs. On top of this, hot electrons were harvested before thermalization by their transfer into higher energy levels within PCBM NPs. While perovskite transfers hot electrons into both polycrystalline and compact PCBM, a fast re-injection into perovskite's CB was observed for compact PCBM only. For solar cells using PCBM NPs, an improved interaction between perovskite and ETM layer enables reproducible PCEs and a fabrication of devices with larger active layer without compromising its efficiency (prepared in the group of Prof. Brabec).

Finally, we studied the charge carrier transfer process across the interface of perovskite and several HTMs in bilayer samples (fabricated in the group of Prof. Palomares). We corroborated a fast hole injection in a subpico-second to 2 ps time frame for spiro-OMeTAD as well as the polymer-based HTMs PTB7, P3HT, and PCPDTBT. Surprisingly, for PCPDTBT, we additionally observed hot electron injection from the perovskite into the polymer's LUMO, which is the energetically lowest of the four HTMs. In the light of increasing laser intensity, the hot electron transfer and, particularly, the back-injection into perovskite's CB was investigated. Here, trapped electrons within the HTM remain longer in PCPDTBT for lower laser intensities. This finding elucidates a bright luminescence of perovskite in the presence of PCPDTBT and, accordingly, the low photocurrent and PCE (measured in the group of Prof. Palomares) of solar cells using PCPDTBT as HTM. As such, future designs of HTMs for PSCs can be improved using energetically high LUMO levels.

6. Zusammenfassung

Zusammengefasst bietet diese Arbeit ein tiefgreifendes Verständnis der in Bleihalogenid-Perowskit-Materialien vorherrschenden ionischen Diffusionsprozessen und der Interaktionen zwischen Perowskiten und sowohl Lochleitern als auch Elektronenleitern mittels der Betrachtung von Injektions- und Rekombinationsprozessen. Hierbei wurde festgestellt, dass die besonderen Eigenschaften der Perowskite, wie zum Beispiel eine schnelle Erzeugung freier Ladungsträger und relativ langlebige heiße Elektronen, zusätzliche Injektionskanäle zur Ladungsträgerübertragungen ermöglichen. Die Beobachtungen wurden mittels elektrochemischen Messmethoden wie Voltammetrie, Amperometrie, und Impedanzspektroskopie sowie durch zeitaufgelöste Transiente-Absorptions-spektroskopie im Femtosekundenbereich untersucht.

Im ersten Teil fokussierten wir uns auf die intrinsischen Eigenschaften von Perowskiten, wie die ionische Leitfähigkeit. Wir zeigten, dass bei einer angelegten Spannung hybrides Perowskit wie beispielsweise $MAPbBr_3$ (hergestellt im Arbeitskreis Dr. Docampo) sich durch zwei diffundierende Komponenten auszeichnet. Demgegenüber haben anorganische Perowskite wie $CsPbBr_3$ nur eine diffundierende Spezies. In beiden Materialien diffundieren die Halogenide und deren Fehlstellen, die eine niedrige Diffusionsaktivierungsenergie aufweisen, am schnellsten. Die trägeren Komponenten sind die organischen **A**-Kationen MA^+, welche sich nicht nur im elektrischen Feld ausrichten, sondern sich auch zusammen mit ihren Fehlstellen innerhalb des Kristallgitters bewegen können. $CsPbBr_3$ hat im Gegensatz zu $MAPbBr_3$ ein **A**-Kation mit geringerem fluidem Charakter, und entsprechend verbleibt Cs^+ im Kristallgitter. Unter Anlegen einer hohen Spannung kann Cs^+ zu einer Verschiebung gezwungen werden, wodurch es jedoch zur Zersetzung von $CsPbBr_3$ kommt. Diese Beobachtung spiegelt einerseits die verbesserte Stabilität, aber auch die verringerte Selbstheilungsrate von anorganischem Perowskit-Materialien im Vergleich zu hybriden Perowskit-Materialien wider.

Im zweiten Teil wurde der Mechanismus der Ladungsträgerinjektion und -rekombination zwischen hybridem Perowskit-Material und den Elektronleitern TiO_2 und PCBM sowie verschiedenen polymerbasierten Lochleitern und spiro-OMeTAD untersucht. Dabei konnten wir die positive Wirkung von $FAPbI_3$ Nanokristallen auf den Wirkungsgrad der DPP:PCBM-beruhenden Polymersolarzellen

zeigen (hergestellt im Arbeitskreis Dr. Ameri). Diese Nanokristalle lagern sich an den Korngrenze zwischen dem Polymer und dem Fullerenderivaten an und reduzieren folglich die Grenzfläche zwischen den Elektronendonatoren und -akzeptoren. Innerhalb einer ternären Mischung agieren die Perowskit-Nanokristalle einerseits als zweiter Lichtabsorber, welcher komplementär zu DPP ist und somit die Lichtabsorption des aktiven Films erhöht. Andererseits helfen die Perowskit-Nanokristalle durch einen zusätzlichen Transferkanal bei der Trennung der Ladungsträger an der DPP-PCBM-Grenzfläche. Auf diese Weise erhöht das Perowskit die Anzahl erzeugter freier Ladungsträger und verhindert die Rekombination zwischen DPP^+ und $PCBM^-$ wie auch den Elektronrücktransfer in den Triplettzustand des DPPs. Die optimale Konzentration der $FAPbI_3$ Nanokristalle lag bei 5 Gewichtsprozent. Dies erhöht im Vergleich zur binären Mischung die Lebenszeit der Ladungstrennung innerhalb der ternären Mischung um 13%. Die besten Wirkungsgrade der Solarzellen wurden bei einem Verhältnis von 1:0.05:2 für DPP:FAPI:PCBM erreicht und belaufen sich auf 5.5 ± 0.3%. Im Vergleich erreichen Solarzellen mit binären Mischungen 5.0 ± 0.4% (gemessen im Arbeitskreis Dr. Ameri).

Darauffolgend untersuchten wir die Elektroneninjektion von hybridem Perowskit-Material ins PCBM im Hinblick auf die Kristallinität des elektronleitenden Filmes. Polykristalline PCBM-Nanopartikel wurden durch Nanoemulsion gewonnen (hergestellt im Arbeitskreis Prof. Brabec) und in n-leitenden Dünnfilmsolarzellen verarbeitet. Als Referenz dienten dabei standardisierte kompakte PCBM-Lagen. Die PCBM-Nanopartikel lagern sich selbstständig als ein mesoporös-strukturierter Film an, welcher eine größere Oberfläche und durch seine polykristalline Art eine geringere Verteilung der Zustandsdichte hat als amorphes PCBM im kompakten Film. Infolgedessen werden Elektronen effizienter gesammelt. Dies geschieht durch (i) eine vergrößerte Grenzfläche und (ii) ultraschnelle Injektion in diskretere unbesetzte Orbitale der PCBM-Nanopartikel. Zusätzlich können heiße Elektronen vor ihrer Thermalisierung in energiehöhere, unbesetzte Orbitale der Nanopartikel injiziert werden. Obwohl eine Übertragung der heißen Elektronen für beide Arten der PCBM Dünnfilmen beobachtbar ist, findet nur für kompaktes PCBM eine Rückinjektion in das Leitungsband des Perowskits statt. Solarzellen, die eine Dünnschicht der PCBM-Nanopartikel verwenden, zeichnen sich durch eine verbesserte Wechselwirkung zwischen dem Perowskit und dem elektronleitenden Material aus, wodurch es zu gesteigerter Reproduzierbarkeit der Wirkungsgrade kommt (gemessen im Arbeitskreis

Prof. Brabec). Außerdem ist es möglich effiziente Solarzellen mit einer größeren aktiven Oberfläche zu bauen.

Abschließend haben wir die Ladungsträgerübertragung an der Grenzfläche der Doppelschichten von hybridem Perowskit mit verschiedenen lochleitenden Materialien untersucht (hergestellt im Arbeitskreis Prof. Palomares). Wir haben bewiesen, dass sowohl für spiro-OMeTAD als auch lochleitende Polymere wie PTB7, P3HT und PCPDTBT die schnelle Lochinjektion innerhalb eines Zeitrahmens im Subpikosekundenbereich bis zu 2 ps stattfindet. Interessanterweise entdeckten wir dabei die Übertragung von heißen Elektronen des Perowskits in unbesetzte Orbitale des Polymers PCPDTBT, welches das tiefliegendste LUMO der vier lochleitenden Materialien hat. Mittels ansteigender Laserintensitäten konnten wir die Übertragung der heißen Elektronen und besonders ihre Rückinjektion in das Leitungsband des Perowskits untersuchen. Hierbei stellte sich heraus, dass bei einer niedrigen Laserintensität die im Lochleiter festsitzenden Elektronen länger verweilen. Diese Beobachtungen erklären die helle Lumineszenz der Perowskit-Filme in Doppelschichten mit dem Lochleiter PCPDTBT und entsprechend auch den niedrigen Fotostrom und Wirkungsgrad (gemessen im Arbeitskreis Prof. Palomares) der Solarzellen, welche PCPDTBT als Lochleiter haben. Daher ist es ratsam beim Design neuer Lochleiter für Perowskit-Solarzellen auf ein energetisch hohes LUMO zu achten.

7. Acknowledgements

First, I would like to express my deepest gratitude to Prof. Dr. Dirk M. Guldi. He offered me the opportunity to work on this fascinating topic and his guidance and support was ever-present on this journey.

Further, I would like to thank the whole Guldi group for their support and help. In particular, I would like to thank the members of my office for the fruitful discussions and the inspiring atmosphere, which accounts especially for Dr. Rubén D. Costa, Dr. Andreas Kunzmann, Dr. Rubén Casillas, and Katharina Weber, as well as my Bachelor student Lena Nguyen. I also want to express my deepest appreciation to the Femto team, namely Bettina Basel, Stefan Bauroth, Sebastian Heiß, Ramandeep Kaur, Marcel Krug, Dominik Thiel, Tobias Ullrich, Dr. Maximilian Wolf, and Dr. Johannes Zirzlmeier, and their hard work on enabling best measuring conditions. I would like to thank all present and former members for the great atmosphere and memories I experienced.

I would also like to address deep gratitude to Prof. Dr. Rainer H. Fink, who supported me during my Bachelor thesis, my Master thesis, as well as my dissertation, and enabled my research stay abroad.

I also express my gratitude to all cooperation partners for their great effort and significant contribution to this work: Dr. Pablo Docampo and Dr. Meltem F. Aygüler from the Newcastle University and from the Ludwig-Maximilian-University in Munich; Prof. Dr. Christoph J. Brabec, Dr. Tayebeh Ameri, Dr. Yi Hou, Dr. Ievgen Levchuk, and Dr. Rezvan Soltani from the Institute Materials for Electronics and Energy; Prof. Dr. Emilio Palomarez, Dr. Jesús Jiménez-López, and Werther Cambarau from Institute of Chemical Research of Catalonia. I would also like to express my thanks to Prof. Dr. Anders Hagfeldt, Dr. Gerrit Boschloo, and Dr. Erik M. J. Johansson for my research stay at the University of Uppsala and want to thank them and the whole working group for their kind hospitality.

I also want to thank Gerd Gätzschmann, Angelika Leistner, Manfred Pfennig, Dorjkhand Rudolph, and Corinne Wiegner as well as Friedhold Wölfel and his workshop team Bernd Hofmann, Thomas Hofmann, Werner Höfler, and Viola Ziegler for their constant support. Further, I express my gratitude to the Akademischen Räte Dr. Christian Ehli, Dr. Karin Mansyreff, and Dr. Guido Sauer as well as the secretaries Margit Hartmann and Beate Maaß for their outstanding help.

I, also, want to thank my friends at university for a fantastic atmosphere within the EAM and department community as well my friends outside of university for the work-life-balance. Finally, I want to express my deepest gratitude and appreciation to my parents and Dr. Olaf Brummel for their patience, help, and strong support.

8. Literature

1 J. A. J. Gowlett and R. W. Wrangham, Earliest fire in Africa: towards the convergence of archaeological evidence and the cooking hypothesis, *Azania*, 2013, **48**, 5–30.

2 V. Smil, *Energy transitions: global and national perspectives*, Praeger, 2nd edn., 2016.

3 BP, Statistical review of world energy, https://www.bp.com/content/dam/bp/business-sites/en/global/corporate/pdfs/energy-economics/statistical-review/bp-stats-review-2018-full-report.pdf, (accessed 11 April 2019).

4 Bundesministerium für Wirtschaft und Energie, Primärenergieverbrauch in Deutschland 2017, https://www.bmwi.de/Redaktion/DE/Infografiken/Energie/Energiedaten/Energiegewinnung-und-Energieverbrauch/energiedaten-energiegewinnung-verbrauch-03.html, (accessed 11 April 2019).

5 Umweltbundesamt, Energieverbrauch nach Energieträgern, Sektoren und Anwendungen, https://www.umweltbundesamt.de/daten/energie/energieverbrauch-nach-energietraegern-sektoren, (accessed 11 April 2019).

6 G. Ourisson, P. Albrecht and M. Rohmer, The microbial origin of fossil fuels, *Sci. Am.*, 2010, **251**, 44–51.

7 E. W. Tegelaar, J. W. de Leeuw, S. Derenne and C. Largeau, A reappraisal of kerogen formation, *Geochim. Cosmochim. Acta*, 1989, **53**, 3103–3106.

8 C. N. Waters, J. Zalasiewicz, C. Summerhayes, A. D. Barnosky, C. Poirier, A. Galuszka, A. Cearreta, M. Edgeworth, E. C. Ellis, M. Ellis, C. Jeandel, R. Leinfelder, J. R. McNeill, D. deB. Richter, W. Steffen, J. Syvitski, D. Vidas, M. Wagreich, M. Williams, A. Zhisheng, J. Grinevald, E. Odada, N. Oreskes and A. P. Wolfe, The Anthropocene is functionally and stratigraphically distinct from the Holocene, *Science*, 2016, **351**, aad2622.

9 M. E. Sosa Torres, J. P. Saucedo-Vázquez and P. M. H. Kroneck, in *Kroneck P. M. H., Sosa Torres M. E. Sustaining life on planet Earth: metalloenzymes mastering dioxygen and other chewy gases*, Springer, 2015, pp. 1–12.

10 Das Forschungsinstitut für biologischen Landbau, Global organic farming statistics and news, https://www.organic-world.net/yearbook/yearbook-2019/infographics.html#c17493, (accessed 11 April 2019).

11 United Nations, The Paris agreement, http://unfccc.int/paris_agreement/items/9485.php, (accessed 11 April 2019).

12 R. C. Ewing, Long-term storage of spent nuclear fuel, *Nat. Mater.*, 2015, **14**, 252–257.

13 N. A. Beresford and D. Copplestone, Effects of ionizing radiation on wildlife: what knowledge have we gained between the chernobyl and fukushima accidents?, *Integr. Environ. Assess. Manag.*, 2011, **7**, 371–373.

14 K. Kamiya, K. Ozasa, S. Akiba, O. Niwa, K. Kodama, N. Takamura, E. K. Zaharieva, Y. Kimura and R. Wakeford, Long-term effects of radiation exposure on health, *Lancet*, 2015, **386**, 469–478.

15 World Commission on Environment and Development, *Brundtland report - our common future*, Oxford University Press, 1987.

16 Y. Gao, M. Skutsch, R. Drigo, P. Pacheco and O. Masera, Assessing deforestation from biofuels: methodological challenges, *Appl. Geogr.*, 2011, **31**, 508–518.

17 O. R. Inderwildi and D. A. King, Quo vadis biofuels?, *Energy Environ. Sci.*, 2009, **2**, 343–346.

18 E. Kabir, P. Kumar, S. Kumar, A. A. Adelodun and K.-H. Kim, Solar energy: potential and future prospects, *Renew. Sustain. Energy Rev.*, 2018, **82**, 894–900.

19 B. Kahn, This is what 4 million solar panels look like from space, https://www.climatecentral.org/news/china-solar-farm-satellite-21182, (accessed 11 April 2019).

20 NASA, The edge of sunshine, https://science.nasa.gov/science-news/science-at-nasa/2002/08jan_sunshine/, (accessed 11 April 2019).

21 A. E. Becquerel, Mémoire sur les effets électriques produits sous l'influence des rayons solaires, *Comptes Rendus des Séances Hebd.*, 1839, **9**, 561–567.

22 L. El Chaar, L. A. Lamont and N. El Zein, Review of photovoltaic technologies, *Renew. Sustain. Energy Rev.*, 2011, **15**, 2165–2175.

23 A. W. Copeland, O. D. Black and A. B. Garrett, The photovoltaic effect, *Chem. Rev.*, 1942, **31**, 177–226.

24 C. E. Fritts, On a new form of selenium cell, and some electrical discoveries made by its use, *Am. J. Sci.*, 1883, **s3**-**26**, 465–472.

25 *United States Pat. Off. 2402662*, 1941, 1–14.

26 A. Einstein, On a heuristic point of view about the creation and conversion of Light (German: Über einen die Erzeugung und Verwandlung des Lichtes betreffenden heuristischen Gesichtspunkt), *Ann. Phys.*, 1905, **322**, 132–148.

27 A. Blakers, N. Zin, K. R. McIntosh and K. Fong, High efficiency silicon solar cells, *Energy Procedia*, 2013, **33**, 1–10.

28 National Renewable Energy Laboratory (NREL), https://www.nrel.gov/pv/assets/pdfs/pv-efficiency-chart.20190103.pdf, (accessed 10 April 2019).

29 C. H. Lee, D. R. Kim, I. S. Cho, N. William, Q. Wang and X. Zheng, Peel-and-stick: fabricating thin film solar cell on universal substrates, *Sci. Rep.*, 2012, **2**, 1000.

30 W. Qarony, M. I. Hossain, M. K. Hossain, U. M. Jalal, A. Haque, A. R. Saad and Y. H. Tsang, Efficient amorphous silicon solar cells: characterization, optimization, and optical loss analysis, *Results Phys.*, 2017, **7**, 4287–4293.

31 J. Britt and C. Ferekides, Thin-film CdS/CdTe solar cell with 15.8% efficiency, *Appl. Phys. Lett.*, 1993, **62**, 2851–2852.

32 M. Konagai, M. Sugimoto and K. Takahashi, High efficiency GaAs thin film solar cells by peeled film technology, *J. Cryst. Growth*, 1978, **45**, 277–280.

33 M. A. Contreras, B. Egaas, K. Ramanathan, J. Hiltner, A. Swartzlander, F. Hasoon and R. Noufi, Progress toward 20% efficiency in Cu(In,Ga)Se_2 polycrystalline thin-film solar cells, *Prog. Photovoltaics Res. Appl.*, 1999, **7**, 311–316.

34 W. Shockley and H. J. Queisser, Detailed balance limit of efficiency of p-n junction solar cells, *J. Appl. Phys.*, 1961, **32**, 510–519.

35 T. Ameri, N. Li and C. J. Brabec, Highly efficient organic tandem solar cells: a follow up review, *Energy Environ. Sci.*, 2013, **6**, 2390–2413.

36 O. Langmar, E. Fazio, P. Schol, G. de la Torre, R. D. Costa, T. Torres and D. M. Guldi, Controlling interfacial charge transfer and fill factors in CuO-based tandem dye-sensitized solar cells, *Angew. Chem. Int. Ed.*, 2019, **58**, 4056–4060.

37 M. K. Siddiki, J. Li, D. Galipeau and Q. Qiao, A review of polymer multijunction solar cells, *Energy Environ. Sci.*, 2010, **3**, 867–883.

38 A. Kunzmann, M. Gruber, R. Casillas, J. Zirzlmeier, M. Stanzel, W. Peukert, R. R. Tykwinski and D. M. Guldi, Singlet fission for photovoltaics with 130% injection efficiency, *Angew. Chem. Int. Ed.*, 2018, **57**, 10742–10747.

39 J. N. Schrauben, Y. Zhao, C. Mercado, P. I. Dron, J. L. Ryerson, J. Michl, K. Zhu and J. C. Johnson, Photocurrent enhanced by singlet fission in a dye-sensitized solar cell, *ACS Appl. Mater. Interfaces*, 2015, **7**, 2286–2293.

40 K. Tanabe, A review of ultrahigh efficiency III-V semiconductor compound solar cells: multijunction tandem, lower dimensional, photonic up/down conversion and plasmonic

nanometallic structures, *Energies*, 2009, **2**, 504–530.

41 B. P. Rand, J. Genoe, P. Heremans and J. Poortmans, Solar cells utilizing small molecular weight organic semiconductors, *Prog. Photovoltaics Res. Appl.*, 2007, **15**, 659–676.

42 H. Zhang, Y. Liu, Y. Sun, M. Li, B. Kan, X. Ke, Q. Zhang, X. Wan and Y. Chen, Developing high-performance small molecule organic solar cells via a large planar structure and an electron-withdrawing central unit, *Chem. Commun.*, 2017, **53**, 451–454.

43 F. C. Krebs, Fabrication and processing of polymer solar cells: a review of printing and coating techniques, *Sol. Energy Mater. Sol. Cells*, 2009, **93**, 394–412.

44 J. Gong, K. Sumathy, Q. Qiao, Z. Zhou, J. Liang and K. Sumathy, Review on dye-sensitized solar cells (DSSCs): advanced techniques and research trends, *Renew. Sustain. Energy Rev.*, 2017, **68**, 5848–5860.

45 K. Kakiage, Y. Aoyama, T. Yano, K. Oya, J. I. Fujisawa and M. Hanaya, Highly-efficient dye-sensitized solar cells with collaborative sensitization by silyl-anchor and carboxy-anchor dyes, *Chem. Commun.*, 2015, **51**, 15894–15897.

46 S. Il Seok, M. Grätzel and N.-G. Park, Methodologies toward highly efficient perovskite solar cells, *Small*, 2018, **14**, 1704177.

47 E. H. Jung, N. J. Jeon, E. Y. Park, C. S. Moon, T. J. Shin, T.-Y. Yang, J. H. Noh and J. Seo, Efficient, stable and scalable perovskite solar cells using poly(3-hexylthiophene), *Nature*, 2019, **567**, 511–515.

48 M. Saliba, T. Matsui, J.-Y. Seo, K. Domanski, J.-P. Correa-Baena, M. K. Nazeeruddin, S. M. Zakeeruddin, W. Tress, A. Abate, A. Hagfeldt, M. Gratzel, N. Mohammad K., S. M. Zakeeruddin, W. Tress, A. Abate, A. Hagfeldt and M. Gratzel, Cesium-containing triple cation perovskite solar cells: improved stability, reproducibility and high efficiency, *Energy Environ. Sci.*, 2016, **9**, 1989–1997.

49 Z. Wei, H. Chen, K. Yan and S. Yang, Inkjet printing and instant chemical transformation of a $CH_3NH_3PbI_3$/nanocarbon electrode and interface for planar perovskite solar cells, *Angew. Chem. Int. Ed.*, 2014, **53**, 13239–13243.

50 M. Shirayama, M. Kato, T. Miyadera, T. Sugita, T. Fujiseki, S. Hara, H. Kadowaki, D. Murata, M. Chikamatsu and H. Fujiwara, Degradation mechanism of $CH_3NH_3PbI_3$ perovskite materials upon exposure to humid air, *J. Appl. Phys.*, 2016, **119**, 115501.

51 P. Wang, X. Zhang, Y. Zhou, Q. Jiang, Q. Ye, Z. Chu, X. Li, X. Yang, Z. Yin and J. You, Solvent-controlled growth of inorganic perovskite films in dry environment for efficient and stable solar cells, *Nat. Commun.*, 2018, **9**, 2225.

52 N. K. Kim, Y. H. Min, S. Noh, E. Cho, G. Jeong, M. Joo, S. W. Ahn, J. S. Lee, S. Kim, K. Ihm, H. Ahn, Y. Kang, H. S. Lee and D. Kim, Investigation of thermally induced degradation in $CH_3NH_3PbI_3$ perovskite solar cells using in-situ synchrotron radiation analysis, *Sci. Rep.*, 2017, **7**, 4645.

53 E. J. Juarez-Perez, L. K. Ono, M. Maeda, Y. Jiang, Z. Hawash and Y. Qi, Photodecomposition and thermal decomposition in methylammonium halide lead perovskites and inferred design principles to increase photovoltaic device stability, *J. Mater. Chem. A*, 2018, **6**, 9604–9612.

54 P. Yadav, D. Prochowicz, E. A. Alharbi, S. M. Zakeeruddin and M. Grätzel, Intrinsic and interfacial kinetics of perovskite solar cells under photo and bias-induced degradation and recovery, *J. Mater. Chem. C*, 2017, **5**, 7799–7805.

55 W. Nie, J.-C. Blancon, A. J. Neukirch, K. Appavoo, H. Tsai, M. Chhowalla, M. A. Alam, M. Y. Sfeir, C. Katan, J. Even, S. Tretiak, J. J. Crochet, G. Gupta and A. D. Mohite, Light-activated photocurrent degradation and self-healing in perovskite solar cells, *Nat. Commun.*, 2016, **7**, 11574.

56 M. Saliba, T. Matsui, K. Domanski, J.-Y. Seo, A. Ummadisingu, S. M. Zakeeruddin, J.-P. Correa-Baena, W. R. Tress, A. Abate, A. Hagfeldt and M. Gratzel, Incorporation of rubidium cations into perovskite solar cells improves photovoltaic performance, *Science*, 2016, **354**, 206–209.

57 W. Zhou, Y. Y. Zhao, X. Zhou, R. Fu, Q. Li, Y. Y. Zhao, K. Liu, D. Yu and Q. Zhao, Light-independent ionic transport in inorganic perovskite and ultrastable Cs-based perovskite solar cells, *J. Phys. Chem. Lett.*, 2017, **8**, 4122–4128.

58 N. Arora, M. I. Dar, A. Hinderhofer, N. Pellet, F. Schreiber, S. M. Zakeeruddin and M. Grätzel, Perovskite solar cells with CuSCN hole extraction layers yield stabilized efficiencies greater than 20%, *Science*, 2017, **358**, 768–771.

59 Y. Zong, Y. Zhou, Y. Zhang, Z. Li, L. Zhang, M. G. Ju, M. Chen, S. Pang, X. C. Zeng and N. P. Padture, Continuous grain-boundary functionalization for high-efficiency perovskite solar cells with exceptional stability, *Chem*, 2018, **4**, 1404–1415.

60 G. Rose, Beschreibung einiger neuen Mineralien des Urals, *Ann. Phys.*, 1840, **126**, 652–656.

61 R. E. Wasylishen, O. Knop and J. B. Macdonald, Cation rotation in methylammonium lead halides, *Solid State Commun.*, 1985, **56**, 581–582.

62 D. Weber, $CH_3NH_3PbX_3$, ein Pb(II)-System mit kubischer Perowskitstruktur, *Verlag der Zeitschrift für Naturforsch.*, 1978, **1445**, 1443–1445.

63 M. V. S. Narayan, R. Lakshmisarma and S. V. Suryanarayana, Iionic conductivity of $CsPbCl_3$ and $CsPbBr_3$, *J. Mater. Sci. Lett.*, 1987, **6**, 93–94.

64 J. Mizusaki, K. Arai and K. Fueki, Iionic conduction of the perovskite-type halides, *Solid State Ionics*, 1983, **11**, 203–211.

65 T. Kuku, Ionic transport and galvanic cell discharge characteristics of $CuPbI_3$ thin films, *Thin Solid Films*, 1998, **325**, 246–250.

66 R. L. Narayan and S. V. Suryanarayana, Transport properties of the perovskite-type halides, *Mater. Lett.*, 1991, **11**, 305–308.

67 O. Knop, R. E. Wasylishen, M. A. White, T. S. Cameron and M. J. M. Van Oort, Alkylammonium lead halides. Part 2. $CH_3NH_3PbX_3$ (X = Cl, Br, I) perovskites: cuboctahedral halide cages with isotropic cation reorientation, *Can. J. Chem.*, 1990, **68**, 412–422.

68 M. Hirasawa, T. Ishihara, T. Goto, K. Uchida and N. Miura, Magnetoabsorption of the lowest exciton in perovskite-type compound $(CH_3NH_3)PbI_3$, *Phys. B Condens. Matter*, 1994, **201**, 427–430.

69 C. C. Stoumpos, C. D. Malliakas and M. G. Kanatzidis, Semiconducting tin and lead iodide perovskites with organic cations: phase transitions, high mobilities, and near-infrared photoluminescent properties, *Inorg. Chem.*, 2013, **52**, 9019–9038.

70 P. S. Whitfield, N. Herron, W. E. Guise, K. Page, Y. Q. Cheng, I. Milas and M. K. Crawford, Structures, phase transitions and tricritical behavior of the hybrid perovskite methyl ammonium lead iodide, *Sci. Rep.*, 2016, **6**, 35685.

71 A. Kojima, K. Teshima, Y. Shirai and T. Miyasaka, Organometal halide perovskites as visible-light sensitizers for photovoltaic cells, *J. Am. Chem. Soc.*, 2009, **131**, 6050–6051.

72 K. Leo, Signs of stability, *Nat. Nanotechnol.*, 2015, **10**, 574–575.

73 M. M. Lee, J. Teuscher, T. Miyasaka, T. N. Murakami and H. J. Snaith, Efficient hybrid solar cells based on meso-superstructured organometal halide perovskites, *Science*, 2012, **338**, 643–647.

74 N. Ahn, D. Y. Son, I. H. Jang, S. M. Kang, M. Choi and N. G. Park, Highly reproducible perovskite solar cells with average efficiency of 18.3% and best efficiency of 19.7% fabricated via Lewis base adduct of lead(II) iodide, *J. Am. Chem. Soc.*, 2015, **137**, 8696–8699.

75 A. Kogo, Y. Sanehira, Y. Numata, M. Ikegami and T. Miyasaka, Amorphous metal oxide blocking layers for highly efficient low-temperature brookite TiO_2-based perovskite solar cells, *ACS Appl. Mater. Interfaces*, 2018, **10**, 2224–2229.

76 Q. Jiang, Y. Zhao, X. Zhang, X. Yang, Y. Chen, Z. Chu, Q. Ye, X. Li, Z. Yin and J. You, Surface passivation of perovskite film for efficient solar cells, *Nat. Photonics*, 2019, **13**, 460–466.

77 S. Sun, T. Salim, N. Mathews, M. Duchamp, C. Boothroyd, G. Xing, T. C. Sum and Y. M. Lam, The origin of high efficiency in low-temperature solution-processable bilayer organometal halide hybrid solar cells, *Energy Environ. Sci.*, 2014, **7**, 399–407.

78 C. Wehrenfennig, M. Liu, H. J. Snaith, M. B. Johnston and L. M. Herz, Homogeneous emission line broadening in the organo lead halide perovskite $CH_3NH_3PbI_{3-x}Cl_x$, *J. Phys. Chem. Lett.*, 2014, **5**, 1300–1306.

79 M. A. Green, A. Ho-Baillie and H. J. Snaith, The emergence of perovskite solar cells, *Nat. Photonics*, 2014, **8**, 506–514.

80 N. J. Jeon, J. H. Noh, W. S. Yang, Y. C. Kim, S. Ryu, J. Seo and S. Il Seok, Compositional engineering of perovskite materials for high-performance solar cells, *Nature*, 2015, **517**, 476–480.

81 O. A. Jaramillo-Quintero, R. S. Sánchez, M. Rincón and I. Mora-Sero, Bright visible-infrared light emitting diodes based on hybrid halide perovskite with spiro-OMeTAD as a hole injecting layer, *J. Phys. Chem. Lett.*, 2015, **6**, 1883–1890.

82 G. Nedelcu, L. Protesescu, S. Yakunin, M. I. Bodnarchuk, M. J. Grotevent and M. V. Kovalenko, Fast anion-exchange in highly luminescent nanocrystals of cesium lead halide perovskites (CsPbX3, X = Cl, Br, I), *Nano Lett.*, 2015, **15**, 5635–5640.

83 L. Protesescu, S. Yakunin, M. I. Bodnarchuk, F. Krieg, R. Caputo, C. H. Hendon, R. X. Yang, A. Walsh and M. V. Kovalenko, Nanocrystals of cesium lead halide perovskites ($CsPbX_3$, X = Cl, Br, and I): novel optoelectronic materials showing bright emission with wide color gamut, *Nano Lett.*, 2015, **15**, 3692–3696.

84 N. K. Kumawat, A. Dey, K. L. Narasimhan and D. Kabra, Near infrared to visible electroluminescent diodes based on organometallic halide perovskites: structural and optical investigation, *ACS Photonics*, 2015, **2**, 349–354.

85 Z.-K. Tan, R. S. Moghaddam, M. L. Lai, P. Docampo, R. Higler, F. Deschler, M. Price, A. Sadhanala, L. M. Pazos, D. Credgington, F. Hanusch, T. Bein, H. J. Snaith and R. H. Friend, Bright light-emitting diodes based on organometal halide perovskite, *Nat. Nanotechnol.*, 2014, **9**, 687–692.

86 K. Chondroudis and D. B. Mitzi, Electroluminescence from an organic−inorganic perovskite incorporating a quaterthiophene dye within lead halide perovskite layers, *Chem. Mater.*, 1999, **11**, 3028–3030.

87 M. F. Aygüler, M. D. Weber, B. M. D. Puscher, D. D. Medina, P. Docampo and R. D. Costa, Light-emitting electrochemical cells based on hybrid lead halide perovskite nanoparticles, *J. Phys. Chem. C*, 2015, **119**, 12047–12054.

88 M. F. Aygüler, B. M. D. Puscher, Y. Tong, T. Bein, A. S. Urban, R. D. Costa and P. Docampo, Light-emitting electrochemical cells based on inorganic metal halide perovskite nanocrystals, *J. Phys. D. Appl. Phys.*, 2018, **51**, 334001.

89 K. Lin, J. Xing, L. N. Quan, F. P. G. de Arquer, X. Gong, J. Lu, L. Xie, W. Zhao, D. Zhang, C. Yan, W. Li, X. Liu, Y. Lu, J. Kirman, E. H. Sargent, Q. Xiong and Z. Wei, Perovskite light-emitting diodes with external quantum efficiency exceeding 20 per cent, *Nature*, 2018, **562**, 245–248.

90 B. Zhao, S. Bai, V. Kim, R. Lamboll, R. Shivanna, F. Auras, J. M. Richter, L. Yang, L. Dai, M. Alsari, X.-J. She, L. Liang, J. Zhang, S. Lilliu, P. Gao, H. J. Snaith, J. Wang, N. C. Greenham, R. H. Friend and D. Di, High-efficiency perovskite–polymer bulk heterostructure light-emitting diodes, *Nat. Photonics*, 2018, **12**, 783–789.

91 C. Wehrenfennig, G. E. Eperon, M. B. Johnston, H. J. Snaith and L. M. Herz, High charge carrier mobilities and lifetimes in organolead trihalide perovskites, *Adv. Mater.*, 2014, **26**, 1584–1589.

92 M. J. P. Alcocer, T. Leijtens, L. M. Herz, A. Petrozza, H. J. Snaith, S. D. Stranks, G. E. Eperon, G. Grancini, C. Menelaou, M. J. P. Alcocer, T. Leijtens, L. M. Herz, A. Petrozza and H. J. Snaith, Electron-hole diffusion lengths exceeding 1 micrometer in an organometal trihalide perovskite absorber, *Science*, 2013, **342**, 341–344.

93 Y. Yamada, T. Nakamura, M. Endo, A. Wakamiya and Y. Kanemitsu, Photocarrier recombination dynamics in perovskite $CH_3NH_3PbI_3$ for solar cell applications, *J. Am. Chem. Soc.*, 2014, **136**, 11610–11613.

94 C. S. Ponseca, T. J. Savenije, M. Abdellah, K. Zheng, A. Yartsev, T. Pascher, T. Harlang, P. Chabera, T. Pullerits, A. Stepanov, J. P. Wolf and V. Sundström, Organometal halide perovskite solar cell materials rationalized: ultrafast charge generation, high and microsecond-long balanced mobilities, and slow recombination, *J. Am. Chem. Soc.*, 2014, **136**, 5189–5192.

95 J. Even, L. Pedesseau and C. Katan, Analysis of multivalley and multibandgap absorption and enhancement of free carriers related to exciton screening in hybrid perovskites, *J. Phys. Chem. C*, 2014, **118**, 11566–11572.

96 Y. Yang, D. P. Ostrowski, R. M. France, K. Zhu, J. van de Lagemaat, J. M. Luther and M. C. Beard, Observation of a hot-phonon bottleneck in lead-iodide perovskites, *Nat. Photonics*, 2015, **10**, 53–59.

97 Y. Yamada, T. Nakamura, M. Endo, A. Wakamiya and Y. Kanemitsu, Photoelectronic responses in solution-processed perovskite $CH_3NH_3PbI_3$ solar cells studied by photoluminescence and photoabsorption spectroscopy, *IEEE J. Photovoltaics*, 2015, **5**, 401–405.

98 R. L. Milot, G. E. Eperon, H. J. Snaith, M. B. Johnston and L. M. Herz, Temperature-dependent charge-carrier dynamics in $CH_3NH_3PbI_3$ perovskite thin films, *Adv. Funct. Mater.*, 2015, **25**, 6218–6227.

99 C. Wehrenfennig, M. Liu, H. J. Snaith, M. B. Johnston and L. M. Herz, Charge-carrier dynamics in vapour-deposited films of the organolead halide perovskite $CH_3NH_3PbI_{3-x}Cl_x$, *Energy Environ. Sci.*, 2014, **7**, 2269–2275.

100 J. K. Nam, D. H. Chun, R. J. K. Rhee, J. H. Lee and J. H. Park, Methodologies toward efficient and stable cesium lead halide perovskite-based solar cells, *Adv. Sci.*, 2018, **5**, 1800509.

101 Y. Yuan and J. Huang, Ion migration in organometal trihalide perovskite and its impact on photovoltaic efficiency and stability, *Acc. Chem. Res.*, 2016, **49**, 286–293.

102 Y. Yuan, J. Chae, Y. Shao, Q. Wang, Z. Xiao, A. Centrone and J. Huang, Photovoltaic switching mechanism in lateral structure hybrid perovskite solar cells, *Adv. Energy Mater.*, 2015, **5**, 1500615.

103 C. Eames, J. M. Frost, P. R. F. Barnes, B. C. O'Regan, A. Walsh and M. S. Islam, Ionic transport in hybrid lead iodide perovskite solar cells, *Nat. Commun.*, 2015, **6**, 7497.

104 S. Chen, X. Wen, R. Sheng, S. Huang, X. Deng, M. A. Green and A. Ho-Baillie, Mobile ion induced slow carrier dynamics in organic–inorganic perovskite $CH_3NH_3PbBr_3$, *ACS Appl. Mater. Interfaces*, 2016, **8**, 5351–5357.

105 J. Haruyama, K. Sodeyama, L. Han and Y. Tateyama, First-principles study of ion diffusion in perovskite solar cell sensitizers, *J. Am. Chem. Soc.*, 2015, **137**, 10048–10051.

106 B. M. D. Puscher, M. F. Aygüler, P. Docampo and R. D. Costa, Unveiling the dynamic processes in hybrid lead bromide perovskite nanoparticle thin film devices, *Adv. Energy Mater.*, 2017, **7**, 1602283.

107 E. T. Hoke, D. J. Slotcavage, E. R. Dohner, A. R. Bowring, H. I. Karunadasa and M. D. McGehee, Reversible photo-induced trap formation in mixed-halide hybrid perovskites for photovoltaics, *Chem. Sci.*, 2015, **6**, 613–617.

108 Y. Deng, Z. Xiao and J. Huang, Light-induced self-poling effect on organometal trihalide perovskite solar cells for increased device efficiency and stability, *Adv. Energy Mater.*, 2015, **5**, 1500721.

109 P. Calado, A. M. Telford, D. Bryant, X. Li, J. Nelson, B. C. O'Regan and P. R. F. Barnes, Evidence for ion migration in hybrid perovskite solar cells with minimal hysteresis, *Nat. Commun.*, 2016, **7**, 13831.

110 Z. Xiao, Y. Yuan, Y. Shao, Q. Wang, Q. Dong, C. Bi, P. Sharma, A. Gruverman and J. Huang,

Giant switchable photovoltaic effect in organometal trihalide perovskite devices, *Nat Mater*, 2015, **14**, 193–198.

111 J. Burschka, N. Pellet, S.-J. Moon, R. Humphry-Baker, P. Gao, M. K. Nazeeruddin, M. Grätzel and M. Gratzel, Sequential deposition as a route to high-performance perovskite-sensitized solar cells, *Nature*, 2013, **499**, 316–320.

112 Q. Chen, H. Zhou, Z. Hong, S. Luo, H. S. Duan, H. H. Wang, Y. Liu, G. Li and Y. Yang, Planar heterojunction perovskite solar cells via vapor-assisted solution process, *J. Am. Chem. Soc.*, 2014, **136**, 622–625.

113 M. H. Kumar, N. Yantara, S. Dharani, M. Graetzel, P. P. Boix and N. Mathews, Flexible, low-temperature, solution processed ZnO-based perovskite solid state solar cells, *Chem. Commun.*, 2013, **49**, 11089–11091.

114 S. S. Shin, W. S. Yang, J. H. Noh, J. H. Suk, N. J. Jeon, J. H. Park, J. S. Kim, W. M. Seong and S. Il Seok, High-performance flexible perovskite solar cells exploiting Zn_2SnO_4 prepared in solution below 100 °C, *Nat. Commun.*, 2015, **6**, 7410.

115 Y. Ren, I. W. H. Oswald, X. Wang, G. T. McCandless and J. Y. Chan, Orientation of organic cations in hybrid inorganic-organic perovskite $CH_3NH_3PbI_3$ from subatomic resolution single crystal neutron diffraction structural studies, *Cryst. Growth Des.*, 2016, **16**, 2945–2951.

116 K. Druzbicki, R. S. Pinna, S. Rudić, M. Jura, G. Gorini and F. Fernandez-Alonso, Unexpected cation dynamics in the low-temperature phase of methylammonium lead iodide: the need for improved models, *J. Phys. Chem. Lett.*, 2016, **7**, 4701–4709.

117 M. T. Weller, O. J. Weber, J. M. Frost and A. Walsh, Cubic perovskite structure of black formamidinium lead iodide, *α*-$[HC(NH_2)_2]PbI_3$, at 298 K, *J. Phys. Chem. Lett.*, 2015, **6**, 3209–3212.

118 M. T. Weller, O. J. Weber, P. F. Henry, A. M. Di Pumpo and T. C. Hansen, Complete structure and cation orientation in the perovskite photovoltaic methylammonium lead iodide between 100 and 352 K, *Chem. Commun.*, 2015, **51**, 4180–4183.

119 A. A. Bakulin, O. Selig, H. J. Bakker, Y. L. A. Rezus, C. Mueller, T. Glaser, R. Lovrincic, Z. Sun, Z. Chen, A. Walsh, J. M. Frost and T. L. C. Jansen, Real-time observation of organic cation reorientation in methylammonium lead iodide perovskites, *J. Phys. Chem. Lett.*, 2015, **6**, 3663–3669.

120 J. Even, M. Carignano and C. Katan, Molecular disorder and translation/rotation coupling in the plastic crystal phase of hybrid perovskites, *Nanoscale*, 2016, **8**, 6222–6236.

121 D. Yuan, A. Gorka, M. Xu, Z. Wang and L. Liao, Inverted planar $NH_2C{=}NH_2PbI_3$ perovskite solar cells with 13.56% efficiency via low temperature processing, *Phys. Chem. Chem. Phys.*, 2015, **17**, 19745–19750.

122 N. Onoda-Yamamuro, T. Matsuo and H. Suga, Calorimetric and IR spectroscopic studies of phase transitions in methylammonium trihalogenoplumbates (II), *J. Phys. Chem. Solids*, 1990, **51**, 1383–1395.

123 I. P. Swainson, C. Stock, S. F. Parker, L. Van Eijck, M. Russina and J. W. Taylor, From soft harmonic phonons to fast relaxational dynamics in $CH_3NH_3PbBr_3$, *Phys. Rev. B*, 2015, **92**, 100303.

124 A. M. A. Leguy, J. M. Frost, A. P. McMahon, V. G. Sakai, W. Kochelmann, C. Law, X. Li, F. Foglia, A. Walsh, B. C. O'Regan, J. Nelson, J. T. Cabral and P. R. F. Barnes, The dynamics of methylammonium ions in hybrid organic–inorganic perovskite solar cells, *Nat. Commun.*, 2015, **6**, 7124.

125 B. J. Foley, D. L. Marlowe, K. Sun, W. A. Saidi, L. Scudiero, M. C. Gupta and J. J. Choi, Temperature dependent energy levels of methylammonium lead iodide perovskite, *Appl. Phys. Lett.*, 2015, **106**, 243904.

126 P. An and S. Thomson, Observing phase transitions in a halide perovskite using temperature dependent photoluminescence spectroscopy observing phase transitions in a halide perovskite

using temperature dependent photoluminescence spectroscopy, *Edinburgh Instruments*, 2018, 1–4.

127 O. Selig, A. Sadhanala, C. Müller, R. Lovrincic, Z. Chen, Y. L. A. Rezus, J. M. Frost, T. L. C. Jansen and A. A. Bakulin, Organic cation rotation and immobilization in pure and mixed methylammonium lead-halide perovskites, *J. Am. Chem. Soc.*, 2017, **139**, 4068–4074.

128 J. H. Noh, S. H. Im, J. H. Heo, T. N. Mandal and S. Il Seok, Chemical management for colorful, efficient, and stable inorganic–organic hybrid nanostructured solar cells, *Nano Lett.*, 2013, **13**, 1764–1769.

129 R. Soltani, B. M. D. Puscher, A. A. Katbab, I. Levchuk, N. Kazerouni, N. Gasparini, N. Camaioni, A. Osvet, M. Batentschuk, R. H. Fink, D. M. Guldi and T. Ameri, Improved charge carrier dynamics in polymer/perovskite nanocrystal based hybrid ternary solar cells, *Phys. Chem. Chem. Phys.*, 2018, **20**, 23674–23683.

130 I. Poli, X. Liang, R. Baker, S. Eslava and P. J. Cameron, Enhancing the hydrophobicity of perovskite solar cells using C18 capped $CH_3NH_3PbI_3$ nanocrystals, *J. Mater. Chem. C*, 2018, **6**, 7149–7156.

131 F. Zhang, H. Zhong, C. Chen, X. Wu, X. Hu and H. Huang, Brightly luminescent and color-tunable colloidal $CH_3NH_3PbX_3$ (X = Br ,I ,Cl) quantum dots: potential alternatives for display technology, *ACS Nano*, 2015, **3**, 4533–4542.

132 F. Brivio, K. T. Butler, A. Walsh and M. Van Schilfgaarde, Relativistic quasiparticle self-consistent electronic structure of hybrid halide perovskite photovoltaic absorbers, *Phys. Rev. B*, 2014, **89**, 155204.

133 A. Amat, E. Mosconi, E. Ronca, C. Quarti, P. Umari, M. K. Nazeeruddin, M. Grätzel and F. De Angelis, Cation-induced band-gap tuning in organohalide perovskites: interplay of spin-orbit coupling and octahedra tilting, *Nano Lett.*, 2014, **14**, 3608–3616.

134 K. G. Stamplecoskie, J. S. Manser and P. V. Kamat, Dual nature of the excited state in organic-inorganic lead halide perovskites, *Energy Environ. Sci.*, 2015, **8**, 208–215.

135 J. A. Christians, J. S. Manser and P. V. Kamat, Multifaceted excited state of $CH_3NH_3PbI_3$. Charge separation, recombination, and trapping, *J. Phys. Chem. Lett.*, 2015, **6**, 2086–2095.

136 G. Xing, N. Mathews, S. Sun, S. S. Lim, Y. M. Lam, M. Gratzel, S. Mhaisalkar and T. C. Sum, Long-range balanced electron- and hole-transport lengths in organic-inorganic $CH_3NH_3PbI_3$, *Science*, 2013, **342**, 344–347.

137 J. S. Manser and P. V Kamat, Band filling with free charge carriers in organometal halide perovskites, *Nat. Photonics*, 2014, **8**, 737–743.

138 L. Wang, C. Mccleese, A. Kovalsky, Y. Zhao and C. Burda, Femtosecond time-resolved transient absorption spectroscopy of $CH_3NH_3PbI_3$ perovskite films: evidence for passivation effect of PbI_2, *J. Am. Chem. Soc.*, 2014, **136**, 12205–12208.

139 H. Kawai, G. Giorgi, A. Marini and K. Yamashita, The mechanism of slow hot-hole cooling in lead-iodide perovskite: first-principles calculation on carrier lifetime from electron-phonon interaction, *Nano Lett.*, 2015, **15**, 3103–3108.

140 N. Kitazawa, Y. Watanabe and Y. Nakamura, Optical properties of $CH_3NH_3PbX_3$ (X = halogen) and their mixed-halide crystals, *J. Mater. Sci.*, 2002, **37**, 3585–3587.

141 K. Tanaka, T. Takahashi, T. Ban, T. Kondo, K. Uchida and N. Miura, Comparative study on the excitons in lead-halide-based perovskite-type crystals $CH_3NH_3PbBr_3$ $CH_3NH_3PbI_3$, *Solid State Commun.*, 2003, **127**, 619–623.

142 M. Park, A. J. Neukirch, S. E. Reyes-Lillo, M. Lai, S. R. Ellis, D. Dietze, J. B. Neaton, P. Yang, S. Tretiak and R. A. Mathies, Excited-state vibrational dynamics toward the polaron in methylammonium lead iodide perovskite, *Nat. Commun.*, 2018, **9**, 2525.

143 M. Sotoodeh, A. H. Khalid and A. A. Rezazadeh, Empirical low-field mobility model for III-V compounds applicable in device simulation codes, *J. Appl. Phys.*, 2000, **87**, 2890–2900.

144 S. S. Li and W. R. Thurber, The dopant density and temperature dependence of electron mobility and resistivity in n-type silicon, *Solid. State. Electron.*, 1977, **20**, 609–616.

145 D. Niesner, H. Zhu, K. Miyata, P. P. Joshi, T. J. S. Evans, B. J. Kudisch, M. T. Trinh, M. Marks and X. Y. Zhu, Persistent energetic electrons in methylammonium lead iodide perovskite thin films, *J. Am. Chem. Soc.*, 2016, **138**, 15717–15726.

146 H. Zhu, K. Miyata, Y. Fu, J. Wang, P. P. Joshi, D. Niesner, K. W. Williams, S. Jin and X.-Y. Zhu, Screening in crystalline liquids protects energetic carriers in hybrid perovskites, *Science*, 2016, **353**, 1409–1413.

147 G. J. Hedley, C. Quarti, J. Harwell, O. V Prezhdo, D. Beljonne and I. D. W. Samuel, Hot-hole cooling controls the initial ultrafast relaxation in methylammonium lead iodide perovskite, *Sci. Rep.*, 2018, **8**, 8115.

148 M. E. Madjet, G. R. Berdiyorov, F. El-Mellouhi, F. H. Alharbi, A. V Akimov and S. Kais, Cation effect on hot carrier cooling in halide perovskite materials, *J. Phys. Chem. Lett.*, 2017, **8**, 4439–4445.

149 K. Miyata, D. Meggiolaro, M. T. Trinh, P. P. Joshi, E. Mosconi, S. C. Jones, F. De Angelis and X.-Y. Zhu, Large polarons in lead halide perovskites, *Sci. Adv.*, 2017, **3**, e1701217.

150 K. T. Munson, E. R. Kennehan, G. S. Doucette and J. B. Asbury, Dynamic disorder dominates delocalization, transport, and recombination in halide perovskites, *Chem*, 2018, **4**, 2826–2843.

151 A. Walsh, D. O. Scanlon, S. Chen, X. G. Gong and S.-H. Wei, Self-regulation mechanism for charged point defects in hybrid halide perovskites, *Angew. Chem. Int. Ed.*, 2015, **54**, 1791–1794.

152 D. Yang, W. Ming, H. Shi, L. Zhang and M. H. Du, Fast diffusion of native defects and impurities in perovskite solar cell material $CH_3NH_3PbI_3$, *Chem. Mater.*, 2016, **28**, 4349–4357.

153 J. L. Minns, P. Zajdel, D. Chernyshov, W. Van Beek and M. A. Green, Structure and interstitial iodide migration in hybrid perovskite methylammonium lead iodide, *Nat. Commun.*, 2017, **8**, 15152.

154 Y. Shao, Y. Fang, T. Li, Q. Wang, Q. Dong, Y. Deng, Y. Yuan, H. Wei, M. Wang, A. Gruverman, J. Shield and J. Huang, Grain boundary dominated ion migration in polycrystalline organic-inorganic halide perovskite films, *Energy Environ. Sci.*, 2016, **9**, 1752–1759.

155 Z. Xiao, Q. Dong, C. Bi, Y. Shao, Y. Yuan and J. Huang, Solvent annealing of perovskite-induced crystal growth for photovoltaic-device efficiency enhancement, *Adv. Mater.*, 2014, **26**, 6503–6509.

156 H. S. Kim and N. G. Park, Parameters affecting I-V hysteresis of $CH_3NH_3PbI_3$ perovskite solar cells: effects of perovskite crystal size and mesoporous TiO_2 layer, *J. Phys. Chem. Lett.*, 2014, **5**, 2927–2934.

157 Y. Shao, Z. Xiao, C. Bi, Y. Yuan and J. Huang, Origin and elimination of photocurrent hysteresis by fullerene passivation in $CH_3NH_3PbI_3$ planar heterojunction solar cells, *Nat. Commun.*, 2014, **5**, 5784.

158 E. L. Unger, E. T. Hoke, C. D. Bailie, W. H. Nguyen, A. R. Bowring, T. Heumuller, M. G. Christoforo and M. D. McGehee, Hysteresis and transient behavior in current-voltage measurements of hybrid-perovskite absorber solar cells, *Energy Environ. Sci.*, 2014, **7**, 3690–3698.

159 W. Tress, N. Marinova, T. Moehl, S. M. Zakeeruddin, M. K. Nazeeruddin and M. Grätzel, Understanding the rate-dependent J–V hysteresis, slow time component, and aging in $CH_3NH_3PbI_3$ perovskite solar cells: the role of a compensated electric field, *Energy Environ. Sci.*, 2015, **8**, 995–1004.

160 H. J. Snaith, A. Abate, J. M. Ball, G. E. Eperon, T. Leijtens, N. K. Noel, S. D. Stranks, J. T. W. Wang, K. Wojciechowski and W. Zhang, Anomalous hysteresis in perovskite solar cells, *J. Phys. Chem. Lett.*, 2014, **5**, 1511–1515.

161 X. Deng, X. Wen, J. Zheng, T. Young, C. F. J. Lau, J. Kim, M. Green, S. Huang and A. Ho-Baillie,

Dynamic study of the light soaking effect on perovskite solar cells by in-situ photoluminescence microscopy, *Nano Energy*, 2018, **46**, 356–364.

162 C. Zhao, B. Chen, X. Qiao, L. Luan, K. Lu and B. Hu, Revealing underlying processes involved in light soaking effects and hysteresis phenomena in perovskite solar cells, *Adv. Energy Mater.*, 2015, **5**, 1500279.

163 B. Chen, M. Yang, X. Zheng, C. Wu, W. Li, Y. Yan, J. Bisquert, G. Garcia-Belmonte, K. Zhu and S. Priya, Impact of capacitive effect and ion migration on the hysteretic behavior of perovskite solar cells, *J. Phys. Chem. Lett.*, 2015, **6**, 4693–4700.

164 G. A. Nemnes, C. Besleaga, A. G. Tomulescu, A. Palici, L. Pintilie, A. Manolescu and I. Pintilie, How measurement protocols influence the dynamic J-V characteristics of perovskite solar cells: theory and experiment, *Sol. Energy*, 2018, **173**, 976–983.

165 S. M. Vorpahl, R. Giridharagopal, G. E. Eperon, I. M. Hermes, S. A. L. Weber and D. S. Ginger, Orientation of ferroelectric domains and disappearance upon heating methylammonium lead triiodide perovskite from tetragonal to cubic phase, *ACS Appl. Energy Mater.*, 2018, **1**, 1534–1539.

166 F. Panzer, C. Li, T. Meier, A. Köhler and S. Huettner, Impact of structural dynamics on the optical properties of methylammonium lead iodide perovskites, *Adv. Energy Mater.*, 2017, **7**, 1700286.

167 E. J. Juarez-Perez, R. S. Sanchez, L. Badia, G. Garcia-Belmonte, Y. S. Kang, I. Mora-Sero and J. Bisquert, Photoinduced giant dielectric constant in lead halide perovskite solar cells, *J. Phys. Chem. Lett.*, 2014, **5**, 2390–2394.

168 R. D. Costa, E. Ortí, H. J. Bolink, F. Monti, G. Accorsi and N. Armaroli, Luminescent ionic transition-metal complexes for light-emitting electrochemical cells, *Angew. Chem. Int. Ed.*, 2012, **51**, 8178–8211.

169 S. Tang and L. Edman, Light-emitting electrochemical cells: a review on recent progress, *Top. Curr. Chem.*, 2016, **374**, 40.

170 S. B. Meier, D. Tordera, A. Pertegás, C. Roldán-Carmona, E. Ortí and H. J. Bolink, Light-emitting electrochemical cells: Recent progress and future prospects, *Mater. Today*, 2014, **17**, 217–223.

171 A. Munar, A. Sandström, S. Tang and L. Edman, Shedding light on the operation of polymer light-emitting electrochemical cells using impedance spectroscopy, *Adv. Funct. Mater.*, 2012, **22**, 1511–1517.

172 S. van Reenen, R. A. J. Janssen and M. Kemerink, Dynamic processes in sandwich polymer light-emitting electrochemical cells, *Adv. Funct. Mater.*, 2012, **22**, 4547–4556.

173 S. B. Meier, D. Hartmann, A. Winnacker and W. Sarfert, The dynamic behavior of thin-film ionic transition metal complex-based light-emitting electrochemical cells, *J. Appl. Phys.*, 2014, **116**, 104504.

174 H. R. Byun, D. Y. Park, H. M. Oh, G. Namkoong and M. S. Jeong, Light soaking phenomena in organic-inorganic mixed halide perovskite single crystals, *ACS Photonics*, 2017, **4**, 2813–2820.

175 M. Saliba, S. Orlandi, T. Matsui, S. Aghazada, M. Cavazzini, J.-P. Correa-Baena, P. Gao, R. Scopelliti, E. Mosconi, K.-H. Dahmen, F. De Angelis, A. Abate, A. Hagfeldt, G. Pozzi, M. Graetzel and M. K. Nazeeruddin, A molecularly engineered hole-transporting material for efficient perovskite solar cells, *Nat. Energy*, 2016, **1**, 15017.

176 B. Roose, J.-P. Correa-Baena, K. C. Gödel, M. Grätzel, A. Hagfeldt, U. Steiner and A. Abate, Mesoporous SnO_2 electron selective contact enables UV-stable perovskite solar cells, *Nano Energy*, 2016, **30**, 517–522.

177 P. Zhang, J. Wu, T. Zhang, Y. Wang, D. Liu, H. Chen, L. Ji, C. Liu, W. Ahmad, Z. D. Chen and S. Li, Perovskite solar cells with ZnO electron-transporting materials, *Adv. Mater.*, 2018, **30**, 1703737.

178 K. Mahmood, A. Khalid, S. W. Ahmad and M. T. Mehran, Indium-doped ZnO mesoporous nanofibers as efficient electron transporting materials for perovskite solar cells, *Surf. Coatings*

Technol., 2018, **352**, 231–237.

179 Y. Hou, C. Xie, V. V. Radmilovic, B. Puscher, M. Wu, T. Heumüller, A. Karl, N. Li, X. Tang, W. Meng, S. Chen, A. Osvet, D. Guldi, E. Spiecker, V. R. Radmilović and C. J. Brabec, Assembling mesoscale-structured organic interfaces in perovskite photovoltaics, *Adv. Mater.*, 2019, **31**, 1806516.

180 Y. Hou, C. O. R. Quiroz, S. Scheiner, W. Chen, T. Stubhan, A. Hirsch, M. Halik and C. J. Brabec, Low-temperature and hysteresis-free electron-transporting layers for efficient, regular, and planar structure perovskite solar cells, *Adv. Energy Mater.*, 2015, **5**, 1501056.

181 L.-L. Deng, S.-Y. Xie and F. Gao, Fullerene-based materials for photovoltaic applications: toward efficient, hysteresis-free, and stable perovskite solar cells, *Adv. Electron. Mater.*, 2018, **4**, 1700435.

182 K.-C. Wang, J.-Y. Jeng, P.-S. Shen, Y.-C. Chang, E. W.-G. Diau, C.-H. Tsai, T.-Y. Chao, H.-C. Hsu, P.-Y. Lin, P. Chen, T.-F. Guo and T.-C. Wen, P-type mesoscopic nickel oxide/organometallic perovskite heterojunction solar cells, *Sci. Rep.*, 2015, **4**, 4756.

183 N. F. Montcada, J. M. Marín-Beloqui, W. Cambarau, J. Jiménez-López, L. Cabau, K. T. Cho, M. K. Nazeeruddin and E. Palomares, Analysis of photoinduced carrier recombination kinetics in flat and mesoporous lead perovskite solar cells, *ACS Energy Lett.*, 2017, **2**, 182–187.

184 J. Burschka, A. Dualeh, F. Kessler, E. Baranoff, N. L. Cevey-Ha, C. Yi, M. K. Nazeeruddin and M. Grätzel, Tris(2-(1H-pyrazol-1-yl)pyridine)cobalt(III) as p-type dopant for organic semiconductors and its application in highly efficient solid-state dye-sensitized solar cells, *J. Am. Chem. Soc.*, 2011, **133**, 18042–18045.

185 W. H. Nguyen, C. D. Bailie, E. L. Unger and M. D. McGehee, Enhancing the hole-conductivity of spiro-OMeTAD without oxygen or lithium salts by using spiro(TFSI)$_2$ in perovskite and dye-sensitized solar cells, *J. Am. Chem. Soc.*, 2014, **136**, 10996–11001.

186 Z. Hawash, L. K. Ono and Y. Qi, Recent advances in spiro-MeOTAD hole transport material and its applications in organic-inorganic halide perovskite solar cells, *Adv. Mater. Interfaces*, 2018, **5**, 1700623.

187 S. Ameen, M. A. Rub, S. A. Kosa, K. A. Alamry, M. S. Akhtar, H.-S. Shin, H.-K. Seo, A. M. Asiri and M. K. Nazeeruddin, Perovskite solar cells: influence of hole transporting materials on power conversion efficiency, *ChemSusChem*, 2016, **9**, 10–27.

188 D. Bi, L. Yang, G. Boschloo, A. Hagfeldt and E. M. J. Johansson, Effect of different hole transport materials on recombination in $CH_3NH_3PbI_3$ perovskite-sensitized mesoscopic solar cells, *J. Phys. Chem. Lett.*, 2013, **4**, 1532–1536.

189 J. Jiménez-López, W. Cambarau, L. Cabau and E. Palomares, Charge injection, carriers recombination and HOMO energy level relationship in perovskite solar cells, *Sci. Rep.*, 2017, **7**, 6101.

190 Y. Hou, X. Du, S. Scheiner, D. P. McMeekin, Z. Wang, N. Li, M. S. Killian, H. Chen, M. Richter, I. Levchuk, N. Schrenker, E. Spiecker, T. Stubhan, N. A. Luechinger, A. Hirsch, P. Schmuki, H.-P. Steinrück, R. H. Fink, M. Halik, H. J. Snaith and C. J. Brabec, A generic interface to reduce the efficiency-stability-cost gap of perovskite solar cells, *Science*, 2017, **358**, 1192–1197.

191 J. A. Christians, R. C. M. Fung and P. V Kamat, An inorganic hole conductor for organo-lead halide perovskite solar cells. Improved hole conductivity with copper iodide, *J. Am. Chem. Soc.*, 2014, **136**, 758–764.

192 M.-H. Li, P.-S. Shen, K.-C. Wang, T.-F. Guo and P. Chen, Inorganic p-type contact materials for perovskite-based solar cells, *J. Mater. Chem. A*, 2015, **3**, 9011–9019.

193 P. Tiwana, P. Docampo, M. B. Johnston, H. J. Snaith and L. M. Herz, Electron mobility and injection dynamics in mesoporous ZnO, SnO_2, and TiO_2 films used in dye-sensitized solar cells, *ACS Nano*, 2011, **5**, 5158–5166.

194 J. M. Cha, J. W. Lee, D. Y. Son, H. S. Kim, I. H. Jang and N. G. Park, Mesoscopic perovskite solar cells with an admixture of nanocrystalline TiO_2 and Al_2O_3: role of interconnectivity of TiO_2

in charge collection, *Nanoscale*, 2016, **8**, 6341–6351.

195 A. Marchioro, J. Teuscher, D. Friedrich, M. Kunst, R. van de Krol, T. Moehl, M. Grätzel and J.-E. Moser, Unravelling the mechanism of photoinduced charge transfer processes in lead iodide perovskite solar cells, *Nat. Photonics*, 2014, **8**, 250–255.

196 J. Bisquert, Chemical capacitance of nanostructured semiconductors: Its origin and significance for nanocomposite solar cells, *Phys. Chem. Chem. Phys.*, 2003, **5**, 5360–5364.

197 Y. Shao, Y. Yuan and J. Huang, Correlation of energy disorder and open-circuit voltage in hybrid perovskite solar cells, *Nat. Energy*, 2016, **1**, 15001.

198 G. E. Eperon, V. M. Burlakov, P. Docampo, A. Goriely and H. J. Snaith, Morphological control for high performance, solution-processed planar heterojunction perovskite solar cells, *Adv. Funct. Mater.*, 2014, **24**, 151–157.

199 J. Y. Jeng, K. C. Chen, T. Y. Chiang, P. Y. Lin, T. Da Tsai, Y. C. Chang, T. F. Guo, P. Chen, T. C. Wen and Y. J. Hsu, Nickel oxide electrode interlayer in $CH_3NH_3PbI_3$ perovskite/PCBM planar-heterojunction hybrid solar cells, *Adv. Mater.*, 2014, **26**, 4107–4113.

200 O. Malinkiewicz, A. Yella, Y. H. Lee, G. M. Espallargas, M. Graetzel, M. K. Nazeeruddin and H. J. Bolink, Perovskite solar cells employing organic charge-transport layers, *Nat. Photonics*, 2014, **8**, 128–132.

201 P. Docampo, J. M. Ball, M. Darwich, G. E. Eperon and H. J. Snaith, Efficient organometal trihalide perovskite planar-heterojunction solar cells on flexible polymer substrates, *Nat. Commun.*, 2013, **4**, 2761.

202 C. Tao, S. Neutzner, L. Colella, S. Marras, A. R. Srimath Kandada, M. Gandini, M. De Bastiani, G. Pace, L. Manna, M. Caironi, C. Bertarelli and A. Petrozza, 17.6% stabilized efficiency in low-temperature processed planar perovskite solar cells, *Energy Environ. Sci.*, 2015, **8**, 2365–2370.

203 P. Piatkowski, B. Cohen, F. Javier Ramos, M. Di Nunzio, M. K. Nazeeruddin, M. Grätzel, S. Ahmad and A. Douhal, Direct monitoring of ultrafast electron and hole dynamics in perovskite solar cells, *Phys. Chem. Chem. Phys.*, 2015, **17**, 14674–14684.

204 J. C. Brauer, Y. H. Lee, M. K. Nazeeruddin and N. Banerji, Ultrafast charge carrier dynamics in $CH_3NH_3PbI_3$: evidence for hot hole injection into spiro-OMeTAD, *J. Mater. Chem. C*, 2016, **4**, 5922–5931.

205 J. C. Brauer, Y. H. Lee, M. K. Nazeeruddin and N. Banerji, Charge transfer dynamics from organometal halide perovskite to polymeric hole transport materials in hybrid solar cells, *J. Phys. Chem. Lett.*, 2015, **6**, 3675–3681.

206 Y. C. Ho, M. N. F. Hoque, E. Stoneham, J. Warzywoda, T. Dallas and Z. Fan, Reduction of oxygen vacancy related traps in TiO_2 and the impacts on hybrid perovskite solar cells, *J. Phys. Chem. C*, 2017, **121**, 23939–23946.

207 J. R. Klein, M. Scholz, K. Oum and T. Lenzer, Quantifying ultrafast charge carrier injection from methylammonium lead iodide into the hole-transport material H101 and mesoporous TiO_2 using Vis-NIR transient absorption, *Phys. Chem. Chem. Phys.*, 2017, **19**, 17952–17959.

208 S. D. Stranks, V. M. Burlakov, T. Leijtens, J. M. Ball, A. Goriely and H. J. Snaith, Recombination kinetics in organic-inorganic perovskites: excitons, free charge, and subgap states, *Phys. Rev. Appl.*, 2014, **2**, 034007.

209 M. Adachi, M. Sakamoto, J. Jiu, Y. Ogata and S. Isoda, Determination of parameters of electron transport in dye-sensitized solar cells using electrochemical impedance spectroscopy, *J. Phys. Chem. B*, 2006, **110**, 13872–13880.

210 J. Bisquert, L. Bertoluzzi, I. Mora-Sero and G. Garcia-Belmonte, Theory of impedance and capacitance spectroscopy of solar cells with dielectric relaxation, drift-diffusion transport, and recombination, *J. Phys. Chem. C*, 2014, **118**, 18983–18991.

211 H. Kim, I. Mora-Sero, V. Gonzalez-Pedro, F. Fabregat-Santiago, E. J. Juarez-Perez, N. Park and J. Bisquert, Mechanism of carrier accumulation in perovskite thin-absorber solar cells, *Nat.*

Commun., 2013, **4**, 2242.

212 G. J. Brug, A. L. G. van den Eeden, M. Sluyters-Rehbach and J. H. Sluyters, The analysis of electrode impedances complicated by the presence of a constant phase element, *J. Electroanal. Chem.*, 1984, **176**, 275–295.

213 N. Jürgensen, J. Zimmermann, A. J. Morfa and G. Hernandez-Sosa, Biodegradable polycaprolactone as ion solvating polymer for solution-processed light-emitting electrochemical cells, *Sci. Rep.*, 2016, **6**, 36643.

214 C. Ruckebusch, M. Sliwa, P. Pernot, A. de Juan and R. Tauler, Comprehensive data analysis of femtosecond transient absorption spectra: a review, *J. Photochem. Photobiol. C Photochem. Rev.*, 2012, **13**, 1–27.

215 U. Megerle, I. Pugliesi, C. Schriever, C. F. Sailer and E. Riedle, Sub-50 fs broadband absorption spectroscopy with tunable excitation: putting the analysis of ultrafast molecular dynamics on solid ground, *Appl. Phys. B*, 2009, **96**, 215–231.

216 O. Flender, J. R. Klein, T. Lenzer and K. Oum, Ultrafast photoinduced dynamics of the organolead trihalide perovskite $CH_3NH_3PbI_3$ on mesoporous TiO_2 scaffolds in the 320–920 nm range, *Phys. Chem. Chem. Phys.*, 2015, **17**, 19238–19246.

217 M. B. Price, J. Butkus, T. C. Jellicoe, A. Sadhanala, A. Briane, J. E. Halpert, K. Broch, J. M. Hodgkiss, R. H. Friend and F. Deschler, Hot-carrier cooling and photoinduced refractive index changes in organic–inorganic lead halide perovskites, *Nat. Commun.*, 2015, **6**, 8420.

218 S. Narra, C. Chung, E. W. Diau and S. Shigeto, Simultaneous observation of an intraband transition and distinct transient species in the infrared region for perovskite solar cells, *J. Phys. Chem. Lett.*, 2016, **7**, 2450–2455.

219 Y. Zhai, C. X. Sheng, C. Zhang and Z. V. Vardeny, Ultrafast spectroscopy of photoexcitations in organometal trihalide perovskites, *Adv. Funct. Mater.*, 2016, **26**, 1617–1627.

220 Z. Guo, Y. Wan, M. Yang, J. Snaider, K. Zhu and L. Huang, Long-range hot-carrier transport in hybrid perovskites visualized by ultrafast microscopy, *Science*, 2017, **356**, 59–62.

221 L. M. Herz, Charge-carrier dynamics in organic-inorganic metal halide perovskites, *Annu. Rev. Phys. Chem.*, 2016, **67**, 65–89.

222 J. J. Snellenburg, S. P. Laptenok, R. Seger, K. M. Mullen and I. H. M. van Stokkum, Glotaran: a Java-based graphical user interface for the R package TIMP, *J. Stat. Softw.*, 2012, **49**, 1–22.

223 M. Pazoki, U. B. Cappel, E. M. J. Johansson, A. Hagfeldt and G. Boschloo, Characterization techniques for dye-sensitized solar cells, *Energy Environ. Sci.*, 2017, **10**, 672–709.

224 E. Bi, H. Chen, F. Xie, Y. Wu, W. Chen, Y. Su, A. Islam, M. Grätzel, X. Yang and L. Han, Diffusion engineering of ions and charge carriers for stable efficient perovskite solar cells, *Nat. Commun.*, 2017, **8**, 15330.

225 H. Kim, L. Zhao, J. S. Price, A. J. Grede, K. Roh, A. N. Brigeman, M. Lopez, B. P. Rand and N. C. Giebink, Hybrid perovskite light emitting diodes under intense electrical excitation, *Nat. Commun.*, 2018, **9**, 4893.

226 R. Doshi, J. L. Routbort and C. B. Alcock, Diffusion in mixed conducting oxides: a review, *Defect Diffus. Forum*, 1995, **127**–**128**, 39–58.

227 X. Deng, X. Wen, C. F. J. Lau, T. Young, J. Yun, M. A. Green, S. Huang and A. W. Y. Ho-Baillie, Electric field induced reversible and irreversible photoluminescence responses in methylammonium lead iodide perovskite, *J. Mater. Chem. C*, 2016, **4**, 9060–9068.

228 H.-C. Su and J.-H. Hsu, Improving the carrier balance of light-emitting electrochemical cells based on ionic transition metal complexes, *Dalt. Trans.*, 2015, **44**, 8330–8345.

229 F. AlTal and J. Gao, Long-term testing of polymer light-emitting electrochemical cells: reversible doping and black spots, *Org. Electron.*, 2015, **18**, 1–7.

230 S. B. Meier, D. Hartmann, D. Tordera, H. J. Bolink, A. Winnacker and W. Sarfert, Dynamic doping

and degradation in sandwich-type light-emitting electrochemical cells, *Phys. Chem. Chem. Phys.*, 2012, **14**, 10886–10890.

231 Q. Pei, Yang, G. Yu, C. Zhang and A. J. Heeger, Polymer light-emitting electrochemical cells: in situ formation of a light-emitting p−n junction, *J. Am. Chem. Soc.*, 1996, **118**, 3922–3929.

232 J. A. Manzanares, H. Reiss and A. J. Heeger, Polymer light-emitting electrochemical cells: a theoretical study of junction formation under steady-state conditions, *J. Phys. Chem. B*, 1998, **102**, 4327–4336.

233 Z. He, B. Xiao, F. Liu, H. Wu, Y. Yang, S. Xiao, C. Wang, T. P. Russell and Y. Cao, Single-junction polymer solar cells with high efficiency and photovoltage, *Nat. Photonics*, 2015, **9**, 174–179.

234 N. Gasparini, X. Jiao, T. Heumueller, D. Baran, G. J. Matt, S. Fladischer, E. Spiecker, H. Ade, C. J. Brabec and T. Ameri, Designing ternary blend bulk heterojunction solar cells with reduced carrier recombination and a fill factor of 77%, *Nat. Energy*, 2016, **1**, 16118.

235 M. Koppe, H.-J. Egelhaaf, E. Clodic, M. Morana, L. Lüer, A. Troeger, V. Sgobba, D. M. Guldi, T. Ameri and C. J. Brabec, Charge carrier dynamics in a ternary bulk heterojunction system consisting of P3HT, fullerene, and a low bandgap polymer, *Adv. Energy Mater.*, 2013, **3**, 949–958.

236 S. Honda, S. Yokoya, H. Ohkita, H. Benten and S. Ito, Light-harvesting mechanism in polymer/fullerene/dye ternary blends studied by transient absorption spectroscopy, *J. Phys. Chem. C*, 2011, **115**, 11306–11317.

237 J.-H. Huang, M. Velusamy, K.-C. Ho, J.-T. Lin and C.-W. Chu, A ternary cascade structure enhances the efficiency of polymer solar cells, *J. Mater. Chem.*, 2010, **20**, 2820–2825.

238 R. Soltani, A. A. Katbab, K. Schaumberger, N. Gasparini, C. J. Brabec, S. Rechberger, E. Spiecker, A. G. Alabau, A. Ruland, A. Saha, D. M. Guldi, V. Sgobba and T. Ameri, Light harvesting enhancement upon incorporating alloy structured $CdSe_xTe_{1-x}$ quantum dots in DPP:PC_{61}BM bulk heterojunction solar cells, *J. Mater. Chem. C*, 2017, **5**, 654–662.

239 H. Bronstein, Z. Chen, R. S. Ashraf, W. Zhang, J. Du, J. R. Durrant, P. Shakya Tuladhar, K. Song, S. E. Watkins, Y. Geerts, M. M. Wienk, R. A. J. Janssen, T. Anthopoulos, H. Sirringhaus, M. Heeney and I. McCulloch, Thieno[3,2-*b*]thiophene−diketopyrrolopyrrole-containing polymers for high-performance organic field-effect transistors and organic photovoltaic devices, *J. Am. Chem. Soc.*, 2011, **133**, 3272–3275.

240 B. P. Karsten, R. K. M. Bouwer, J. C. Hummelen, R. M. Williams and R. A. J. Janssen, Charge separation and (triplet) recombination in diketopyrrolopyrrole–fullerene triads, *Photochem. Photobiol. Sci.*, 2010, **9**, 1055–1065.

241 J. C. Bijleveld, V. S. Gevaerts, D. Di Nuzzo, M. Turbiez, S. C. J. Mathijssen, D. M. De Leeuw, M. M. Wienk and R. A. J. Janssen, Efficient solar cells based on an easily accessible diketopyrrolopyrrole polymer, *Adv. Mater.*, 2010, **22**, 242–246.

242 I. Levchuk, A. Osvet, X. Tang, M. Brandl, J. D. Perea, F. Hoegl, G. J. Matt, R. Hock, M. Batentschuk and C. J. Brabec, Brightly luminescent and color-tunable formamidinium lead halide perovskite $FAPbX_3$ (X = Cl, Br, I) colloidal nanocrystals, *Nano Lett.*, 2017, **17**, 2765–2770.

243 M. M. Wienk, M. Turbiez, J. Gilot and R. A. J. Janssen, Narrow-bandgap diketo-pyrrolo-pyrrole polymer solar cells: the effect of processing on the performance, *Adv. Mater.*, 2008, **20**, 2556–2560.

244 G. A. Berriman, J. L. Holdsworth, X. Zhou, W. J. Belcher and P. C. Dastoor, Molecular versus crystallite PCBM diffusion in P3HT:PCBM blends, *AIP Adv.*, 2015, **5**, 097220.

245 C. Tao, J. Van Der Velden, L. Cabau, N. F. Montcada, S. Neutzner, A. R. Srimath Kandada, S. Marras, L. Brambilla, M. Tommasini, W. Xu, R. Sorrentino, A. Perinot, M. Caironi, C. Bertarelli, E. Palomares and A. Petrozza, Fully solution-processed n-i-p-like perovskite solar cells with planar junction: how the charge extracting layer determines the open-circuit voltage, *Adv. Mater.*, 2017, **29**, 1604493.

246 B. M. Savoie, A. Rao, A. A. Bakulin, S. Gelinas, B. Movaghar, R. H. Friend, T. J. Marks and M. A. Ratner, Unequal partnership: asymmetric roles of polymeric donor and fullerene acceptor in generating free charge, *J. Am. Chem. Soc.*, 2014, **136**, 2876–2884.

247 K. Ishioka, B. G. Barker, M. Yanagida, Y. Shirai and K. Miyano, Direct observation of ultrafast hole injection from lead halide perovskite by differential transient transmission spectroscopy, *J. Phys. Chem. Lett.*, 2017, **8**, 3902–3907.

248 J. Jiménez-López, B. M. D. Puscher, W. Cambarau, R. H. Fink, E. Palomares and D. M. Guldi, Hot electron injection into semiconducting polymers in polymer based-perovskite solar cells and their fate, *Nanoscale*, submitted.

249 M. Li, S. Bhaumik, T. W. Goh, M. S. Kumar, N. Yantara, M. Grätzel, S. Mhaisalkar, N. Mathews and T. C. Sum, Slow cooling and highly efficient extraction of hot carriers in colloidal perovskite nanocrystals, *Nat. Commun.*, 2017, **8**, 14350.

250 B. S. Kalanoor, L. Gouda, R. Gottesman, S. Tirosh, E. Haltzi, A. Zaban and Y. R. Tischler, Third-order optical nonlinearities in organometallic methylammonium lead iodide perovskite thin films, *ACS Photonics*, 2016, **3**, 361–370.

9. List of abbreviations

A	Ampere
AC	Alternating current
A_g	Geometric area
C	Capacitance
C_{eff}	Effective capacitance
C_{EDL}	Electrical double layer capacitance
C_{geo}	Geometric capacitance
CB	Conduction band
CPE	Constant phase element
CPE_{EDL}	Electrical double layer constant phase element
CPE_{geo}	Geometric constant phase element
d	Distance
DC	Direct current
DSSC	Dye-sensitized solar cell
e^-	Electron
E_{Fn}	Quasi-Fermi level of electrons
E_{Fp}	Quasi-Fermi level of holes
E_g	Band-gap energy
EDL	Electrical double layer
EIS	Electrochemical impedance spectroscopy
ESA	Excited-state absorption
ETM	Electron transporting material
eV	Electron volt
f	Frequency
FF	Fill factor
fs	Femtosecond
fs-TAS	Femtosecond transient absorption spectroscopy
G	Conductance
G_{AL}	Active layer conductance
GSB	Ground state bleaching
h	Hour
HIOP	Hybrid inorganic-organic perovskite
HOMO	Highest occupied molecular orbital
HTM	Hole transporting material
I_{exc}	Excitation pulse
I_p	Probe pulse
J	Current density
J-V	Current density voltage
K	Kelvin
L	Longitudinal
L_{cab}	Cable inductance
LEC	Light emitting electrochemical cell
LED	Light emitting diode
LUMO	Lowest unoccupied molecular orbital
m	Meter
meV	Milli electron volt
min	Minute
MPP	Maximum power point
ms	Millisecond
NC	Nanocrystal
NIR	Near-infrared
nm	Nanometer
NP	Nanoparticle
O	Optical
O.D.	Optical density
P	Power
$PCBM_{compact}$	Compact layer of PCBM
$PCBM_{NPs}$	Mesoporous layer of PCBM NPs
PCE, η	Power conversion efficiency
PIA	Photoinduced absorption
PL	Photoluminescence
ps	Picosecond
PSC	Perovskite solar cell
R	Resistance
R_e	Electrical resistance
R_I	Ionic resistance
R_S	Series resistance
S	Siemens
s	Second
SAS	Species associated spectrum
SE	Stimulated emission
TCO	Transparent conducting oxide
TWh	Terawatt hours
V	Voltage
V_I	Iodide vacancy
V_{MA}	MA^+ vacancy
VB	Valence band
vis	Visible
VS	Vibration state
wt%	Percent by weight
Z	Impedance
ε_0	Permittivity in vacuum
ε_{eff}	Dielectric constant
ε_R	Permittivity in a dielectric medium
λ_{exc}	Excitation wavelength
µs	Microsecond
φ	Phase angle
Ω	Ohm
ω	Angular frequency
°C	Degree Celsius

Al	Aluminum
Au	Gold
Br	Bromine
C	Carbon
Cl	Chlorine
CPB	Cesium lead triiodide
Cs	Cesium
DPP	Diketopyrrolopyrrole
FA^+	Formadinium
FAPI	Formadinium lead triiodide
FTO	Fluorine-doped tin oxide
H	Hydrogen
I	Iodine
ITO	Indium-doped tin oxide
MA^+	Methylammonium
MAPB	Methylammonium lead tribromide
MAPI	Methylammonium lead triiodide
N	Nitrogen
P3HT	Poly(3-hexylthiophene-2,5-diyl)
Pb	Lead
PbI_2	Lead(II) iodide
PCBM	[6,6]-phenyl-C_{61}-butyric acid methyl ester
$PC_{71}BM$	[6,6]-phenyl-C_{71}-butyric acid methyl ester
PCPDTBT	Poly[2,6-(4,4-bis-(2-ethylhexyl)-4H-cyclopenta[2,1-b;3,4-b′]dithiophene)-alt-4,7(2,1,3-benzothiadiazole)]
pDPP5T-2	Diketopyrrolopyrrole–quinquethiophene
PEDOT	Poly(3,4-ethylenedioxythiophene) polystyrene sulfonate
PEN	Polythylene naphthalate
PMMA	Poly(methyl methacrylate)
PTB7	Poly[[4,8-bis[(2-ethylhexyl)oxy]benzo[1,2-b:4,5-b’]dithiophene-2,6-diyl][3-fluoro-2-[(2-ethylhexyl)carbonyl]thieno[3,4-b]thiophenediyl]]
Spiro-OMeTAD	2,2′,7,7′-tetrakis-(diphenylamino)-9,9′-spirobifluorene
TiO_2	Titanium dioxide

10. Publications

1. M. F. Aygüler, M. D. Weber, B. M. D. Puscher, D. D. Medina, P. Docampo and R. D. Costa, Light-emitting electrochemical cells based on hybrid lead halide perovskite nanoparticles, *J. Phys. Chem. C*, 2015, **119**, 12047–12054.
   DOI: 10.1021/acs.jpcc.5b02959

2. B. M. D. Puscher, M. F. Aygüler, P. Docampo and R. D. Costa, Unveiling the dynamic processes in hybrid lead bromide perovskite nanoparticle thin film devices, *Adv. Energy Mater.*, 2017, **7**, 1602283.
   DOI: 10.1002/aenm.201602283

3. M. F. Aygüler, B. M. D. Puscher, Y. Tong, T. Bein, A. S. Urban, R. D. Costa and P. Docampo, Light-emitting electrochemical cells based on inorganic metal halide perovskite nanocrystals, *J. Phys. D. Appl. Phys.*, 2018, **51**, 334001.
   DOI: 10.1088/1361-6463/aad203

4. R. Soltani‡, B. M. D. Puscher‡, A. A. Katbab, I. Levchuk, N. Kazerouni, N. Gasparini, N. Camaioni, A. Osvet, M. Batentschuk, R. H. Fink, D. M. Guldi and T. Ameri, Improved charge carrier dynamics in polymer/perovskite nanocrystal based hybrid ternary solar cells, *Phys. Chem. Chem. Phys.*, 2018, **20**, 23674-23683. // ‡ contributed equally.
   DOI: 10.1039/C8CP03743D

5. Y. Hou, C. Xie, V. V. Radmilovic, B. M. D. Puscher, M. Wu, T. Heumüller, A. Karl, N. Li, X. Tang, W. Meng, S. Chen, A. Osvet, D. Guldi, E. Spiecker, V. R. Radmilović and C. J. Brabec, Assembling mesoscale-structured organic interfaces in perovskite photovoltaics, *Adv. Mater.*, 2019, **31**, 1806516.
   DOI: 10.1002/adma.201806516

6. J. Jiménez-López‡, B. M. D. Puscher‡, W. Cambarau, R. H. Fink, E. Palomares and D. M. Guldi, Hot electron injection into semiconducting polymers in polymer based-perovskite solar cells and their fate, *Nanoscale*, 2019, **11**, 23357-23365. // ‡ contributed equally.
   DOI: 10.1039/C9NR06297A

7. J. Jiménez-López‡, B. M. D. Puscher‡, D. M. Guldi and E. Palomares, Improved carrier collection and hot electron extraction across perovskite, C_{60}, and TiO_2 interfaces, *J. Am. Chem. Soc.*, 2019, accepted. // ‡ contributed equally.
   DOI: 10.1021/jacs.9b09182

11. Author contributions and attached publications

1. B. M. D. Puscher, M. F. Aygüler, P. Docampo and R. D. Costa, Unveiling the dynamic processes in hybrid lead bromide perovskite nanoparticle thin film devices, *Adv. Energy Mater.*, 2017, **7**, 1602283.
   DOI: 10.1002/aenm.201602283

Author contribution of Bianka M. D. Puscher

Electrochemical measurements:

- Constant voltage and pulsed current measurements
- Impedance spectroscopy measurements

Data analysis:

- Analysis of constant voltage, pulsed current, and impedance measurements
- Interpretation of constant voltage, pulsed current, and impedance measurements (in cooperation with R. D. Costa)
- Discussion of the results (in cooperation with all authors)

Writing of the manuscript:

- Writing of the manuscript (in cooperation with R. D. Costa)
- Revision of the manuscript (in cooperation with all authors)
- Proofreading of the manuscript (in cooperation with all authors)

2. R. Soltani‡, B. M. D. Puscher‡, A. A. Katbab, I. Levchuk, N. Kazerouni, N. Gasparini, N. Camaioni, A. Osvet, M. Batentschuk, R. H. Fink, D. M. Guldi and T. Ameri, Improved charge carrier dynamics in polymer/perovskite nanocrystal based hybrid ternary solar cells, *Phys. Chem. Chem. Phys.*, 2018, **20**, 23674–23683. ‡ contributed equally.
DOI: 10.1039/C8CP03743D

Author contribution of Bianka M. D. Puscher

Photophysical measurements:

- fs-TAS measurements

Data analysis:

- Analysis of fs-TAS measurements
- Interpretation of fs-TAS measurements (in cooperation with D. M. Guldi)
- Discussion of the results (in cooperation with all authors)

Writing of the manuscript:

- Writing of the manuscript (in cooperation with R. Soltani)
- Revision of the manuscript (in cooperation with all authors)
- Proofreading of the manuscript (in cooperation with all authors)

3. Y. Hou, C. Xie, V. V. Radmilovic, B. M. D. Puscher, M. Wu, T. Heumüller, A. Karl, N. Li, X. Tang, W. Meng, S. Chen, A. Osvet, D. Guldi, E. Spiecker, V. R. Radmilović and C. J. Brabec, Assembling mesoscale-structured organic interfaces in perovskite photovoltaics, *Adv. Mater.*, 2019, **31**, 1806516. DOI: 10.1002/adma.201806516

Author contribution of Bianka M. D. Puscher

Photophysical measurements:

- fs-TAS measurements

Data analysis:

- Analysis of fs-TAS measurements
- Interpretation of fs-TAS measurements (in cooperation with Y. Hou, C. J. Brabec, and D. M. Guldi)
- Discussion of the results (in cooperation with Y. Hou, C. J. Brabec, and D. M. Guldi)

Writing of the manuscript:

- Writing of the fs-TAS part of the manuscript (in cooperation with Y. Hou)
- Revision of the manuscript (in cooperation with all authors)
- Proofreading of the manuscript (in cooperation with all authors)

4. J. Jiménez-López‡, B. M. D. Puscher‡, W. Cambarau, R. H. Fink, E. Palomares and D. M. Guldi, Hot electron injection into semiconducting polymers in polymer based-perovskite solar cells and their fate, *Nanoscale*, 2019, **11**, 23357-23365. ‡ contributed equally.
DOI: 10.1039/c9nr06297a

Author contribution of Bianka M. D. Puscher

Photophysical measurements:

- fs-TAS measurements using an excitation wavelength of 695 and 460 nm, and a laser fluence of 130 µJ cm^{-2} (in cooperation with J. Jiménez-López)
- Intensity-dependent fs-TAS measurements

Data analysis:

- Analysis of fs-TAS measurements (in cooperation with J. Jiménez-López)
- Interpretation of fs-TAS measurements (in cooperation with J. Jiménez-López and D. M. Guldi)
- Discussion of the results (in cooperation with all authors)

Writing of the manuscript:

- Writing of the manuscript (in cooperation with J. Jiménez-López, E. Palomares, and D. M. Guldi)
- Revision of the manuscript (in cooperation with all authors)
- Proofreading of the manuscript (in cooperation with all authors)